

**Measurement of jets produced in top quark events using the $e\mu$ final state with
2 b -tagged jets in pp collisions at $\sqrt{s} = 8$ TeV with the ATLAS detector**

by

Jacquelyn Kay Brosamer

A dissertation submitted in partial satisfaction of the

requirements for the degree of

Doctor of Philosophy

in

Physics

in the

Graduate Division

of the

University of California, Berkeley

Committee in charge:

Professor Marjorie Shapiro, Chair
Professor Leo Blitz
Professor Barbara Jacak

Fall 2015

The dissertation of Jacquelyn Kay Brosamer, titled Measurement of jets produced in top quark events using the $e\mu$ final state with 2 b -tagged jets in pp collisions at $\sqrt{s} = 8$ TeV with the ATLAS detector, is approved:

Chair _____

Date _____

University of California, Berkeley

**Measurement of jets produced in top quark events using the $e\mu$ final state with
2 b -tagged jets in pp collisions at $\sqrt{s} = 8$ TeV with the ATLAS detector**

Copyright 2015
by
Jacquelyn Kay Brosamer

Abstract

Measurement of jets produced in top quark events using the $e\mu$ final state with 2 b -tagged jets in pp collisions at $\sqrt{s} = 8$ TeV with the ATLAS detector

by

Jacquelyn Kay Brosamer

Doctor of Philosophy in Physics

University of California, Berkeley

Professor Marjorie Shapiro, Chair

The transverse momentum (p_T) and multiplicity of jets produced in top quark events are measured using 20.3 fb^{-1} of pp collision data at a center-of-mass energy of $\sqrt{s} = 8$ TeV. Jets are selected from top events requiring an opposite-charge $e\mu$ pair and two b -tagged jets in the final state. The data are corrected to obtain the particle-level fiducial cross section $\frac{1}{\sigma_{e\mu+2 \text{ } b\text{-jets}}} \frac{d\sigma_{\text{jet}}}{dp_T}$ for additional jets with rank 1-4, where rank=1 is the leading additional jet. These distributions are used to obtain the extra jet multiplicity as a function of minimum jet p_T threshold.

Contents

Contents	i
List of Figures	iv
List of Tables	x
1 Introduction	1
2 Theory	3
2.1 The Standard Model	3
2.1.1 Particles of the SM	3
2.1.2 Electroweak theory	4
2.1.3 Quantum chromodynamics	4
2.1.3.1 Factorization	5
2.1.4 Beyond the SM	7
2.2 Top quark physics	9
2.2.1 Top quark production at the LHC	10
2.2.2 Top quark decays	10
2.3 QCD in hadron-hadron collisions	11
3 Analysis strategy	16
4 The ATLAS detector and the LHC	18
4.1 The Large Hadron Collider	18
4.1.1 Accelerator Complex	19
4.2 Beam conditions	20
4.3 Overview of the ATLAS detector	21
4.3.1 Coordinate system	23
4.4 Inner detector	24
4.4.1 Pixel detector	25
4.4.2 SemiConductor Tracker	28
4.4.3 Transition Radiation Tracker	28
4.4.4 Track reconstruction	29

4.4.5	Vertex reconstruction	29
4.5	Calorimeters	30
4.5.1	Electromagnetic calorimeter	30
4.5.2	Hadronic calorimeter	31
4.5.3	Clustering	31
4.6	Muon System	32
4.7	The trigger system	34
4.7.1	Single electron trigger	34
4.7.2	Single muon trigger	36
5	Object reconstruction	37
5.1	Muons	37
5.2	Electrons	38
5.3	Jets	39
5.4	<i>b</i> -tagged Jets	40
6	Event selection	43
6.1	Data samples	43
6.1.1	Collision data	43
6.1.2	Simulated Samples	44
6.1.2.1	$t\bar{t}$ samples	44
6.1.2.2	Single top samples	45
6.1.2.3	Background samples	45
6.1.3	Pileup jet samples	45
6.2	Object definitions	47
6.2.1	Reconstructed objects	47
6.2.2	Truth objects	49
6.2.3	Truth matching	49
6.3	Event selection	50
6.3.1	Cleaning cuts	50
6.3.2	Event yields	51
6.3.3	Reconstructed distributions	51
7	Reconstruction of extra jets	55
7.1	Matching criteria	55
7.2	Background contributions to extra jets	55
7.2.1	Pileup jets	56
7.2.2	False jets	57
7.3	Reconstruction level distributions	59
8	Correction to particle-level	65
8.1	Introduction to unfolding	65

8.2	Procedure	65
8.2.1	Binning	66
8.2.2	Unfolding procedure	68
8.2.3	Bias in extra jet distributions due to event selection requirements . . .	69
8.3	Misidentified events	69
8.3.0.1	Reconstructed events that fail truth event selection	70
8.3.0.2	Truth events that fail reconstructed event selection	71
8.3.0.3	Event selection correction factors	75
8.4	Validation	76
8.4.1	Closure test	77
8.4.2	Stress test	77
9	Sources of uncertainty	81
9.1	Types of uncertainty	81
9.2	Detector modeling	81
9.2.1	Nuisance parameters	81
9.2.2	Computation of uncertainty	82
9.3	Single top rate	82
9.4	Pileup and false jet background	82
9.5	Input extra jet spectrum	84
9.6	Statistical uncertainty on migration matrix	84
9.7	PDF modeling uncertainty	85
9.8	Combined uncertainty	85
10	Results	91
10.1	Fully corrected distributions	91
10.2	χ^2 comparisons and discussion	96
11	Conclusions	98
A	Extra jets	99
B	Tracking studies	100
C	Modeling hadron decays	101

List of Figures

2.1	Summary of measurements of α_S as a function of the respective energy scale, Q , from Ref. [?]. The respective degree of QCD perturbation theory used in the extraction of α_S is indicated in brackets (NLO: next-to-leading order; NNLO: next-to-next-to leading order; res. NNLO: NNLO matched with resummed next-to-leading logs; N3LO: next-to-NNLO).	6
2.2	Diagram from Ref. [?] illustrating the structure of a generic hard scattering process of two incoming partons A and B with PDFs $f_{a/A}$ and $f_{b/B}$	8
2.3	Summary of the ATLAS direct m_{top} measurements. The results are compared with the ATLAS, Tevatron and Tevatron+LHC m_{top} combinations. For each measurement, the statistical uncertainty, the sum of the remaining uncertainties are reported separately. The JSF, bJSF contributions are statistical in nature and apply to analyses performing in-situ (top quark pair base) jet energy calibration procedures.	13
2.4	Feynman diagrams for $t\bar{t}$ production at leading order QCD	13
2.5	Summary of LHC and Tevatron measurements of the top-pair production cross-section as a function of the centre-of-mass energy compared to the NNLO QCD calculation complemented with NNLL resummation (top++2.0). The theory band represents uncertainties due to renormalisation and factorisation scale, parton density functions and the strong coupling. The measurements and the theory calculation is quoted at $m_{top}=172.5$ GeV. Measurements made at the same centre-of-mass energy are slightly offset for clarity.	14
2.6	Summary of ATLAS measurements of the single top production cross-sections in various channels as a function of the center of mass energy compared to a theoretical calculation based on NLO QCD complemented with NNLL resummation. For the s -channel only an upper limit is shown.	15
2.7	Feynman diagrams for single top quark production at leading order QCD. From left to right: t -channel production as flavor excitation; t -channel production as W -gluon fusion; s -channel production; Wt -channel production.	15
4.1	The location of the four main LHC experiments: ALICE, ATLAS, CMS and LHCb. The LHC tunnel is 27 km in circumference, situated underneath the border of France and Switzerland, near the city of Geneva, as shown. [?].	19

4.2	The LHC accelerator complex boosts particles to increasingly higher energies before reaching the LHC. The particle beams are accelerated successively by Linac 2, the Proton Synchrotron Booster (PSB), the Proton Synchrotron (PS), the Super Proton Synchrotron (SPS) and then finally enter the LHC rings [?].	20
4.3	Cumulative luminosity versus time delivered to (green), recorded by ATLAS (yellow), and certified to be good quality data (blue) during stable beams and for pp collisions at 8 TeV centre-of-mass energy in 2012. Luminosity can be lost due to data acquisition inefficiency or other effects.	22
4.4	Luminosity-weight distribution of the mean number of interactions per bunch crossing. Both the full data from the 2011 and 2012 pp runs at the LHC are shown.	23
4.5	Computer generated illustration of the whole ATLAS detector detector, with various subdetectors highlighted[?].	24
4.6	A computer-generated image representing how the ATLAS detector functions. The transverse paths of different types of particles are shown interacting with different elements of the detector[?].	25
4.7	Illustration of the ATLAS coordinate system[?].	26
4.8	Schematic view of the Inner Detector: an $r - z$ slice of the cylindrival barrel, disc endcaps with support tubes, and the solenoid magnet. Lines of constant η are drawn [?].	26
4.9	A diagram of the barrel of the Inner Detector: the three layers in the Pixels, the four layers in the SCT, and the many layers of the TRT [?].	27
4.10	Display of a 2012 event with 25 reconstructed vertices [?].	30
4.11	Cut-away view of the ATLAS calorimeter system [?].	31
4.12	Diagram of an electromagnetic calorimeter barrel module[?].	32
4.13	Diagram of a hadronic tile module[?].	32
4.14	Diagram of the muon system[?].	33
4.15	Schematic view of the calorimeter granularity available at the L1 trigger [?].	35
5.1	Reconstruction and identification efficiency [?].	38
5.2	Reconstruction and identification efficiency [?].	39
5.3	Combined efficiency of the 24 GeV and 60 GeV electron triggers. [?].	41
5.4	The relative Jet Energy Scale (JES) uncertainty for jets in the central region [?].	41
5.5	Light-jet rejection (left) and c -jet rejection (right) as a function of the b -tag efficiency for the b -tagging algorithms discussed based on simulated $t\bar{t}$ events. [?].	42
6.1	Distributions of the transverse momentum and η of the electron and muon in events with an opposite sign $e\mu$ pair and at least 2 b -jets in data and simulation. The distributions in data are compared to simulation normalized to data yields (see scale factors in Table 6.5). The ratio of different MC samples to data is shown with error bars corresponding to the MC statistical uncertainty and a shaded band corresponding to the data statistical uncertainty.	52

6.2 Distributions of the transverse momentum and η of the b -jets in events with an opposite sign $e\mu$ pair and at least 2 b -jets in the 2012 data. The distributions in data are compared to simulation, normalized to the same number of events as in the data (see scale factors in Table 6.5).. In events where more than two b -jets are reconstructed, the two highest p_T b -jets are selected and the remaining b -jet is classified as an extra jet (see Section ??). The ratio of different MC samples to data are shown with error bars corresponding to the MC statistical uncertainty and a shaded band corresponding to the data statistical uncertainty. Systematic uncertainties are not shown.	54
7.1 The η distribution of extra jets in simulation and data.	58
7.2 Mean number of reconstructed jets as a function of $<\mu>$ for jets in the p_T range $25 < p_T < 30$ GeV for (a) central and (b) forward jets in data events passing the $e\mu$ selection before and after correction for pileup. Jets passing the 70% MV1 b-tagging selection are removed. The pileup rate is estimated using the ZeroBiasOverlay data stream. The blue markers show the pileup subtracted rate before correcting for the $<\mu>$ -dependent efficiency of the JVF cut. The green points show the results after correction.	59
7.3 Distributions of minimum reconstructed ΔR between extra jets in simulation and data for (Na) the first, (b) second, (c) third and (d) fourth extra jet.	60
7.4 Distributions of ΔR between reconstructed extra jets and the nearest truth jet for (a) the first, (b) second, (c) third and (d) fourth extra jet.	61
7.5 Dependence of the unmatched extra jet rate on μ for the baseline simulation.	62
7.6 Distributions of the reconstructed extra jet multiplicity as a function of p_T threshold in simulation and data. The distributions in data are compared to $t\bar{t}$ simulation normalized to the same number of events as in the data. Extra jets from pileup are excluded in simulation by requiring a match to truth. Extra pileup jets are subtracted from the data. The ratio of different MC samples to data is shown with error bars corresponding to the MC statistical uncertainty and a shaded band corresponding to the data statistical uncertainty. Systematic uncertainties are not shown.	63
7.7 Distributions of reconstructed extra jet p_T in simulation and data. The distributions in data are compared to $t\bar{t}$ simulation normalized to the same number of events as in the data. Backgrounds from single top and extra pileup jets are included as background to $t\bar{t}$. The ratio of different MC samples to data is shown with error bars corresponding to the MC statistical uncertainty and a shaded band corresponding to the data statistical uncertainty. Systematic uncertainties are not shown.	64
8.1 Fraction of reconstructed extra jets with truth matches inside the fiducial region (a) and ratio of alternate generators to the baseline (b). This factor is used to correct the data for p_T smearing across the fiducial boundary.	69

8.2	Migration matrix between the truth and reconstructed number of extra jets in each bin (a) and distribution of ‘missed’ truth jets not matched to reco jets (b). Jets are binned according to both p_T value and rank. The matrix is filled from events passing both reconstructed and truth $e\mu+2$ - b jet events in the baseline $t\bar{t}$ simulation. ‘Missed’ jets are handled by the RooUnfold framework.	70
8.3	Distributions of the (a) $e p_T$, (b) b -jet p_T , (c) b -jet MV1 weight and (d) extra jet multiplicity. Each distribution is normalized by the number of events falling in that category. Events were simulated with PowHeg+Pythia $hdamp=\infty$ $t\bar{t}$	72
8.4	Distributions of the truth (a) b -jet p_T , (b) extra jet multiplicity, (c) leading extra jet p_T and (d) subleading extra jet p_T . Each distribution is normalized by the number of events falling in that category. Events were simulated with PowHeg+Pythia $hdamp=\infty$ $t\bar{t}$ and required to pass the fiducial truth $e\mu+2$ b -jet selection.	73
8.5	Distributions of the truth (a) extra jet multiplicity, (b) leading extra jet p_T , (c) subleading extra jet p_T and (d) subsubleading extra jet p_T in bins of the average of the p_T of the two truth b -jets used to select the event. Each distribution is normalized by the number of events falling in that bin. Events were simulated with PowHeg+Pythia $hdamp=\infty$ $t\bar{t}$ and required to pass the fiducial truth $e\mu+2$ b -jet selection.	74
8.6	(a) Ratio of unfolded extra jets to truth extra jets different $t\bar{t}$ generators (including a 2.9% contribution from single top). (b) Fractional difference of the correction factor from baseline for different generators. Extra jets in events passing reconstructed and truth selection for each generator are added to single top and used to fill a response matrix. Then each generator is unfolded against itself, using all selected reconstructed events. Extra jet truth distributions are made without any reconstruction requirements. Finally, the unfolded distribution is divided by the truth distribution to obtain a correction factor for each bin. . .	76
8.7	(a) Pull distribution and (b) fractional bias for the extra jets from the baseline $t\bar{t}$ simulation unfolded against a matrix filled with the baseline $t\bar{t}$ simulation with all correction factors. The Bayesian unfolding method with 2 iterations is used. One thousand pseudoexperiments, each the size of the events in data, are randomly selected from the sample and unfolded. Each bin of the pull distribution over the pseudoexperiments is fit with a gaussian. The black points show the fitted mean of each bin. A fitted mean of zero shows the unfolding is not significantly biased. The blue band shows the fitted σ of each bin. A fitted σ of one shows the unfolding correctly estimates the errors.	79

8.8	Fractional bias distributions for pseudoexperiments from alternative generators unfolded against a matrix filled with the baseline simulation. The truth spectrum of the baseline sample is reweighted to match jet p_T and multiplicity spectra of (a) PowHeg+Herwig(b) MadGraph+Pythia, (c) PowHeg+Pythia hdamp= m_t , and (d) MC@NLO+Herwig simulation. One thousand pseudoexperiments, each the size of the events in data, are constructed for each generator and unfolded. The Bayesian unfolding method with 2 iterations is used. Each bin of the distribution over the pseudoexperiments is fit with a gaussian. The black points show the fitted mean of each bin and the blue band shows the fitted sigma.	80
9.1	Ratio of reconstructed extra jets spectrum obtained from systematic variations of the 15 JES eigenstate nuisance parameters with respect to that obtained using the nominal parameters. The band shows the uncertainty obtained from the samples with gaussian variation of all nuisance parameters. The upper and lower lines shows uncertainty from the quadratic sum of the independent variations of each nuisance parameter by $\pm 1\sigma$. The distribution of samples values has fitted $\mu = 1$ and σ consistent with the $\pm 1\sigma$ method.	83
9.2	(a) bias and (b) fractional bias distributions PDF variations of MC@NLO+Herwigunfolded with the nominal MC@NLO+Herwigmigration matrix. Each bin of the distribution over the pseudoexperiments is fit with a gaussian. The outer product of the bias is used to compute the uncertainty due to the PDF.	85
9.3	Fractional bias distributions for pseudoexperiments from MadGraph+Pythia radiation samples unfolded against a matrix filled with nominal MadGraph+Pythia. The truth spectrum of the baseline sample is reweighted to match jet p_T and multiplicity spectra of (a) MadGraph+Pythia RadLo (b) MadGraph+Pythia RadHi simulation. One thousand pseudoexperiments, each the size of the events in data, are constructed for each generator and unfolded. The Bayesian unfolding method with 2 iterations is used. Each bin of the distribution over the pseudoexperiments is fit with a gaussian. The black points show the fitted mean of each bin and the blue band shows the fitted sigma.	86
9.4	Unmatched jets in the baseline $t\bar{t}$ simulation and the hybrid sample. The difference between the two is used to estimate the uncertainty.	87
9.5	Sum of systematic uncertainties due to detector modeling. The ratio of the simulated extra jets reconstructed with each systematic variation is taken with respect to the nominal. The band shows the data statistical uncertainty for reference. .	89
9.6	(a) The covariance matrix associated with the statistical uncertainty of the input spectrum returned from RooUnfold. (b) The covariance matrix from all sources of uncertainty, obtained by adding the covariance matrices from all sources of systematic uncertainty to (a). This matrix is used to determine the χ^2 agreement between generators and the fully corrected data.	90

10.1 Distributions of the unfolded p_T of extra jets in data and simulation. Each sample is unfolded against a response matrix filled with baseline $t\bar{t}$ +single top simulation.	92
The gray band on the ratio shows the sum of statistical and systematic uncertainties.	
10.2 Distributions of the number of unfolded extra jets with p_T < (a) 25, (b) 30, (c) 40 and (d) 50 GeV in data and simulation. Each sample is unfolded against a response matrix filled with baseline $t\bar{t}$ +single top simulation. The gray band on the ratio shows the sum of statistical and systematic uncertainties.	93
10.3 Distributions of the unfolded p_T of extra jets in data and simulation. Each sample is unfolded against a response matrix filled with baseline $t\bar{t}$ +single top simulation.	
The gray band on the ratio shows the sum of statistical and systematic uncertainties.	94
10.4 Distributions of the unfolded p_T of extra jets in data and simulation. Each sample is unfolded against a response matrix filled with baseline $t\bar{t}$ +single top simulation.	
The gray band on the ratio shows the sum of statistical and systematic uncertainties.	95
10.5 Visual representation of the χ^2 distributions for (a) PowHeg+Pythia hdamp= ∞ (b) PowHeg+Pythia8 (c) MadGraph+Pythia and (d) PowHeg+Pythia hdamp= m_t . Each element ij of the matrix is given by $M_{ij} = (N_{mc}^i - N_{data}^i)\sigma_{ij}^{-1}(N_{mc}^j - N_{data}^j)^j$ where N_{mc}^i is the number of jets predicted in bin i, N_{data}^i is the number of jets in bin i in data, and σ^{-1} is the inverse of the covariance matrix.	97

List of Tables

2.1	Spin and charge of particles in the SM.	12
2.2	Mass of particles in the SM, taken from Ref. [?].	12
6.1	$t\bar{t}$ samples used in this analysis. The sample name, dataset ID, simulation type, final state simulated (non-fully hadronic, nFH, or dilepton, $\ell\ell$) and tune is given. The Alpgen samples consist of several samples with different parton multiplicities and sometimes dedicated heavy flavor samples.	46
6.2	$Z+jets$ and diboson background samples used in this analysis. The sample name, process, simulation type, process simulated, final state simulated (non-fully hadronic, nFH, or dilepton, $\ell\ell$) and tune is given. The Alpgen samples consist of several samples with different parton multiplicities and sometimes dedicated heavy flavor samples. Dataset IDs are listed in Appendix ???.	46
6.3	Single top Wt -channel samples used in this analysis. The sample name, dataset ID, simulation type, and tune is given. All samples are simulated with the inclusive final state in the Wt channel.	46
6.4	Number of events with opposite sign $e\mu$ and at least 2 b -jets in the data compared to that from Monte Carlo, broken down into contributions from $t\bar{t}$, Wt single top, $Z+jets$ and dibosons. Only central values are shown here; systematic uncertainties are discussed in Section ???.	53
6.5	Number of events with an opposite sign $e\mu$ and at least 2 b -jets for different $t\bar{t}$ generators. The last column gives scale factor to normalize the sum of the $t\bar{t}$ simulation and single top yields ($N_{\text{single top}} = 361.4$) to the data yield (12332).	53
8.1	Binning for unfolding of extra jets. Jets are binned simultaneously in both rank (p_T order) and p_T . For each jet rank, variable sized p_T bins are chosen so that at least 10 data events fall in each bin. The first bin in p_T for each rank is treated as underflow bins. These bins are not reported as part of the measurement.	66
8.2	Number of events passing different combinations of truth and reconstructed selection requirements.	71
8.3	Number of selected reconstructed events that fail truth selection categorized by reason they have failed. The selections are applied sequentially in the order listed in the table.	75

8.4 Number of truth events that fail reconstruction selection categorized by reason they have failed. The selections are applied sequentially in the order listed in the table.	75
10.1 χ^2 between extra jet p_T spectra in fully corrected data and different generators. The first column represents the agreement including only (diagonal) statistical uncertainties. The second column also includes the covariance due to systematic uncertainties (primarily JES).	96

Acknowledgments

To do

Chapter 1

Introduction

The Standard Model (SM) theory of particle physics has been very successful at describing the interactions of fundamental particles. With the discovery of the Higgs boson, the SM is complete and may be the correct theory up to the energy scale of gravity. The Large Hadron Collider (LHC) was built in order to probe this the SM and look for solutions to some of the unknown issues in particle physics that may involve physics beyond the stand model.

Despite the success of the SM, one of the most uncertain of its sectors is Quantum Chromodynamics (QCD). Due to the non-pertubative nature of QCD as well as its higher energy scale, QCD has not been as precisely measured as other parts of the SM. In particular, since the top quark was only discovered in the late 1990s, its decays and properties have not been as studied as thoroughly.

The top quark plays a special role in the Standard Model and in searches for physics beyond the Standard Model . Its high mass means its coupling to the Higgs Boson is large. This high mass, together with the presence of charged leptons, missing energy and b -jets as top decay products, make the top a primary source of background in many searches for new physics. For these reasons, accurate modeling of the properties of top quark events is an important part of the LHC program.

Measurements of the activity of additional jets (jets not coming from the decay of top quarks) have been made by ATLAS [?, ?, ?] and CMS[?] using pp data with $\sqrt{s} = 7$ TeV. Comparison of the measured distributions with the predictions of Monte Carlo (MC) generators indicate that some state-of-the-art generators (e.g. MC@NLO) have a difficult time in reproducing the data, while for others agreement with data can be improved with appropriate choice of generator parameters. For example, in Powheg+Pythia adding a damping function that limits the resummation of higher-order effects incorportated into the Sudakov form factor improves the agreement between data and MC [?] at 7 TeV.

The range of predictions observed in standard MC generators for 8 TeV pp interactions is shown in Figure ???. The fiducial definition of extra jets is provided in Section ???. Differences in rate as large as 40% are seen for jet multiplicities ≥ 5 . Differences up to 20% for the leading jet and up to 40% for the subleading jet are seen at high jet transverse momentum.

This note presents a study of jet activity in top quark events using the $e\mu$ final state

with 2 b -tagged jets in pp collisions at $\sqrt{s} = 8$ TeV. The analysis employs an event selection which closely matches that used in the ATLAS 8 TeV cross section measurement[?]. The particle-level fiducial cross section $\frac{1}{\sigma_{e\mu+2 \text{ } b\text{-jets}}} \frac{d\sigma_{\text{jet},i}}{dp_T}$ for additional jets with rank 1-4, where rank=1 is the leading additional jet are measured and these distributions are used to obtain the extra jet multiplicity as a function of minimum jet p_T threshold. The p_T distribution of b -jets is also presented.

At lowest order, the $e\mu + 2$ b -jet final state results from $t\bar{t}$ production where both the t and the \bar{t} decay leptonically. Events where the leptons do not arise from W decay are suppressed by isolation and transverse momentum cuts on the leptons; they are treated as background and corrected for in the analysis. The distinction between $t\bar{t}$ and Wt final states cannot be made at NLO in QCD unless the top quark is stable. Once it decays to Wb , the same initial and final state appear in both processes, e.g. $gg \rightarrow W^+W^-b\bar{b}$ appears at LO and NLO via $gg \rightarrow t\bar{t} \rightarrow W^+W^-b\bar{b}$ or at NLO via $gg \rightarrow Wt\bar{b} \rightarrow W^+W^-b\bar{b}$. Quantum interference must occur and the classification into " $t\bar{t}$ " and " Wt " is not possible. If restrictions are placed on the final state, this interference can be restricted and an approximate distinction made. For example, if a kinematic constraint is applied so both $W^-\bar{b}$ and W^+b have invariant mass equal to the top mass, the process is dominated by " $t\bar{t}$ ", if $W^-\bar{b}$ has an invariant mass far from the top quark mass " Wt " will dominate. No such kinematic constraint is applied in this analysis, so that any discussion of " $t\bar{t}$ " and " Wt " contributions can only be made in simulation where samples labelled by " $t\bar{t}$ " and " Wt " are used. In standard ATLAS MC samples, $\sim 3\%$ of the $e\mu + 2$ b -jet are assigned to the " Wt " process. This analysis chooses to treat this component as signal rather than background as it cannot separate them in a model independent manner. However, if a MC is used to fix the " Wt " component, then it can be subtracted from the data and comparisons with " $t\bar{t}$ " MC made. The subtraction will introduce (small) additional systematic uncertainties. The effect of such a subtraction is discussed below.

This thesis is structured as follows: FINAL CHAPTER STRUCTURE TO FOLLOW

Chapter 2

Theory

This chapter reviews some of the theoretical concepts relevant to the subsequent physics analysis. The importance of the top quark within the Standard Model is first discussed. The modeling of physics at hadron colliders is also reviewed.

2.1 The Standard Model

The SM of particle physics is one of the most precisely tested and successful theories in the history of physics [?]. The theory represents the best current understanding of the fundamental behavior of subatomic particles and provides the framework for particle physics predictions. All predictions of the SM have been verified and found to be self-consistent up to the Planck scale (10^{15-19} GeV).

The SM uses the mathematical framework of Quantum Field Theory (QFT) to describe two kinds of particles, fermions and bosons. Fundamental interactions between these particles can be derived from the conservation of a symmetry called gauge invariance. This general principle maps all conserved quantities to the invariance of the Lagrangian under some transformation, an aesthetically appealing idea known as Noether's theorem. The SM provides a unified description of the strong, weak and electromagnetic forces, but does not (yet) include gravity. The symmetry group of the SM is $SU(3) \times SU(2) \times U(1)$.

2.1.1 Particles of the SM

Tables ??-?? summarize the properties of the fundamental particles of the SM described below.

Fermions are spin- $\frac{1}{2}$ point-like particles that form ordinary matter. The two types of fermions are known as leptons and quarks. The three lepton generations, each with a charged lepton and a neutrino, interact via the electroweak force. The three quark generations, each with an up-type and down-type quark, interact via both the electroweak force and the strong force. The strong force combines quarks into composite particles. Three such quarks form a

baryon, while two quarks form a meson. Each fermionic generation is identical to the first, except for mass.

Bosons are particles with integer spin that mediate interactions between particles. Each gauge boson corresponds to a different fundamental force, and the range each force is inversely related to the boson mass.

Electromagnetic (EM) force mediated by the massless and chargeless photon (γ). Since the photon is massless, the range of the EM force is infinite. The EM force is responsible for many common interactions, such as radiation of photons from excited atoms.

Weak force mediated by the W^\pm and Z^0 bosons and is responsible for nuclear reactions such as beta decay .

Strong force mediated by gluons (g) is responsible for the formation of protons and neutrons. The quarks are the only fermions that interact strongly.

Discovered in 2012, the Higgs boson is the final particle in the SM. In order to explain the mass difference between the photon and electroweak bosons, the symmetry between the EM and weak forces must be broken. The Higgs field interacts with the electroweak gauge bosons to provide masses while preserving the local gauge invariance of the SM.

2.1.2 Electroweak theory

At low energy, the EM and weak forces appear distinct. Above the unification energy ($\sim 100\text{GeV}$), the EM and weak forces are unified into a single interaction known as the electroweak interaction. The corresponding symmetry group is $SU(2) \times U(1)$, where $SU(2)$ represents the weak force and $U(1)$ represents the EM force. MORE FROM PDG

2.1.3 Quantum chromodynamics

Quantum chromodynamics (QCD) is a gauge theory which interactions between quarks via the strong force. The six flavors of quarks (u, d, s, c, b and t) each carry a conserved quantum number called color, which is analogous to electric charge in QED. Neither quarks nor gluons can exist as free particles. Instead, color-neutral combinations of quarks, anti-quarks and gluons called hadrons are observed.

The QCD Lagrangian for the interaction between two quarks i and j can be written as [?]:

$$\mathcal{L}_{QCD} = \bar{\psi}_i (i\gamma^\mu \partial_\mu \delta_{ij} - g_s \gamma^\mu t_{ij}^C \mathcal{A}_\mu^C - m \delta_{ij}) \psi_j - \frac{1}{4} G_{\mu\nu}^A G_A^{\mu\nu}, \quad (2.1)$$

$$\text{where } G_{\mu\nu}^A \equiv \partial_\mu \mathcal{A}_\nu^A - \partial_\nu \mathcal{A}_\mu^A - g_s f_{ABC} \mathcal{A}_\mu^B \mathcal{A}_\nu^C, \quad (2.2)$$

where repeated indices are summed over, γ^μ are the Dirac γ matrices. ψ_i is the quark-field spinor, where the color index i can correspond to one of three (N_C) quark flavors. \mathcal{A}_μ^B

represents the gluon fields, where C runs from 1 to $N_C^2 - 1 = 8$, corresponding to eight types of gluons. t^A are the eight 3×3 generating matrices of $SU(3)$ and f_{ABC} the group structure constants of $SU(3)$. The fundamental parameters are the coupling g_s and the quark masses m .

The structure of the Lagrangian predicts three types of vertices: a quark-antiquark-gluon ($q\bar{q}g$) vertex proportional to g_s , a three gluon vertex proportional to g_s , and a four gluon vertex proportional to g_s^2 . Since gluons carry color charge, they can directly couple to other gluons, unlike other bosons. These self-interaction vertices mean that QCD has divergent terms that are not found in other SM sectors.

Perturbative QCD calculations at next-to-leading order and beyond necessarily involve these divergent quark and gluon loops. These divergences must be removed in order to obtain a physical result. In order to remove the divergences, the strong coupling constant must be “renormalized” and expressed as a function of an (unphysical) renormalization scale μ_R . Notably, QCD predictions change depending on the scale of the probe. This is sometimes referred to as the “running” of the coupling constant. Predictions for a given process are evaluated with μ_R as close to the momentum transfer Q as possible, so that $\alpha_s(\mu_R \simeq Q)$ gives the effective strength of the strong force in that particular process.

The strong coupling constant $\alpha_S \equiv g_s^2/4\pi$ is related the renormalization scale μ_R by the renormalization group equation (RGE):

$$\mu_R^2 \frac{\alpha_S}{\mu_R^2} = \beta(\alpha_S) = - (b_0 \alpha_S^2 + b_1 \alpha_S^3 + b_2 \alpha_S^4 + \dots) \quad (2.3)$$

where the coefficients b are called the beta-function coefficients and depend on the number of quark colors. The values of the beta coefficients up to b_3 can be found in Ref. [?].

Figure 2.1 shows the next-to-leading-order QCD prediction for α_S as a function of Q , as well as several experimentally measured values of α_S for discrete energy scales. Experimental measurement agrees very well with the theoretical predictions. The negative sign on the right side of Eqn.2.3 means that the strong coupling becomes weaker as the scale increases: $\alpha_S \sim 0.1$ for momentum transfers $100 \text{ GeV} \lesssim Q \lesssim 1 \text{ TeV}$. This is the origin of the previously mentioned asymptotic freedom, which allows partons to be considered approximately free at high energy. The divergence of the coupling constant at low energy results in the formation of stable hadrons and is called “confinement.”

2.1.3.1 Factorization

Because of the scale dependence of QCD, interactions can be separated into two regimes, with the transition around the QCD confinement scale, $\Lambda_{QCD} \sim 200 \text{ MeV}$, the energy at which QCD becomes non-perturbative. At low energy, α_S is of order unity, so perturbative expansion is not possible. The quarks are bound together by soft gluon emissions into a proton. At scales far above the QCD confinement scale, the partons can be considered free objects and can be treated with perturbative expansion.

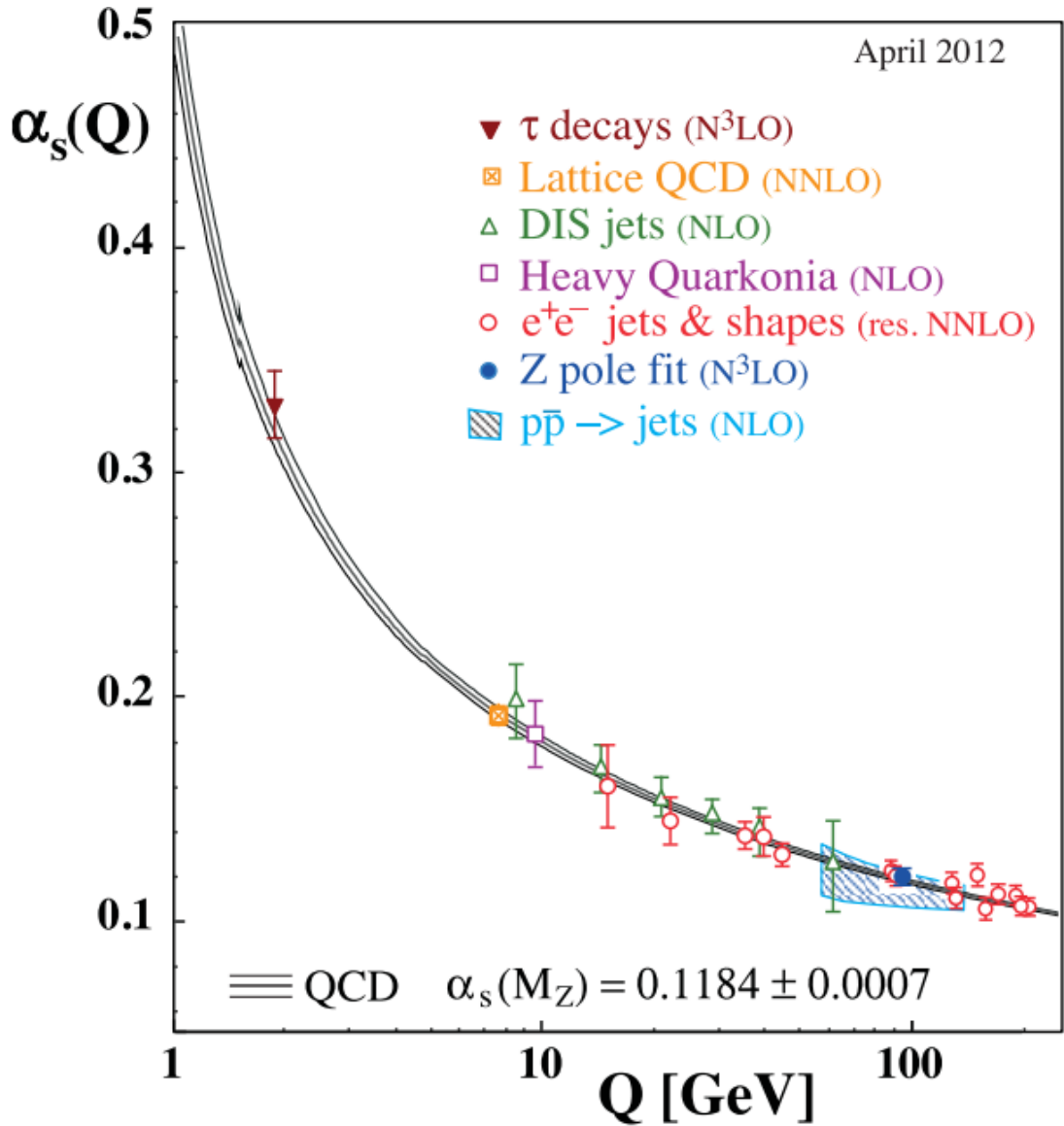


Figure 2.1: Summary of measurements of α_S as a function of the respective energy scale, Q , from Ref. [?]. The respective degree of QCD perturbation theory used in the extraction of α_S is indicated in brackets (NLO: next-to-leading order; NNLO: next-to-next-to leading order; res. NNLO: NNLO matched with resummed next-to-leading logs; N3LO: next-to-NNLO).

The hard scatter interaction with momentum transfer Q occurs on a time scale that goes as $\tau \sim 1/Q$ which is much larger than the time scale of interactions between protons $\tau \sim 1/\Lambda_{QCD}$. This fact allows high energy proton collisions to be *factorized* into two independent processes: the Parton Distribution Function (PDF), which a phenomenological description of the momentum distribution among the partons inside the proton which depends only on

the momentum scale, and the partonic cross section $\hat{\sigma}$, which uses perturbative QCD to determine the calculates the scatter of the hard probe from one of the free partons inside the proton.

Specifically, the hadronic cross-section for a particular process can be written the weighting of the subprocess cross section with the PDFs $f_{q/A}(x)$ extracted from deep inelastic scattering experiments[?]:

$$\begin{aligned}\sigma(AB \rightarrow X) &= \int dx_a dx_b f_{a/A}(x_a, \mu_F^2) f_{b/B}(x_b, \mu_F^2) \hat{\sigma}_{ab \rightarrow X} \\ &= \int dx_a dx_b f_{a/A}(x_a, \mu_F^2) f_{b/B}(x_b, \mu_F^2) \times [\sigma_0 + \alpha_S(\mu_R^2) \sigma_1 + \dots]\end{aligned}\quad (2.4)$$

which is diagrammatically represented in Figure 2.2. The partonic cross-section can be perturbatively expanded in powers of the strong coupling constant α_S for some renormalization scale μ_R . The PDF $f_{a/A}(x_a, \mu_F^2)$ gives the probability that a proton with momentum p_A contains a parton a with momentum p_a . This function depends only on the fraction of the proton momentum distributed to parton a , $x_a \equiv p_a/p_A$, and the factorization scale μ_F .

Since the PDF part of the cross section is in the non-perturbative regime of QCD, PDFs must be determined by global fits to experimental measurements of deep inelastic and other hard-scattering processes. PDFs derived from measurements of one process can be used for predictions in a different process. For example, positron-proton scattering data from the HERA experiment can be used to make predictions for proton-proton collision at the LHC.

PDF measurements depend on the scale of the hard probe, so theoretical calculations are needed to evolve the PDFs between experimental data points. The differential equations governing the μ^2 dependence of the PDFs are called the DGLAP equations and are derived in Ref. [?]. Much like the RGE introduces an arbitrary μ_R , the DGLAP equations introduce a factorization scale μ_F to absorb the divergences from soft parton emissions. To avoid unnaturally large logarithms in the pertubative expansion, μ_F and μ_R are usually assumed to be equal and of the order of the typical momentum scales of the hard scattering process. The theoretical uncertainty from the arbitrary choice of μ_F and μ_R is usually evaluated by repeating the calculation with the scale doubled and halved.

2.1.4 Beyond the SM

In addition to providing a test of the SM, the top quark may also provide a window to physics at higher energy scales beyond the SM.

The top quark is important in aesthetic problem with the Higgs mass known as the hierarchy problem or fine tuning. The Higgs mechanism provides an explanation for electroweak symmetry breaking and acquisition of mass by other SM particles. As a scalar particle, the Higgs receives higher-order corrections to its physical (measured) mass from interactions with fermions, gauge bosons and itself. These corrections are on the order of the Planck scale, $\mathcal{O}(\Lambda^2 \approx 10^{30-38} \text{ GeV})$, while the observed mass is class to the electroweak scale, $\mathcal{O}(100 \text{ MeV})$. Thus, in order to obtain the observed mass without introducing new

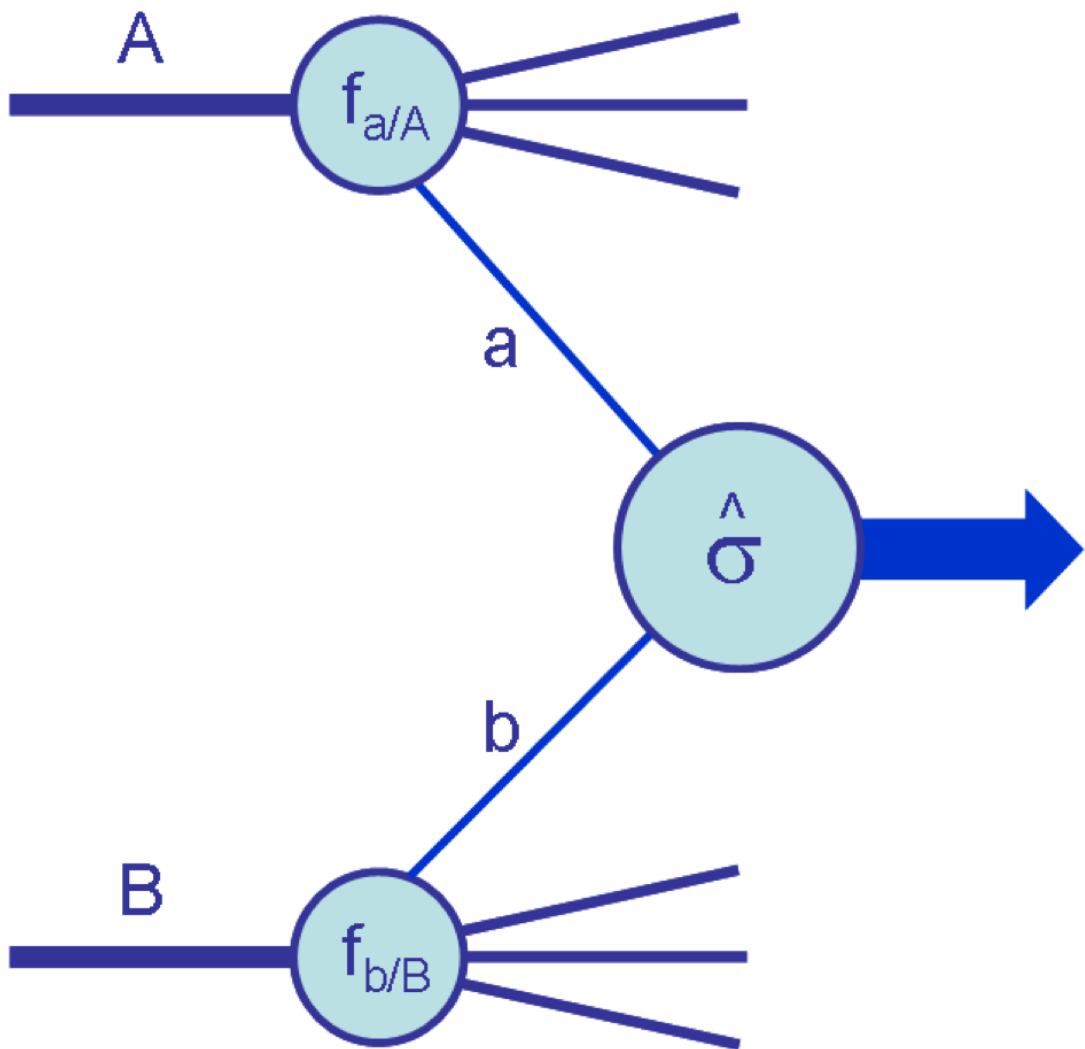


Figure 2.2: Diagram from Ref. [?] illustrating the structure of a generic hard scattering process of two incoming partons A and B with PDFs $f_{a/A}$ and $f_{b/B}$.

physics, there must be an unnatural canceling. Since the dominant higher-order correction to the Higgs mass comes from the top, precisely measuring the top's mass and other properties may provide insight to this problem.

In addition to the hierarchy problem, there are several other open questions which cannot be explained by the SM. The SM does not account for the 85% of our universe made up of

dark matter particles, or provide an explanation for the observed asymmetry between matter and anti-matter. The SM also does not account for the observed non-zero mass of neutrinos or have a way to incorporate gravitational interactions.

Theorists have formulated many extensions to the SM that address these puzzles. Perhaps the most widespread, Supersymmetry (SUSY) [?] proposes an additional superpartner for every particle in the SM. SUSY is especially popular because it naturally contains a light, stable, neutral dark matter candidate and solves the hierarchy problem. Diagrams from superpartners remove the need to fine tune the Higgs mass. Since SUSY has not been observed, the superpartners of SM particles must have different masses, and SUSY has to be a broken symmetry. However, in order to satisfactorily solve the hierarchy problem, the superpartners with the largest contributions to the Higgs mass must be $\mathcal{O}(\text{ TeV})$. This means that they should be discoverable at the LHC.

Another popular SM extension, called the Randall-Sundrum model [?], posits an extra dimension in which gravity would propagate. This model includes a new particle, a Kaluza-Klein gluon, that propagates into the extra dimension and decays into a top quark pair.

Many of the signals for new physics are dominated by the top quark since heavier particles are more sensitive to higher energy scales. The top pair production analyzed in this thesis is important as a background for $t\bar{t}$ resonances [?] and other searches [?].

2.2 Top quark physics

The top quark was first discovered at Fermilab in 1995 [?][?]. As the heaviest known fundamental particle, the top quark is an important probe of the Standard Model (SM) and extensions of the SM. Before the Large Hadron Collider (LHC), the Tevatron provided the only experimental observation of the top. The LHC produces a top quark every few seconds, about a hundred times more frequently than the Tevatron. This significant increase in statistics allows precision measurements of the top at the LHC, which is sometimes called a “Top Factory.”

Because of its large mass, the top quark plays a special role in the SM. The top mass is about the same as a gold atom nucleus, 40 times larger than the next heaviest quark and 10^5 times heavier than the lightest quark. The mass of the top quark has been precisely measured in different decay channels at both the LHC and the Tevatron. Figure 2.3 shows a recent summary of these measurements, which can be combined to give a world average of 173.34 ± 0.76 for the top quark mass.

The top has a very short lifetime ($\sim 5 \times 10^{-25}$ s), so it is the only quark that decays before it can form a hadron with other quarks. This unique property means that the top is the only “bare” quark that can be accessed at the LHC. The top is also the only quark with Yukawa coupling to the Higgs boson of order unity. Thus, accurately measuring its properties (mass, coupling, cross section, branching ratios) provides an important information about Quantum Chromodynamics (QCD), the SM description of interactions between quarks via the strong force.

2.2.1 Top quark production at the LHC

In pp collision at the LHC, top quarks are mostly produced in pairs through the leading order QCD processes $gg \rightarrow t\bar{t}$ and $q\bar{q} \rightarrow t\bar{t}$. The Feynman diagrams for these processes are shown in Figure 2.4. At Tevatron with $p\bar{p}$ collisions, $t\bar{t}$ production was dominated by quark annihilation ($\sim 85\%$). At the LHC, the higher collision energy and lack of valence anti-quarks in the proton result in gluon-fusion dominated $t\bar{t}$ production ($\sim 85\%$) [?]. The total $t\bar{t}$ cross-section has been computed at next-to-next-to leading order (NNLO) with next-to-next-to-leading-log soft gluon resummation (NNLL) in Ref. [?] with a final theoretical uncertainty of $\sim 3\%$ and found to agree with experimental measurements. Figure 2.5 compares this calculation with measurements made at both in the LHC and Tevatron in various decay channels.

Top quarks can also be produced singly via electroweak processes. Because the weak coupling is much smaller than the strong coupling, fewer quarks are produced singly than in pairs. The Feynman diagrams for single top production are shown in Figure 2.7. Single production can mediated by virtual s -channel and t -channel W -bosons. These production channels provide sensitivity to physics beyond the SM. Single tops are also produced in association with a W -boson (Wt -associated production). While negligible at the Tevatron, at the LHC, Wt -associated production provide a sizeable contribution to single top production. The inclusive cross-section for s -channel, t -channel and Wt -associated single top production has been computed to NNLO. This calculation is compared with the ATLAS experimental measurements of each channel in Figure 2.6.

2.2.2 Top quark decays

At lowest order in the SM, the top quark can only decay to a W boson and a down-type quark: $t \rightarrow qW$ where $q = b, s, d$. The rate of each of these decays is proportional to the square of the Cabibbo-Kobayashi-Masakawa (CKM) matrix, $|V_{tq}|^2$. Measured from experiment, the CKM matrix governs quark mixing in flavor-changing weak decays [?].

Weak hadron decays and the unitarity of the CKM matrix constrain the value of $0.9990 < |V_{tb}| < 0.9992$ at the 95% C.L [?]. Top quarks nearly always decay with $t \rightarrow Wb$.

Experimentally, the decay modes of $t\bar{t}$ are distinguished by the decay of the two W -bosons:

All hadronic Both W bosons decay to quark pairs: $t\bar{t} \rightarrow WbWb \rightarrow bbqqqq$. Because there are 6 quarks in the final state, this channel has a large multi-jet background, which can be difficult to subtract.

Semi-leptonic One W boson decays to a quark pair and the other decays to a lepton and neutrino: $t\bar{t} \rightarrow WbWb \rightarrow bbqql\nu$. This channel can be further categorized by lepton flavor.

Dileptonic Both W bosons decay to leptons: $t\bar{t} \rightarrow WbWb \rightarrow bbl\nu l\nu$. Though the dilepton channel has the fewest events, it often provides least background.

2.3 QCD in hadron-hadron collisions

The protons collided at the LHC are composite objects made of point-like quarks held together by soft gluon emissions. Because of the asymptotic freedom of QCD, α_s is of order unity at the scale of these emissions within the proton, but as the scale of emissions increase α_s quickly drops. Then, at scales far above the QCD confinement scale ($\Lambda_{QCD} \sim 200$ MeV, the energy at which QCD becomes non-perturbative), the protons can be considered free objects. The hard scatter interaction with momentum transfer Q occurs on a time scale that goes as $\tau \sim 1/Q$ which is much larger than the time scale of interactions between protons $\tau \sim 1/\Lambda_{QCD}$. This fact allows high energy proton collisions to be *factorized* into two independent processes: the Parton Distribution Function (PDF), which describes the momentum distribution among the partons inside the proton and depends only on the momentum scale, and the partonic cross section $\hat{\sigma}$, which uses perturbative QCD to determine the calculation of the scatter of the hard probe from one of the free partons inside the proton.

PDF STUFF

Then, the final $t\bar{t}$ cross section ($\sigma_{t\bar{t}}$) is a convolution of the partonic cross section ($q\bar{q}, qq \rightarrow t\bar{t}$) and the parton distribution functions (PDFs) [?]:

$$\sigma_{t\bar{t}}(s, m_t) = \sum_{i,j} \int_0^1 dx_i \int_0^1 dx_j f_i(x_i, \mu_F^2) f_j(x_j, \mu_F^2) \times \hat{\sigma}_{ij}(\hat{s}, m_t, \alpha_s(\mu_R), \mu_R,) \quad (2.5)$$

DISCUSSION OF GLUON GLUON ETC AT LHC

At the LHC, qg scattering occurs with the highest parton luminosity but the partonic cross-section $\hat{\sigma}_{qg}$ is smaller than either $\hat{\sigma}_{gg}$ or $\hat{\sigma}_{qq}$. The largest contribution for top pair production at the LHC comes from gluon-gluon fusion, due to the combination of a large partonic cross-section and the second largest parton luminosity. The second largest contribution comes from quark-antiquark annihilation. At NLO QCD, the total $t\bar{t}$ production at the LHC comprises approximately 90%

At the Tevatron, a previous $p\bar{p}$ collider with lower energy, $t\bar{t}$ production was

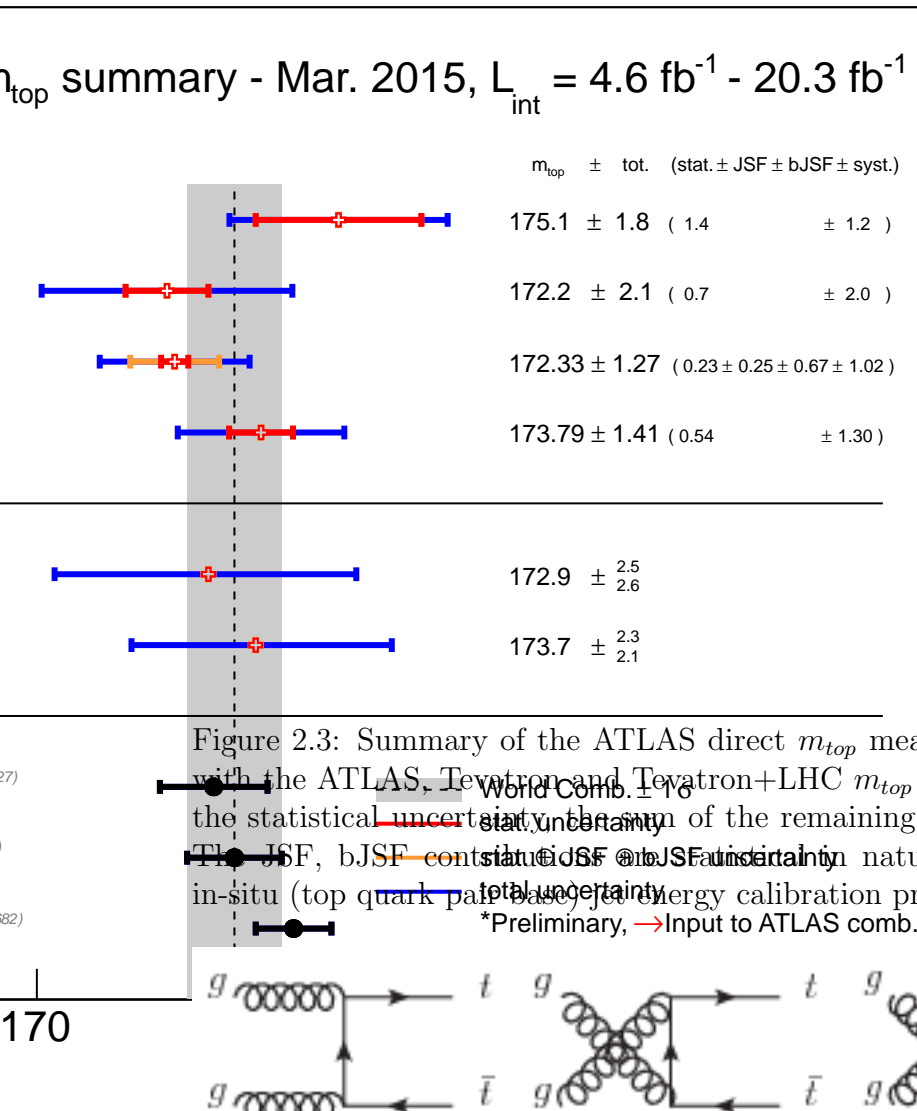
AHHH REPETITIVE

	particles			spin	electric charge
Quarks	$(u, d)_L$	$(c, s)_L$	$(t, b)_L$	$(\frac{1}{2}, \frac{1}{2})$	$(+\frac{2}{3}, -\frac{1}{3})$
	u_R	c_R	t_R	$\frac{1}{2}$	$+\frac{2}{3}$
	d_R	s_R	b_R	$\frac{1}{2}$	$-\frac{1}{3}$
Leptons	$(\nu_e, e^-)_L$	$(\nu_\mu, \mu^-)_L$	$(\nu_\tau, \tau^-)_L$	$(\frac{1}{2}, \frac{1}{2})$	$(0, -1)$
	e_R^-	μ_R^-	τ_R^-	$\frac{1}{2}$	-1
Gauge bosons	g W^\pm and Z			1	0
	γ			1	± 1 and 0
Scalar boson	H			0	0

Table 2.1: Spin and charge of particles in the SM.

	Particle	Mass
Leptons	e	0.511 MeV
	μ	105 MeV
	τ	1777 MeV
Gauge bosons	W^\pm	80.2 GeV
	Z	91.19 GeV
	H	126 GeV
Quarks	up (u)	1.7-3.3 MeV
	down (d)	4.1-5.8 MeV
	charm (c)	1.18-1.34 GeV
	strange (s)	70-120 MeV
	top (t)	173.34 ± 0.76 GeV [?]
	bottom (b)	4.18 ± 0.03 GeV
Hadrons	p	938 MeV
	n	939 MeV
	π^\pm	139.6 MeV
	π^0	135.0 MeV

Table 2.2: Mass of particles in the SM, taken from Ref. [?].

Figure 2.4: Feynman diagrams for $t\bar{t}$ production at leading order QCD

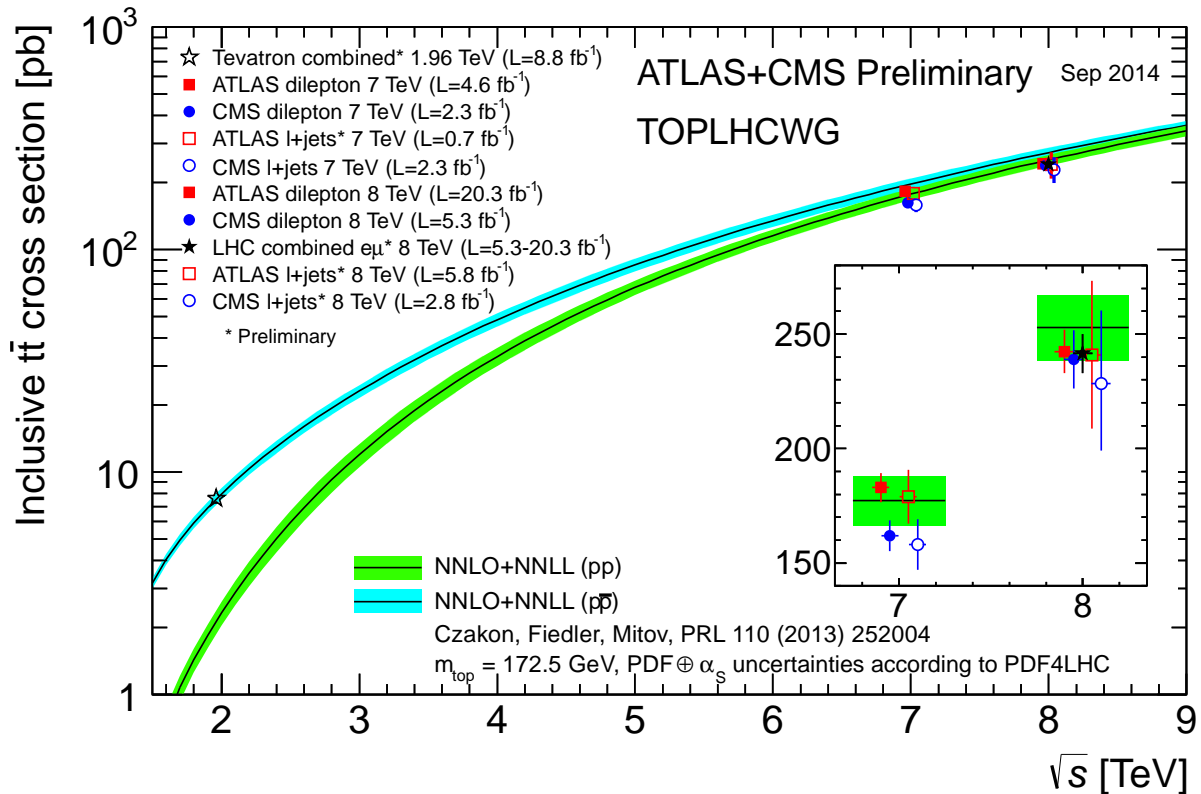


Figure 2.5: Summary of LHC and Tevatron measurements of the top-pair production cross-section as a function of the centre-of-mass energy compared to the NNLO QCD calculation complemented with NNLL resummation (top++2.0). The theory band represents uncertainties due to renormalisation and factorisation scale, parton density functions and the strong coupling. The measurements and the theory calculation is quoted at $m_{top}=172.5$ GeV. Measurements made at the same centre-of-mass energy are slightly offset for clarity.

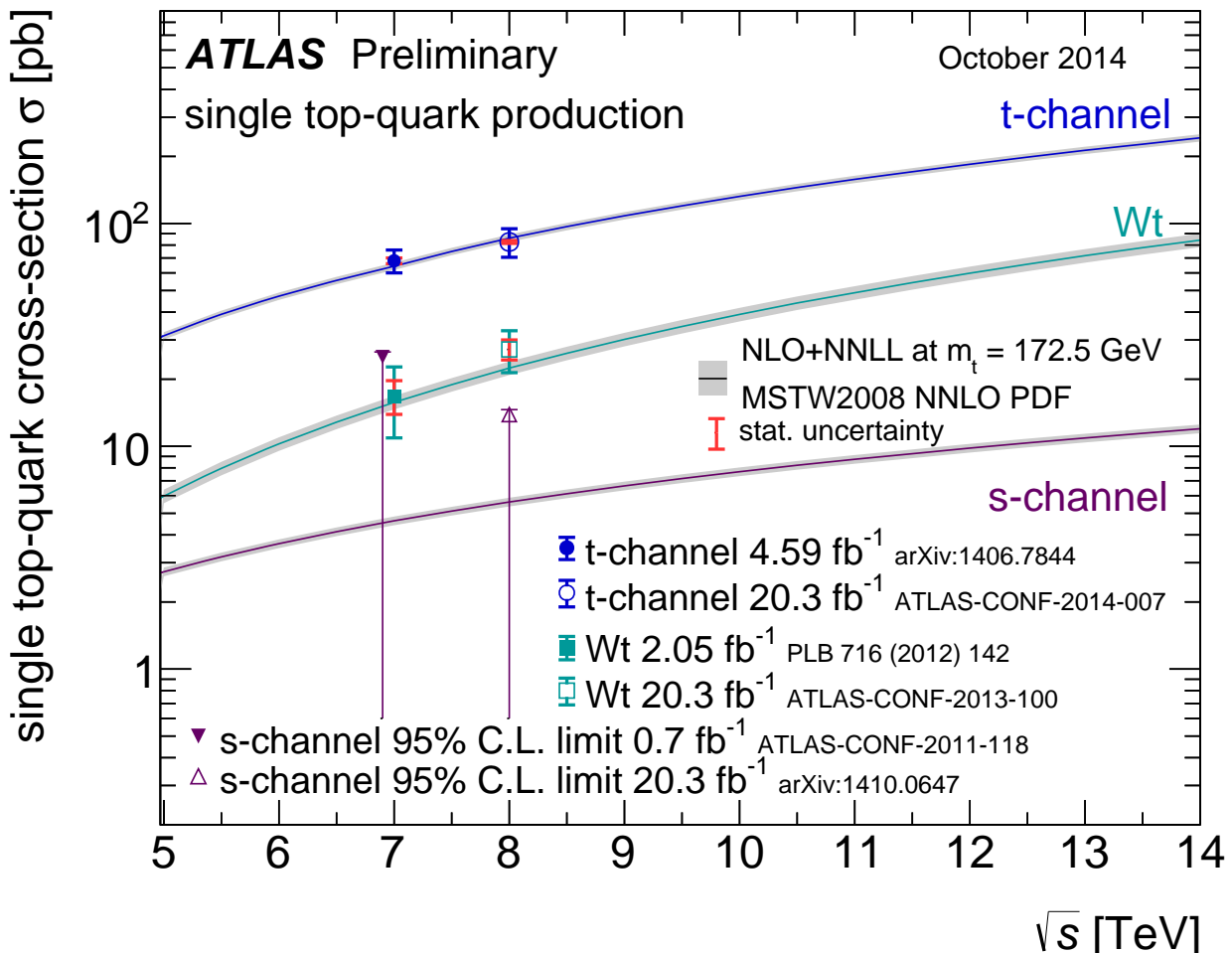


Figure 2.6: Summary of ATLAS measurements of the single top production cross-sections in various channels as a function of the center of mass energy compared to a theoretical calculation based on NLO QCD complemented with NNLL resummation. For the s -channel only an upper limit is shown.

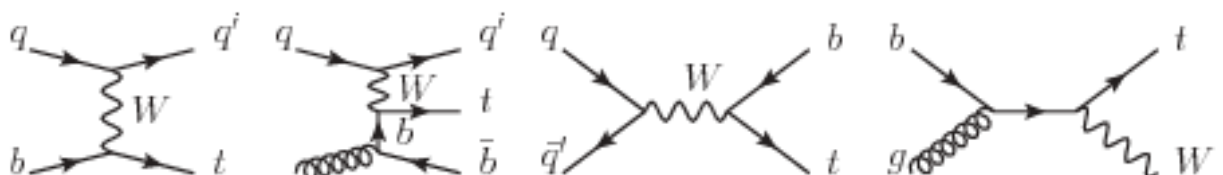


Figure 2.7: Feynman diagrams for single top quark production at leading order QCD. From left to right: t -channel production as flavor excitation; t -channel production as W -gluon fusion; s -channel production; Wt -channel production.

Chapter 3

Analysis strategy

This thesis presents a measurement of the multiplicity and differential cross section for additional (a.k.a. extra) jets produced in association with top quark decay products as a function of jet p_T . Jets are selected from the $R = 0.4$ anti- k_t collection and are calibrated using the final 2012 calibration. These additional jets are ordered in transverse momentum and labeled by *rank i*, such that $i = 1$ represents the leading (highest transverse momentum), $i = 2$ the subleading jet, etc.. The cross sections $\frac{1}{\sigma_{e\mu+2 \text{ } b\text{-jets}}} \frac{d\sigma_{\text{jet},i}}{dp_T}$ for $i = 1$ through $i = 4$ are measured and the multiplicity is measured for the number of jets $N_{\text{jets}} = 1$ through $N_{\text{jets}} = 4$ and inclusively for $N_{\text{jets}} \geq 5$. Here $\sigma_{e\mu+2 \text{ } b\text{-jets}}$ is the fiducial production cross section for events containing a high p_T electron, a high p_T muon and two tagged b -jets, where all four objects are required to pass the fiducial selection: $p_T > 25$ GeV and pseudorapidity $|\eta| < 2.5$, and where the additional jets in the event are required to have $p_T^i > 25$ GeV and $|\eta^i| < 4.5$. Thus $\int \frac{1}{\sigma_{e\mu+2 \text{ } b\text{-jets}}} \frac{d\sigma_{\text{jet},i}}{dp_T} dp_T^i$ gives the fraction of the accepted events that contain at least i jets.

The event selection employed here closely matches that used in the ATLAS 8 TeV cross section measurement[?]. The event rates and background estimates obtained are consistent with those obtained for that analysis and result in a sample with a $\gtrsim 99\%$ purity for the dilepton plus two b -jet final state. More than 95% of the events that pass the reconstruction selection cuts also pass the truth fiducial requirements.

Reconstructed jets not from the primary collision are called *unmatched jets* and treated as background. Their origin can be studied using simulated samples. In the baseline MC simulation, $\sim 4\%$ of the events contain at least one reconstructed calorimeter jet that cannot be matched to a jet reconstructed from truth particles. The largest source of these unmatched jets is pileup interactions. A second source is attributable to detector effects which result in a single truth jet being reconstructed as two jets in the detector or where the separation ΔR between the reconstructed and truth jet exceeds the matching cuts. The rate of unmatched jets is determined as a function of jet rank and p_T and is subtracted from the reconstructed distribution before that distribution is unfolded.

The unfolding procedure used to correct the background-subtracted extra jet p_T distri-

butions to the true spectra takes reconstruction efficiency and resolution effects into account. For events that pass the fiducial requirements at both the truth and the reconstruction level, a response matrix that maps between truth and reconstruction p_T and jet ordering is constructed using simulated data. The reconstructed spectrum is corrected for migration of jets with truth p_T below the 25 GeV cut but reconstructed p_T above it using a correction factor obtained from simulated data. Because the ordered full p_T distributions are corrected with a single unfolding matrix, cases where the relative rank of two reconstructed jets differs from their associated truth jets are properly treated in the unfolding.

The unfolded jet p_T spectra provide unbiased measurements of the true transverse momentum distributions of the ordered jets for events passing the reconstruction-level event selection cuts. However, they do not provide an unbiased measurement of the distributions for events passing the truth fiducial selection. While most events that pass the reconstruction requirements also pass the selection cuts at truth level, the inverse is not the case. Only about 25% of the events passing the truth selection also pass reconstruction. Furthermore, the event selection efficiency depends on the kinematics of the top decays; regions of phase space where the top decay products have higher p_T are more likely to pass the selection criteria. The resulting bias on the unfolded distribution is corrected using bin-by-bin factors obtained from MC. These correction factors typically differ from unity by less than 10%.

The distribution obtained after applying this final correction is $\frac{1}{\sigma_{e\mu+2 \text{ b-jets}}} \frac{d\sigma_{\text{jet},i}}{dp_T}$. The multiplicity is obtained by integrating the differential p_T distribution separately for each jet rank.

Chapter 4

The ATLAS detector and the LHC

4.1 The Large Hadron Collider

The Large Hadron Collider (LHC) ?? is the largest and most powerful particle collider that has ever been built. Construction of the LHC involved a collaboration of more than 10,000 scientist from more than 100 countries and was completed in 2008, after a decade of work. The cost of the machine alone is about 5 billion USD (3 billion Euro).

The European Organization for Nuclear Research (CERN) built the LHC in a tunnel underneath the border of France and Switzerland, near the city of Geneva. The LHC occupies a large tunnel 27 km in circumference that was originally constructed in the 1990s for the Large Electron Positron collider (LEP). Hadrons (either protons or ions) are accelerated and focused into two beams traveling in opposite directions around this tunnel. These beams are then made to collide with very high energy at one of the four collision points along the ring where their paths intersect. Each of these points is home to one of the four main LHC experiments: A Large Ion Collider Experiment (ALICE) [?], ATLAS [?], the Compact Muon Solenoid (CMS) [?], and the Large Hadron Collider beauty (LHCb) experiment [?]. ALICE is a detector that looks at collisions of lead ions to study the properties of quark-gluon plasma. ATLAS is a general-purpose detector that looks for a wide range of possible new types of physics, including the Higgs boson, supersymmetry (SUSY) and extra dimensions. CMS is an additional general-purpose detector, designed and run independently from ATLAS, but with the same goals in mind. LHCb is a detector specially designed to study the asymmetry between matter and anti-matter in the interactions of B-particles. Figure 4.1 shows a aerial view diagram with the locations of these four experiments along the LHC ring. The location of the LHC ring in relation to the city of Geneva and the French-Swiss border is also illustrated.

The main goal of the LHC is to investigate unsolved questions in our current understanding of particle physics, such as the details of the Higgs mechanism, the existence of new particles from SUSY or extra dimensions and the source of dark matter and dark energy.

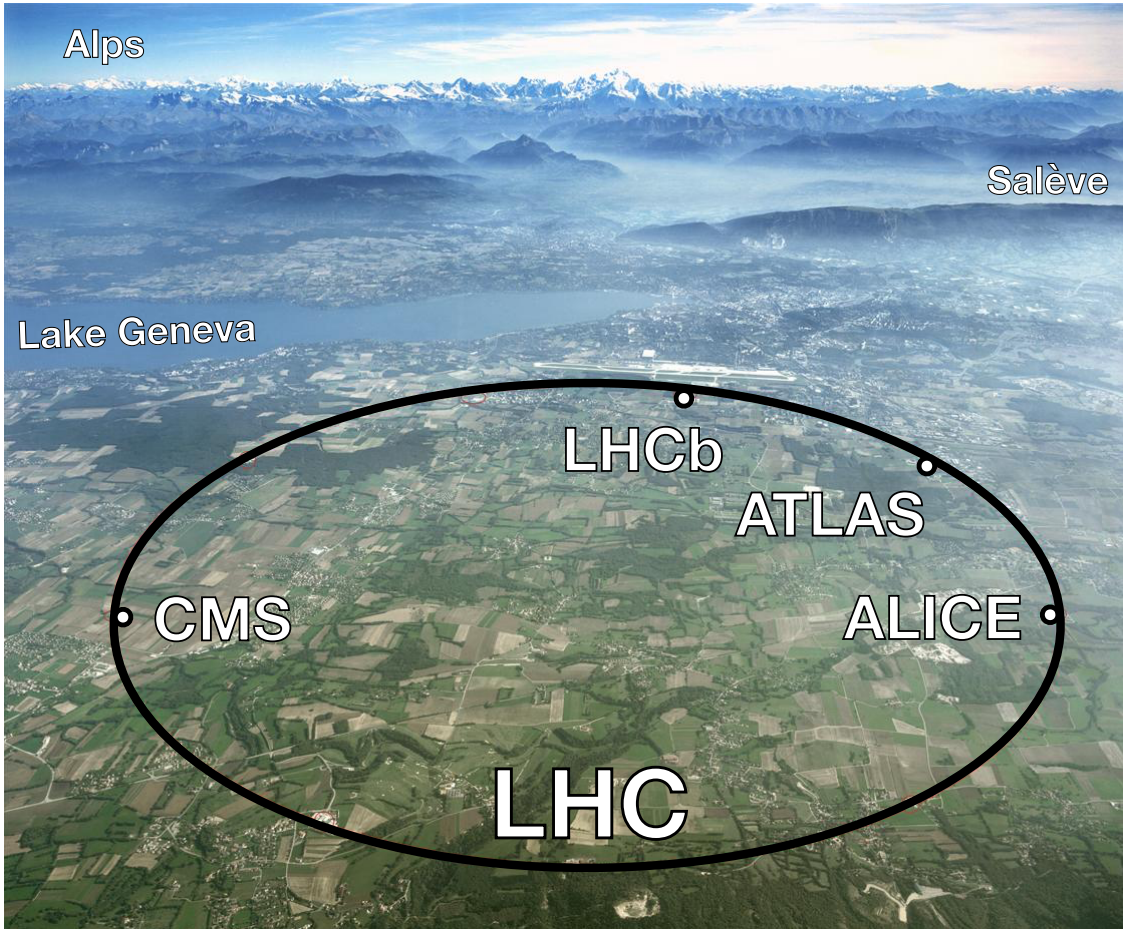


Figure 4.1: The location of the four main LHC experiments: ALICE, ATLAS, CMS and LHCb. The LHC tunnel is 27 km in circumference, situated underneath the border of France and Switzerland, near the city of Geneva, as shown. [?].

4.1.1 Accelerator Complex

A succession of machines known as the *accelerator complex* accelerate particles to increasingly higher energies [?], shown in Figure 4.2. First, an electric field is used to strip protons from atoms in a simple bottle of hydrogen gas. Then, the first accelerator in the chain, Linac 2, accelerates protons to 50 MeV. Next, the beam is injected into the Proton Synchrotron Booster (PSB) and then the Proton Synchrotron (PS), which accelerate the protons to 1.4 GeV and 25 GeV respectively. After that, the Super Proton Synchrotron accelerates the protons to 450 GeV. The last step in the chain is the LHC; from the SPS, protons are transferred into the two beam pipes of the LHC and accelerated in opposite direction. Filling each of the rings of the LHC takes 4 minutes and 20 seconds, and it takes another 20 minutes to accelerate each beam to its final energy of 4 TeV. The same two beams will circle for many hours.

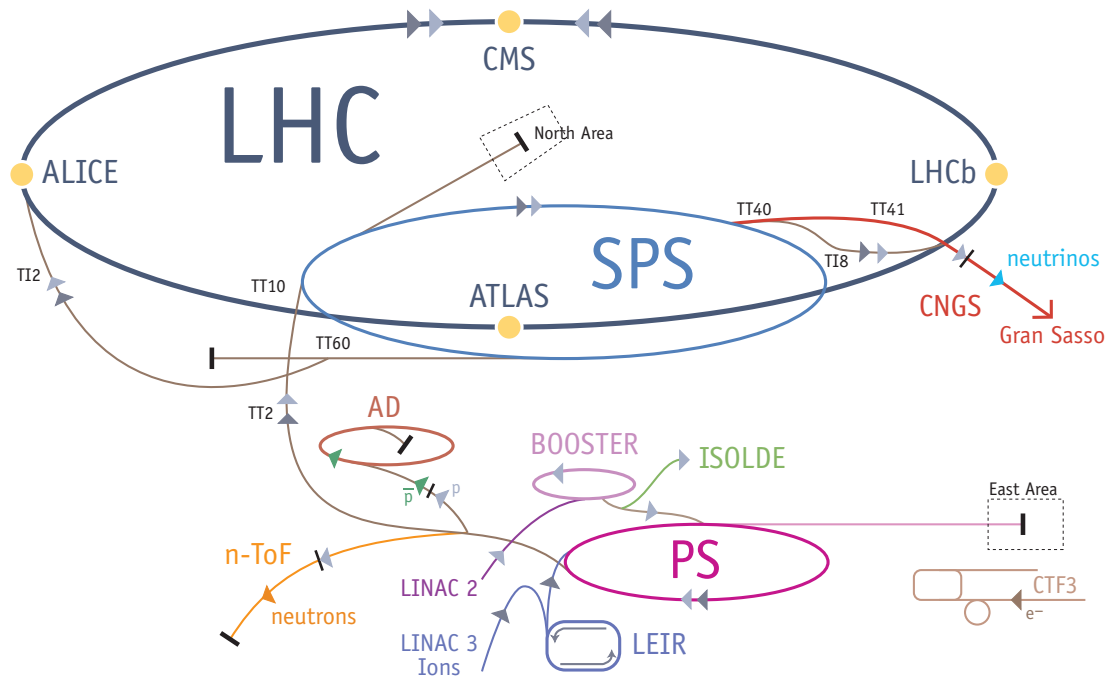


Figure 4.2: The LHC accelerator complex boosts particles to increasingly higher energies before reaching the LHC. The particle beams are accelerated successively by Linac 2, the Proton Synchrotron Booster (PSB), the Proton Synchrotron (PS), the Super Proton Synchrotron (SPS) and then finally enter the LHC rings [?].

Inside the LHC, the beams travel in opposite directions around separate rings called *beam pipes* (or beamline), which are tubes kept at ultrahigh vacuum. The beams are directed by a collection of very strong superconducting electromagnets, including 1232 dipole magnets and 392 quadrupole magnets. Superconduction requires the magnets to be cooled to -271.3 C. A distribution system of liquid helium keeps the magnets cool. The 15 meter long dipole magnets steer the beams around the ring, while the 5-7 meter long quadrupole magnets focus the beams before collision. The protons in the beams circulate in well-defined groups called *bunches*. Each bunch consists of approximately 10^{11} particles, and each beam has 2808 bunches. This bunch structure maximizes the chances of collisions since multiple protons have the chance to collide each crossing. In 2012, bunch crossings occurred every 50 nanoseconds.

4.2 Beam conditions

Due to the Radio Frequency (RF) fields in the accelerating cavities, the proton beams are segmented into groups of protons called *bunches*. Each beam contains 2808 bunches, and

each bunch contains 1.7×10^{11} protons. Many protons are included per bunch to maximize the probability of a proton-proton collision for a given bunch crossing. A bunch crossing occurred every 50 nanoseconds during operations in 2012.

Given two equally bunched beams, the instantaneous *luminosity* (\mathcal{L}) is given by:

$$\mathcal{L} = f \frac{n_1 n_2}{4\pi\sigma_x\sigma_y}, \quad (4.1)$$

where $f = 11\,245.5$ Hz is the collision frequency of the LHC beams; n_1 and n_2 are the numbers of protons in each beam; and σ_x and σ_y are the RMS beam widths in the horizontal (bend) and vertical directions.[?] The maximum instantaneous luminosity of the LHC in 2012 was 7.7×10^{33}

The instantaneous luminosity must be integrated over time because the beam conditions that go into Equation 4.1 are always changing over the duration of a run. The integral over time and varied beam conditions is called the integrated luminosity and can be used to relate the number of events N for a given physics process to its cross section σ :

$$N = \sigma \times \int \mathcal{L}(t) dt \quad (4.2)$$

In 2012, the total integrated luminosity of the LHC was 20.3^{-1}fb with uncertainty of 2.8% [?]. The cumulative luminosity recorded over the course of 2012 is shown in Figure 4.3.

The beam conditions also determine the number of proton-proton interactions that occur in each bunch crossing. When a single bunch crossing produces multiple separate proton-proton collisions, these events are referred to as *pile-up*. Pile-up presents a significant challenge since it can rapidly increase the combinatoric complexity of reconstructing events and quickly degrades the performance of the reconstruction algorithms. In 2012, pile-up was much larger than anticipated. Figure 4.4 shows the mean number of interactions per bunch crossing for 2011 and 2012, demonstrating the substantial increase of pile-up events in the latter. Reconstruction challenges were overcome by optimizing the existing reconstruction algorithms, as well as new techniques for subtracting pile-up events from the physics of interest. Pile-up techniques used in this analysis will be discussed in the chapter on object selection.

4.3 Overview of the ATLAS detector

The ATLAS detector is a general purpose detector centered over one of the four interaction points of the LHC. The detector is cylindrical in shape with a diameter of 25 meters, a length of 46 meters and a weight of 7,000 tons; it contains around 100 million electronic channels and around 3,000 km of cables. Assembling the detector at CERN took 5 years and was completed in 2008. A schematic rendering of the ATLAS detector is shown in Figure 4.5.

In order to detect a wide range of physics in proton-proton collisions, ATLAS must measure the trajectory and energy of many different kinds of particles, including electron, muons,

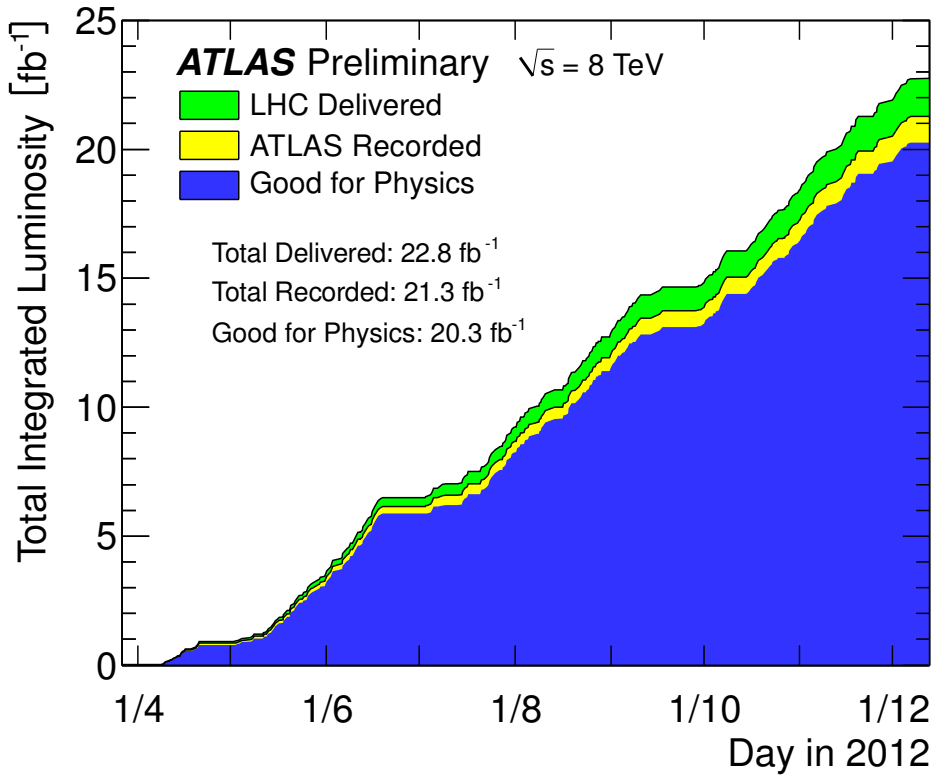


Figure 4.3: Cumulative luminosity versus time delivered to (green), recorded by ATLAS (yellow), and certified to be good quality data (blue) during stable beams and for pp collisions at 8 TeV centre-of-mass energy in 2012. Luminosity can be lost due to data acquisition inefficiency or other effects.

photons, kaons, protons and neutrons. Once these stable final-state particles are identified, information about the heavier, unstable particles can be inferred. This process is called *reconstruction* and is discussed in detail in Chapter 5.

ATLAS consists of specialized subdetectors designed to capture different phenomena. These subdetectors are arranged as increasingly larger concentric cylinders around the interaction point (IP) where the LHC proton beams collide. There are three main specialized sub-systems: the *inner detector* (ID), which is located just outside the beamline and uses silicon and transition radiation systems to track the trajectory of charged particles; the *calorimeters*, which is located radially outward from the ID and designed to measure the energy of particles with a shower sampling method; and the *muon system*, which is located farthest from the IP and measures muon momentum. Details of the subdetectors will be explored below. An overview of interaction of different types of particles with the subdetectors as they travel through the detector is illustrated in Figure 4.6.

In addition to the subdetector, ATLAS has a magnet system that bends the trajectory of charged particles as they travel through the ATLAS detector. This allows the particle's

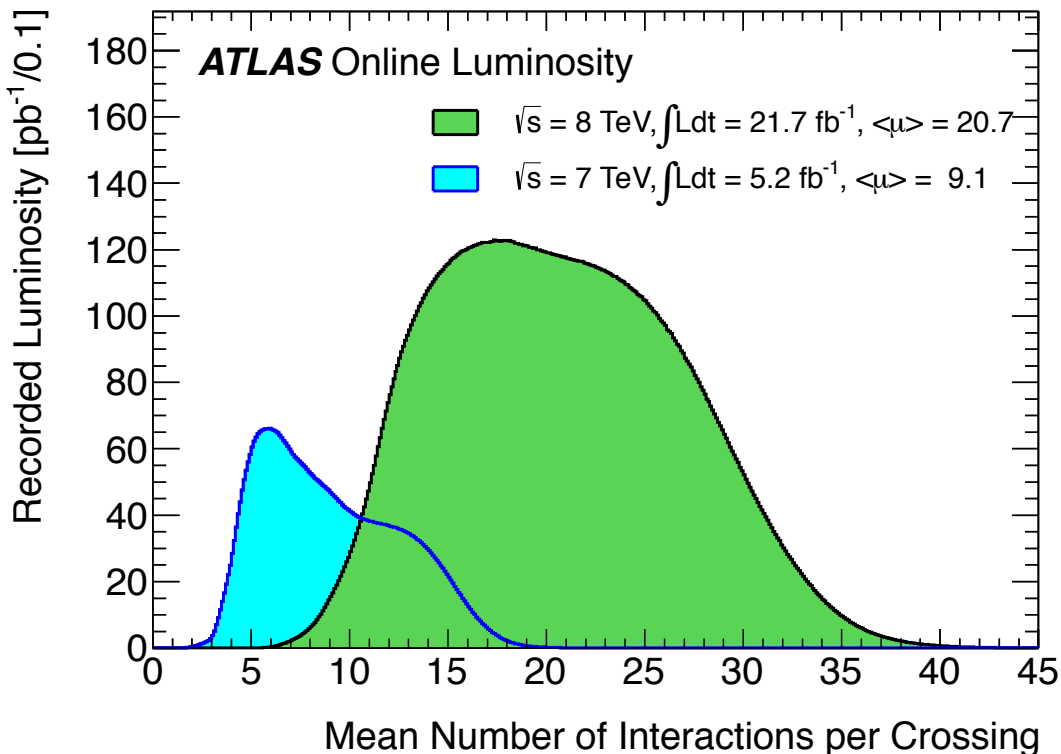


Figure 4.4: Luminosity-weight distribution of the mean number of interactions per bunch crossing. Both the full data from the 2011 and 2012 pp runs at the LHC are shown.

momentum to be precisely calculated using the classical Lorentz force equation. The magnet system consists of a double configuration. Just outside the ID is a solenoidal magnet that produces a field of approximately 2 Tesla. A large toroidal magnet within the outermost part of the detector produces a 1-2 Tesla field.

4.3.1 Coordinate system

ATLAS uses a right-handed coordinate system with its origin at the IP in the center of the detector, which is illustrated in Figure 4.7. The z -axis along the beamline with the positive direction counter-clockwise around the LHC. The $x - y$ plane is defined such that the coordinate system is right-handed, with the x -axis pointing from the IP to the center of the LHC, and the y -axis pointing upwards. This plane is usually referred to as the transverse plane, since it is perpendicular to the beamline. Cylindrical coordinates, r and ϕ , are used in the transverse plane with ϕ defined as the azimuthal angle around the beamline. Instead of the polar angle from the beamline, θ , pseudorapidity is typically used and can be defined

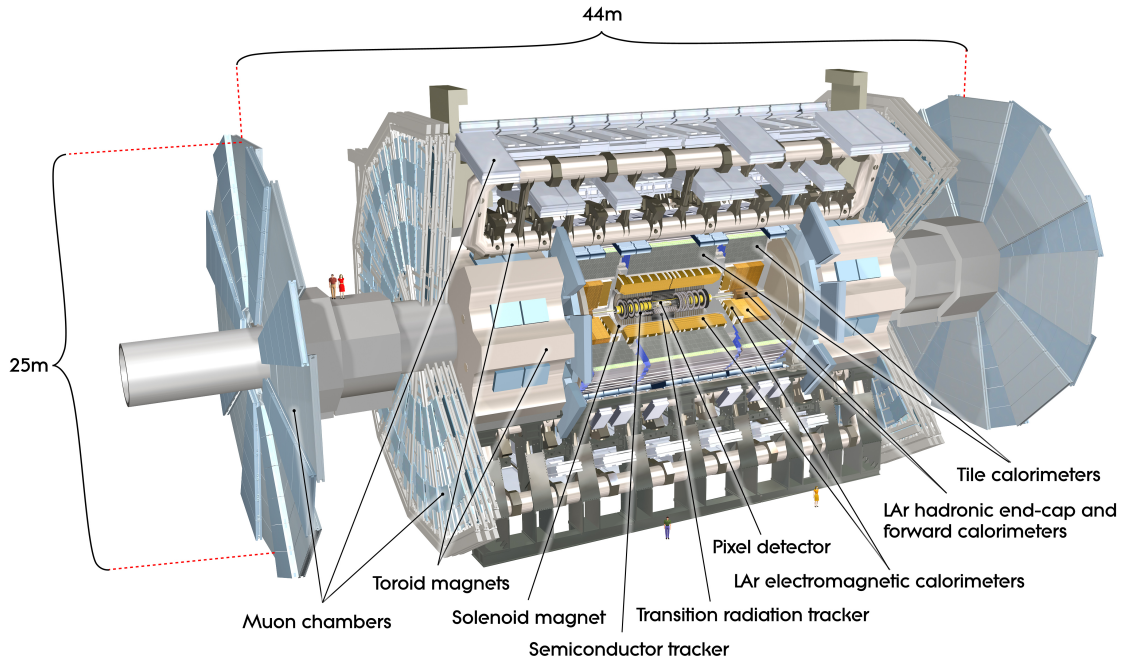


Figure 4.5: Computer generated illustration of the whole ATLAS detector detector, with various subdetectors highlighted[?].

as:

$$\eta = -\ln(\tan \frac{\theta}{2}) \quad (4.3)$$

The pseudorapidity is used because in the limit of a massless particle, it is invariant with respect to Lorentz boosts along the beamline. Then, solid angle distances ΔR can be measured with the difference in pseudorapidity and azimuthal angle:

$$\Delta R = \sqrt{\Delta\phi^2 + \Delta\eta^2} \quad (4.4)$$

4.4 Inner detector

The ID is a series of detectors that functions as a tracking system to measure the momenta and trajectory of charged particles. This also allows reconstruction of the primary and secondary vertices of the collision. The innermost part of the entire detector is the pixel detector, 3 layers of silicon that accurately measure the three-dimensional spatial position of charged particles. Next is the Semiconductor Tracker (SCT), 4 layers of double-sided silicon strip modules which accurately measure tracks in the $r - \phi$ plane and are double sided to provide stereo information along the z axis. The outermost component of the ID is

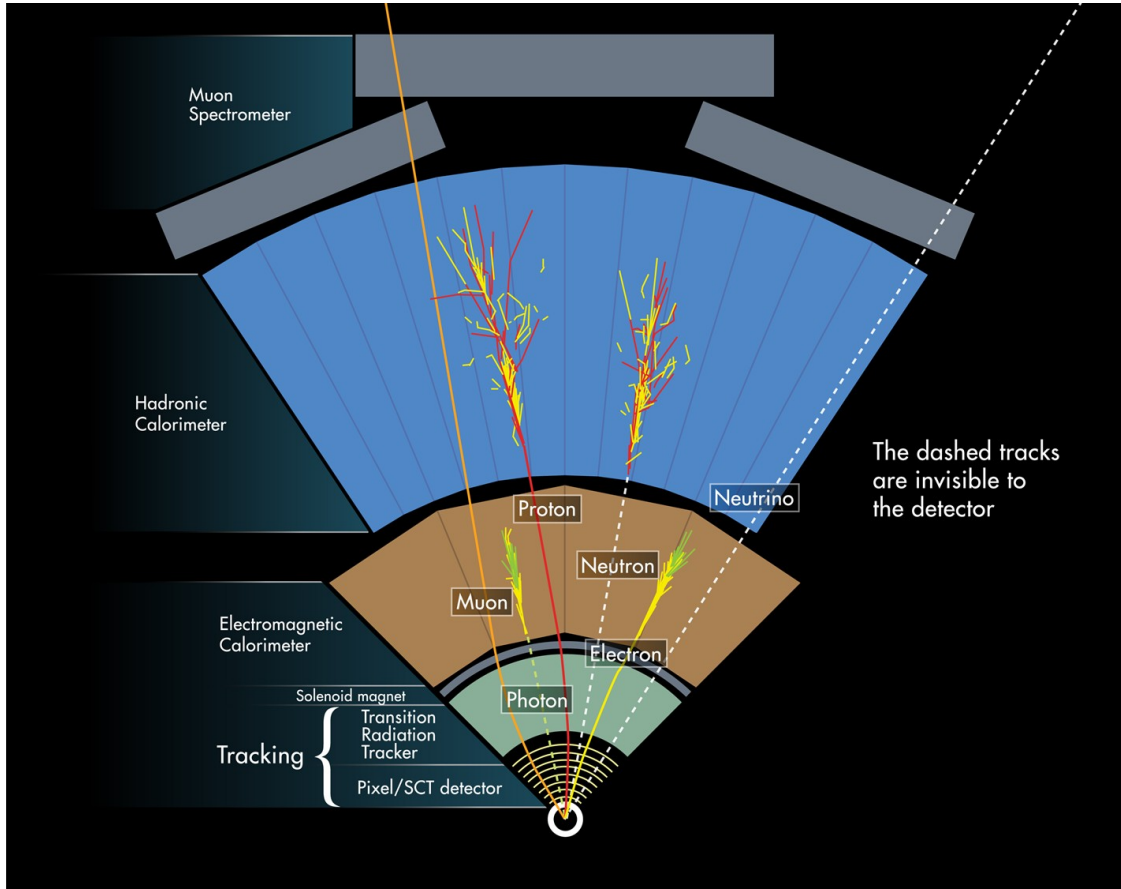


Figure 4.6: A computer-generated image representing how the ATLAS detector functions. The transverse paths of different types of particles are shown interacting with different elements of the detector[?].

the Transition Radiation Tracker (TRT), straw tubes filled with Xenon gas interleaved with polymer layers which provides additional trajectory measurement and differentiate between electron and hadrons. Figure 4.8 shows a schematic outline of the entire inner detector, and Figure 4.9 illustrates a cut-away view of the inner detector barrel.

4.4.1 Pixel detector

The pixel detector is located closest to the beamline and is designed to provide high granularity in a high radiation environment. Measuring trajectories closest to the interaction point is important for constructing the secondary vertex, necessary for the b -tagging of jets used in this analysis.

The pixel detector has 3 barrel layers and three endcap disks on each side of the barrel. The barrel layers are located 50.5 mm, 88.5 mm and 122.5 mm radially from the interaction

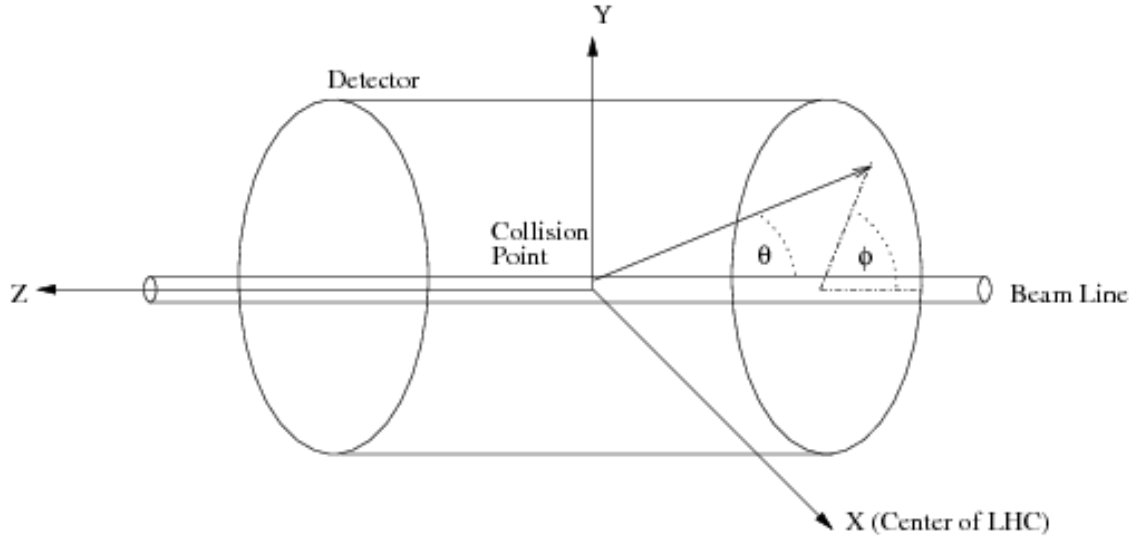


Figure 4.7: Illustration of the ATLAS coordinate system[?].

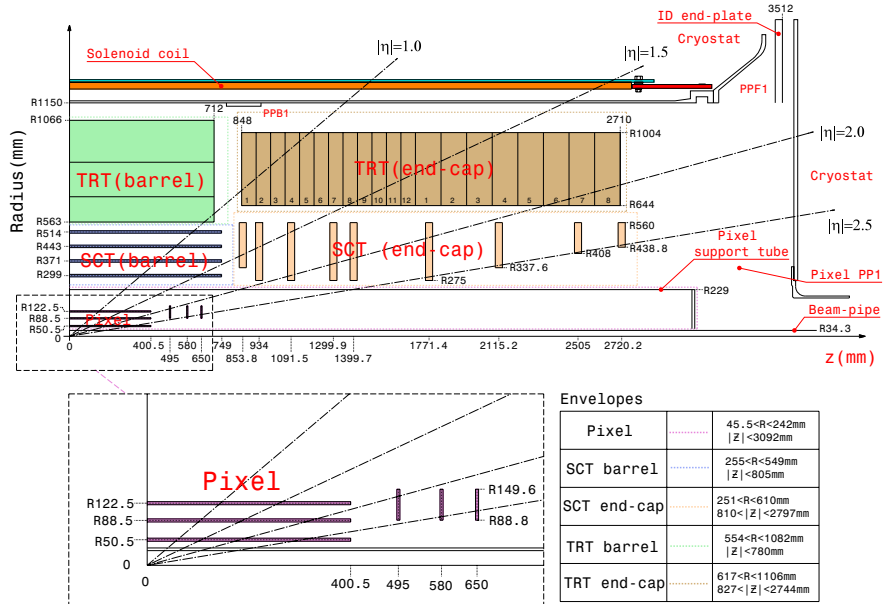


Figure 4.8: Schematic view of the Inner Detector: an $r - z$ slice of the cylindrical barrel, disc endcaps with support tubes, and the solenoid magnet. Lines of constant η are drawn [?].

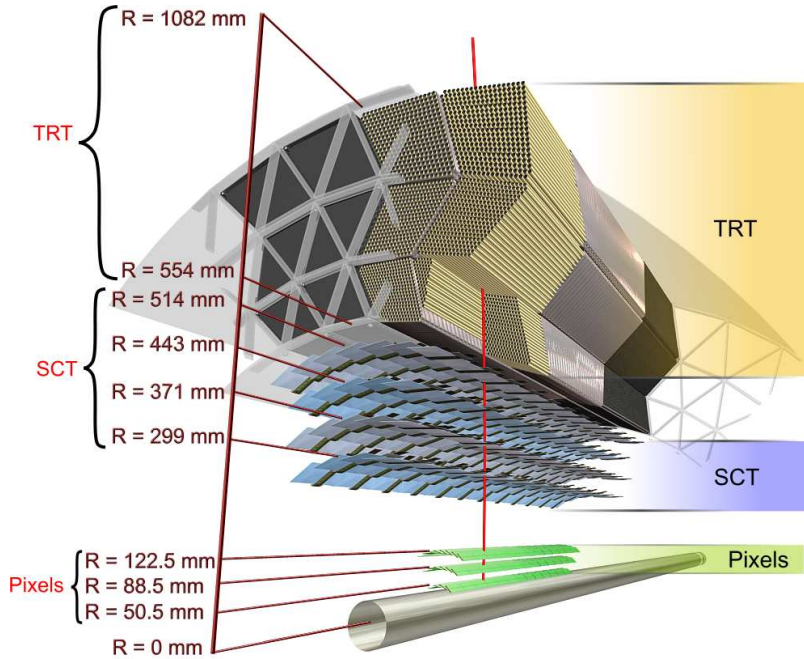


Figure 4.9: A diagram of the barrel of the Inner Detector: the three layers in the Pixels, the four layers in the SCT, and the many layers of the TRT [?].

point. The endcaps sit at 495 mm, 580 mm and 650 mm away from the interaction point. Together, they provide coverage up to $|\eta| = 2.5$.

Each silicon pixel in these layers is a p-n junction built of n-type bulk with both p⁺ and n⁺ impurities. The additional n⁺ implants allow the pixels to operate even after the inversion of the bulk from n-type to p-type caused by the high radiation dose. The size of each pixel is $50 \times 400\mu\text{m}^2$ with the longer side along the z direction. This allows charged particle hit resolution of approximately $115\mu\text{m}$ in the direction of the z axis and $10\mu\text{m}$ in the direction of the transverse plane.

Pixels are bump-bonded to front-end readout chips, with a grid of 2880 pixels connected to each chip. Front-end chips are grouped into rectangular *modules* of dimension $19 \times 63\mu\text{m}^2$. Modules in the barrel layers are arranged into long structures parallel to the beamline called *staves*. Staves are tiled at 20° with respect to the radial direction and overlapped to provide full azimuthal coverage. Endcap modules are arranged into petals and then into wheels, with the sensing element perpendicular to the beam axis. These supporting structures also host power, clock, command and data lines to and from each module. Full coverage is ensured in the endcaps by alternating the placement of the sensors on the front and back of the wheel. The arrangement of the barrel and endcap layers ensures that charged particles with $|\eta| < 2.5$ will pass through at least three pixels.

4.4.2 Semiconductor Tracker

The SCT surrounds the Pixel detector and also employs silicon detector elements, using micro-strips instead of pixels. The strips are arranged in four double layers, with the pairs arranged at small angles relative to each other, to make a three-dimensional measurement. The SCT has 4 barrel layers and 2 endcaps, each with 9 disks.

The SCT is made of single-sided p-in-n sensors of thickness $285\mu\text{m}$ with readout strips. In the rectangular barrel sensors, the readout channels are arranged with a pitch of $80\mu\text{m}$ between them, and the trapezoidal endcap sensors have radial strips with a mean pitch of $80\mu\text{m}$. Modules are comprised of four sensors arranged in two layers aligned at a stereo angle of 40 mrad with respect to each other. This allows a single module to measure all three dimensions spatial position of a charged particle passing through both the front and back layers. The endcap wheels are arranged so that charged particles with $|\eta| < 2.5$ will pass through at least eight sensors. The 2112 modules in the barrel have resolution $17\mu\text{m}$ in $r - \phi$ and $580\mu\text{m}$ in z , and the 1976 endcap modules have resolution $17\mu\text{m}$ in $r - \phi$ and $580\mu\text{m}$ in r .

4.4.3 Transition Radiation Tracker

The outermost layer of the ID, the TRT extends the tracking volume to 1106 mm and also distinguishes between electrons and pions based on their transition radiation as they pass through. The TRT consists of straw drift tubes 4 mm in diameter filled with a Xenon gas mixture. At the center of each tube is a $35\mu\text{m}$ -wide anode tungsten wire held at ground potential. Charged particles ionize the gas inside the tube, then the electric field between the tube and the wire creates an ionization cascade, which can be used to infer the energy of the original particle.

The 351,000 tubes are arranged in a barrel and two endcaps. In the barrel, 73 layers of 144 cm long tubes are parallel to the beamline, with wires slit in half to allow separate measurements for positive and negative z . In the endcaps, the 160 layers of 37 cm long tubes are arranged radially. The intrinsic resolution of the TRT in the barrel is $130\mu\text{m}$ in $r\phi$ with coverage up to $|\eta| < 2.0$. A charged particle passes usually through 30 or more tubes.

When charged particles pass through a polymer fibre mat sitting between the tubes, transition radiation may be produced. The photons from transition radiation produce an ionization cascade much higher than the signal for tracking minimum-ionizing particles. Therefore, TRT straws have two signal thresholds: a *high threshold* for transition radiation hits and a *low threshold* for tracking hits.

Transition radiation, produced when a charged particle crosses the boundary between two media of different dielectric constants, is proportional to the Lorentz γ of a particle. For an electron and charged pion of equal momentum, the electron is about 3.7 times more likely to produce transition radiation than the pion since its mass is 200 times smaller. Seven to ten high threshold hits are typical when an electron passes through the TRT.

4.4.4 Track reconstruction

Measurements from the three subdetectors of the ID are combined to make *tracks*, a description of the trajectory and momentum of each charged particle. The signals left in each layer by a charged particles as it traverses the detector are called *hits*. These hits are then reconstructed into tracks with the ATLAS tracking algorithm[?]. Tracks are required to have $p_T > 400$ MeV in order to be reconstructed.

The algorithm works first from the inside of the detector outward. Pattern recognition is used to make the pixel detector hits into three-point track candidates. Then, a Kalman filter is used to add SCT hits radially outward. After ambiguities like missing or shared hits are resolved, the tracks are extended into the TRT. Tracks must have $p_T > 400$ MeV to be reconstructed. After this inside-out algorithm has been completed, an outside-in algorithm is run on the unused hits, to reconstruct secondary tracks left by particles not originating directly from the IP.

Since charged particle tracks are bent by the magnetic field, the trajectory takes a helical form and can be expressed by 5 parameters:

- d_0 is the transverse impact parameter, equal to the distance of closest approach in the plane transverse to the beam of the track to the primary vertex
- z_0 is the longitudinal impact parameter, equal to the z coordinate of the point of closest approach to the primary vertex
- ϕ_0 is the azimuthal angle of the trajectory at the point of closest approach to the primary vertex
- $\cos \theta$ is the cosine of the angle the track forms with respect to the beam
- q/p_T is the charge divided by the momentum in the transverse plane.

4.4.5 Vertex reconstruction

A vertex reconstruction algorithm determines if many tracks originate from the same pp collision[?, ?]. The vertices are reconstructed with an iterative fitting procedure. Initially, a vertex seed is created from a fit to the global maximum of the z coordinates of the tracks. Then, tracks are matched to the seed using a χ^2 algorithm. Incompatible tracks are used to seed a new vertex until all tracks are associated with a vertex.

Since several pp collisions are likely to occur for each bunch crossing, some of the tracks will be associated with secondary vertices from pile-up rather than the primary vertex (PV) from the hard collision. The PV is conventionally defined as the vertex with the highest track p_T^2 . In 2012, the average number of interactions per crossing was 20.7, as shown in Figure 4.4, so vertex reconstruction is essential for determining which particles came from pile-up. If a track isn't associated with the PV, it is typically considered pile-up. Figure 4.10 shows an event with 22 vertices, demonstrating the importance of tracking and vertexing in events with a lot of pile-up.

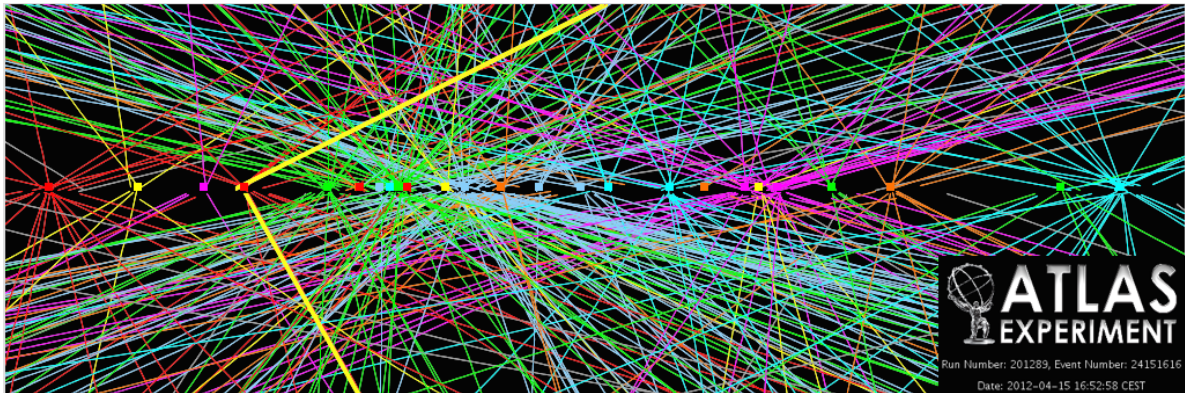


Figure 4.10: Display of a 2012 event with 25 reconstructed vertices [?].

4.5 Calorimeters

The calorimeter system stops and measures the energy of electrons, photons and jets with full coverage in ϕ and $|\eta| < 4.9$. This is done with separate electromagnetic and hadronic calorimeters, both with barrel and endcap components. A combined forward calorimeter provides high η measurements. ATLAS calorimeters are sampling calorimeters, which means that only part of the shower energy is observed. Absorbing material used to initiate showers is interleaved with active material for detecting the showers. The layout of the calorimeters can be seen in Figure 4.11.

4.5.1 Electromagnetic calorimeter

The EM calorimeter has alternating lead absorbers and liquid argon (LAr) active medium with kapton electrodes. The barrel component covers $|\eta| < 1.5$ and the endcap component cover $1.4 < |\eta| < 3.2$. A presample covering $|\eta| < 1.8$ measures showers starting before the calorimeter.

The barrel is segmented into three layers of decreasingly fine segmentation. The first and second layers are important for identifying shower shapes, so they are finely segmented. The first layer has a thickness of $4.3 X_0$, and the second layer has a depth of $16 X_0$, which usually contains the majority of the energy of the EM shower. The third layer is a shallow $2 X_0$ to capture any leftover energy after the first two layers. To provide prevent gaps in ϕ , the layers are bent into an accordion-like shape. A diagram of a barrel module is shown in Figure 4.12.

The endcap of the EM calorimeter has two layers, with the accordion shape oriented to prevent gaps in η .

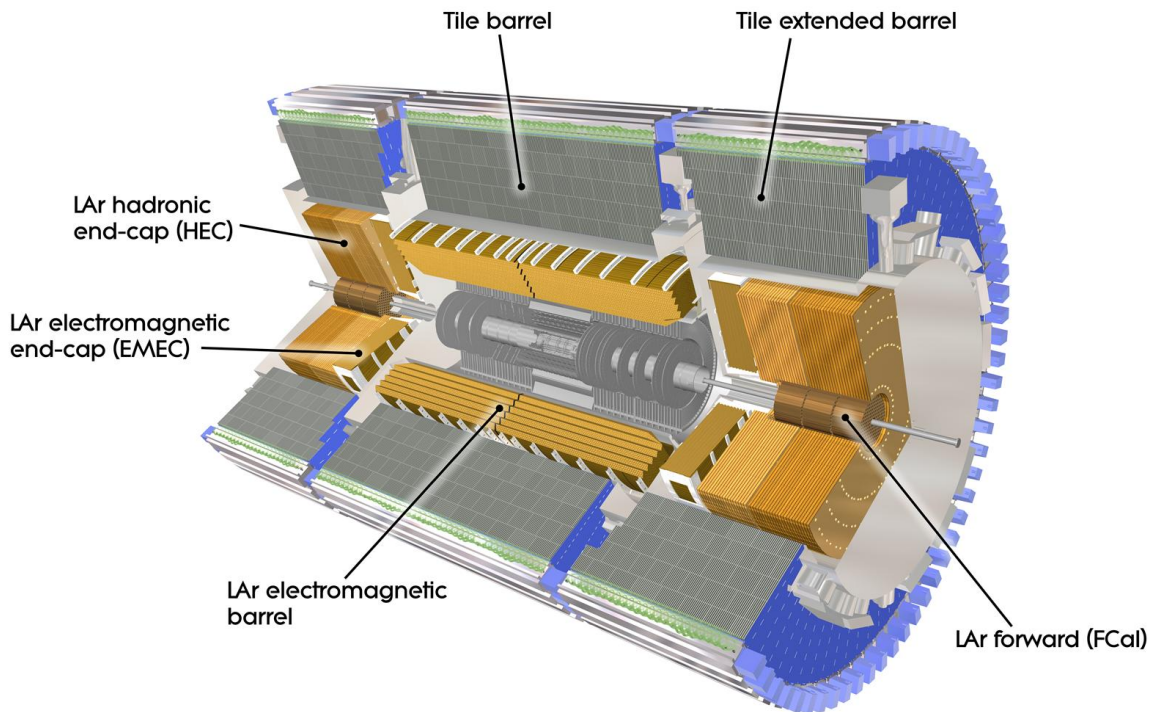


Figure 4.11: Cut-away view of the ATLAS calorimeter system [?].

4.5.2 Hadronic calorimeter

The hadronic calorimeter is divided into three components: the barrel tile calorimeter, which uses steel absorbers and scintillator tiles and covers $|\eta| < 1.7$; the Hadronic Endcap Calorimeter (HEC), which uses copper absorber and LAr active material and covers $|\eta| > 3.2$; and the forward calorimeter (FCal), which uses LAr active materials and covers $3.1 < |\eta| < 4.9$. The hadronic calorimeters are much coarser than the EM calorimeters because electrons and photons usually don't reach the radius of the hadronic calorimeters, so particle identification isn't a priority. Figure 4.13 shows a schematic of a hadronic tile module.

4.5.3 Clustering

In order to identify particles, information from the shape of the calorimeter showers are used. EM particles like photons and electrons produce narrow showers which are largely contained in the EM calorimeters. Hadrons produce broader showers and tend to travel farther into the hadronic calorimeters. Hadronic showers can also contain EM deposits from decays before the calorimeters, such as a neutral pion becoming two photons. In order to turn energy deposits in cells into clusters, information from all of the calorimeters is used

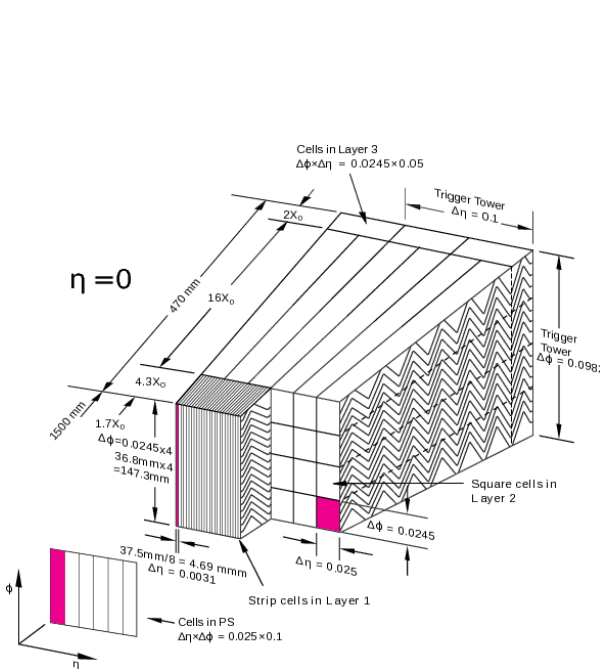


Figure 4.12: Diagram of an electromagnetic calorimeter barrel module[?].

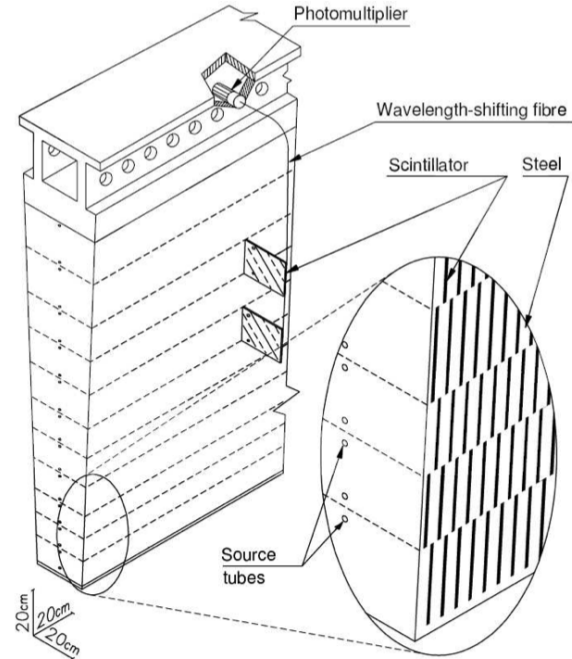


Figure 4.13: Diagram of a hadronic tile module[?].

as inputs to one of two principal algorithms[?]. The *sliding-window* algorithm clusters cells within fixed-sized rectangles. This algorithm is generally used for electron, photon and tau identification.

The second algorithm is the *topological* algorithm, which clusters together neighboring cells on the condition that the energy deposit in the cell is significantly more than the expected noise. This algorithm is generally used for jet and missing transverse energy reconstruction.

4.6 Muon System

The Muon System (MS) is the outermost subdetector, since muons are the only charged particles that can pass through the calorimeters [?]. The MS consists of a toroidal magnet system and a charged particle tracking system. The components of the muon system, highlighted in Figure 4.14, are designed to measure the path and energy of muons, particularly high p_T muons which may signal the presence of interesting physics.

The magnetic field provides the bending necessary for charge and momentum measurements and is comprised of three large air-core toroids. The toroid system has eight coils symmetrically around the beam and provides a magnetic field between 2 and 8 Tesla.

There are two types of tracking systems in the MS. The Monitored Drift Tubes (MDTs)

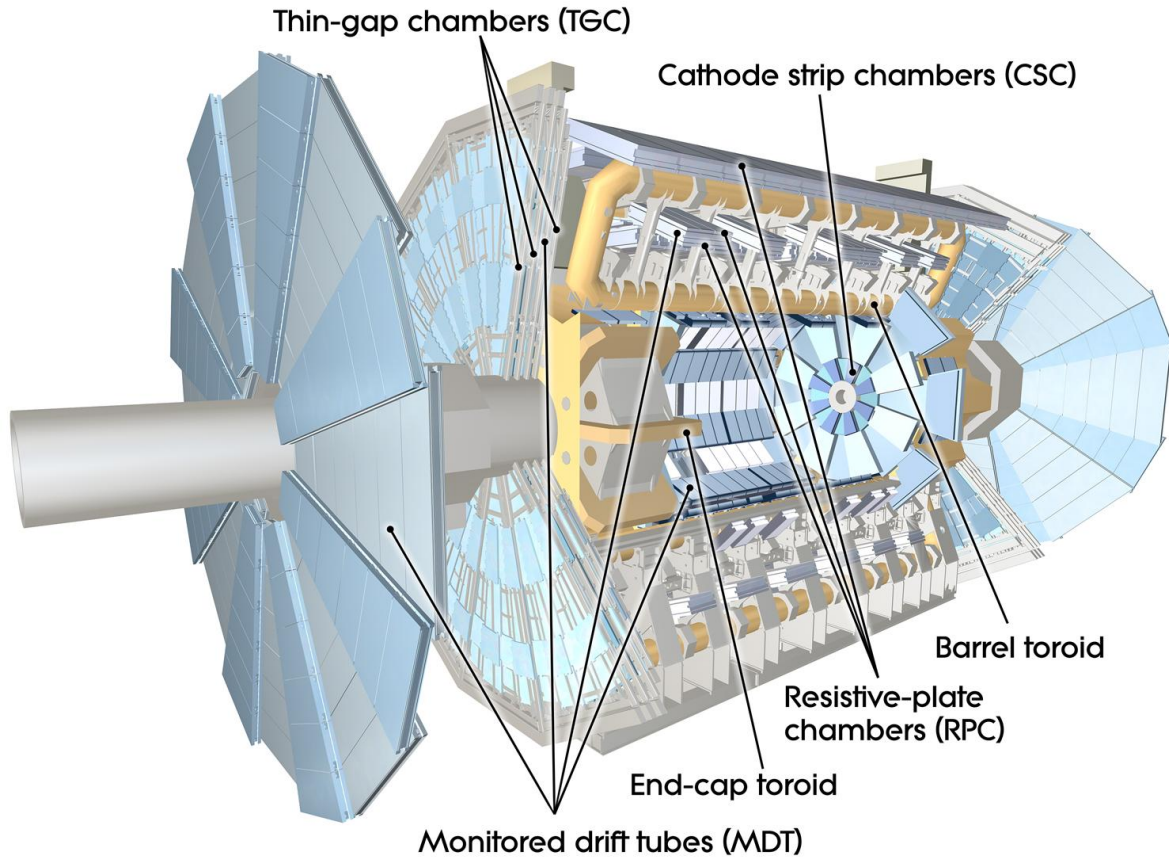


Figure 4.14: Diagram of the muon system[?].

precisely measure the track in the bending direction of the magnetic field and cover $|\eta| < 2.7$ in the outer barrel and cover $|\eta| < 2.0$ in the inner barrel. The Cathode Strip Chambers (CSCs) cover the forward region of the inner layer, $2.0 < |\eta| < 2.7$. The MDTs are pressurized aluminum drift tubes filled with a mixture of argon and carbon dioxide gas, 30 mm in diameter. Each chamber has 3-8 layers of tubes and a resolution of 35 μm per chamber. The MDTs are limited to a counting rate of 150 Hz/cm² and thus cannot be used in the forward region of the inner layer, where high muon rates are expected. This region instead uses CSCs for momentum measurement with better timing and spatial resolution. Two endcap wheels each have 16 chambers. Each chamber has 4 CSC planes. Each plane consists of two cathode strip planes sandwiching anodes wire. The arrangement of the CSCs gives resolution of 40 μm radial direction and 7 ns timing resolution.

The MS also has two types of trigger chambers: Resistive Plate Chambers (RPC) in the barrel and Thin Gap Chambers (TGC) in the endcaps. Just as with tracking, the endcap and barrel have different types of triggers due to the different rate and precision requirements. The barrel trigger system has 3 RPC layers, and the endcap trigger system has 4 TGC layers.

4.7 The trigger system

At hadron colliders, only a very small fraction of the proton-proton collisions result in events with interesting physics. The majority of events are low energy jets, which aren't useful for SM measurements or new physics searches. With bunch crossings every 50 ns, recording and reconstructing all of the collisions would take an unreasonable amount of data storage and computing power. Therefore, it is necessary to determine whether a collision is interesting immediately after it occurs with minimal analysis.

The process quickly filtering events to record only those of physics interest is called *triggering*. Processes which take place in the trigger system are referred to as *online*. Processes which take place after triggering, such as particle reconstruction, are called *offline*.

The ATLAS trigger scheme[?] consists of three stages: Level 1 (L1), Level 2 (L2), and Event Filter (EF). All collision candidates are first run through L1, an online hardware trigger that has coarse granularity by necessity. If events pass the L1 trigger, they are then passed through the offline software triggers, collectively called the High Level Trigger (HLT). The HLT is divided into two stages: L2 and EF.

Applying multiplicity and energy threshold requirements, L1 reduces the rate of events from 20 MHz (all pp collisions) to 75 kHz. The L1 trigger only looks at output from the calorimeters and muon system because the inner detector cannot process events at the rate required. In order to process events with the necessary speed, granularity in the calorimeter must be reduced and in the muon system, only the trigger chambers are read out. This reduction in granularity is illustrated in Figure ???. The maximum latency time to process at this level is $2.5 \mu\text{s}$. The data-acquisition system must keep track of which data correspond to which bunch crossing. This is really challenging since the time for measuring a signal shape in the EM calorimeter is $> 100 \text{ ns}$ and the time of flight through the MS is $> 25 \text{ ns}$, both longer than the time between events.

If the event passes the L1 trigger, then the L2 trigger looks at the distribution of energy deposits as Regions Of Interest (ROIs) identified by L1. The detector signals are compared to a menu of pre-programmed signatures that represent a potential physics object. For instance, a track and a cluster in the EM calorimeter might signal an electron. The L2 looks for these signatures in the ROIs by pulling information from all needed detectors.

For events with signatures that pass the L2 trigger, all information for the event is read out. Then the standard offline reconstruction algorithm is run. The event can then be evaluated in terms of the fully reconstructed physics objects to see if particle identities and kinematics match a menu of desired signatures. Finally, a decision about whether to record the event or not is made. This last stage of the triggering is called the Event Filter. The EF takes about 4s to process each event and can accept events at a rate up to 200 Hz.

4.7.1 Single electron trigger

The single electron trigger for used for 2012 is fully described in [?]. At L1, calorimeters are split into 0.1×0.1 towers and then 2×2 clusters are identify e/γ leptons using the

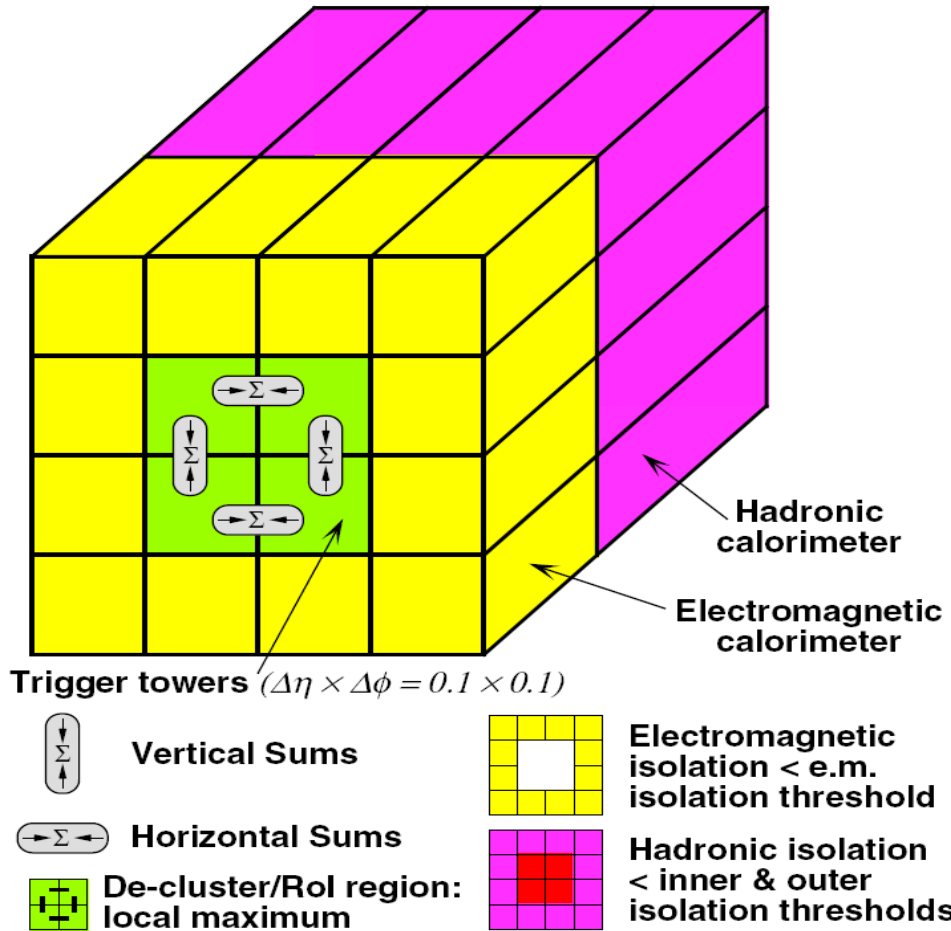


Figure 4.15: Schematic view of the calorimeter granularity available at the L1 trigger [?].

sliding window algorithm described in Section 4.5.3. Regions of 4×4 with clusters that meet isolation requirements are passed to the L2 trigger as ROIs. At L2, the position of the cluster is identified as the energy-weighted average of the cluster. Track reconstruction is then performed and if a track can be matched to the cluster, it is considered to come from an electron, not a photon. At both L2 and EF, electron candidates are required to pass selection criteria based on the calorimeter cluster and the track, such as cuts on the lateral width of the shower and hits in the inner pixel detector.

In this analysis, the logical OR of two triggers is used to identify electrons: a 24 GeV trigger with a loose track-based isolation requirement and a 60 GeV trigger without an isolation requirement. The isolation requirement specifies that the sum of the p_T of tracks within a cone of $\Delta R=0.2$ must be less than 10% the p_T of the electron. These trigger chains have thresholds that are maximally efficient for leptons passing offlines selections of $p_T > 25$ GeV.

4.7.2 Single muon trigger

The single muon trigger for used for 2012 is fully described in [?]. The muon trigger uses data from the RPCs in the barrel region and the TGCs in the outer region. At L1, the paths between hits in the trigger chambers are interpolated to identify muon candidates. If a hit pattern matches the requirements of the L1 trigger, the η and ϕ coordinates are passed to the L2 trigger as a ROI. At L2, the MDT and CSC information for the ROI are used to fit a higher quality track. Then, the track in the MS is combined with a track from the ID. Calorimeter data can be used to apply isolation requirements. Quality cuts are applied to the track to determine whether it passes the final trigger chain.

In this analysis, the logical OR of two triggers is used to identify muons: a 24 GeV trigger with a loose track-based isolation requirement and a 36 GeV trigger without an isolation requirement. The isolation requirement specifies that the sum of the p_T of tracks within a cone of $\Delta R=0.2$ must be less than 12% the p_T of the muon. These trigger chains have thresholds that are maximally efficient for leptons passing offlines selections of $p_T > 25$ GeV.

Chapter 5

Object reconstruction

The analysis relies on the selection of electrons, muons, jets and b -tagged jets. This chapter reviews the reconstruction, definition, efficiencies and calibration of these objects in ATLAS.

5.1 Muons

Muons are reconstructed by combining tracks found in the muon spectrometer and inner detector. Track segments are found in each layer of the detector then combined, taking into account energy loss while crossing the calorimeters. Tracks in the ID are required to pass minimum hit requirements in the Pixel, SCT, and TRT. Muons can be reconstructed using only the MS, but in this analysis uses *combined* muons, reconstructed in both the MS and ID, to ensure high purity.

The muon reconstruction efficiency can be measured using the *tag-and-probe* method. The ID reconstruction efficiency is determined from events reconstructed with one combined muon, the *tag*, and a second muon only required to have an MS track, the *probe*. The ID reconstruction efficiency is given by the fraction of events where the MS track probe also has a track in the ID. The same method can be used to determine the efficiency of the MS reconstruction as matching. This time, the ID segments are used as the probe and the MS+matching efficiency is given by the fraction of ID segments with a matching MS segment. The overall muon reconstruction efficiency is given by the product of these two efficiencies. To obtain the scale factors (SF), the muon reconstruction efficiency in data and MC is compared: $SF = \epsilon_{data}/\epsilon_{MC}$. These scale factors are applied to the simulation to ensure that muons are reconstructed with the same efficiency in MC as in data. For muons, the SFs are calculated in bins of p_T and η for $Z \rightarrow \mu\mu$ and $J/\Psi \rightarrow \mu\mu$ events [?].

The muon momentum scale and resolution of the MC must also be corrected to match data. Differences can come from mis-modeling of the detector geometry, magnetic field, or energy loss in the calorimeter. Scale factors are determined by comparing the shape of the energy distribution in $Z \rightarrow \mu\mu$ and $J/\Psi \rightarrow \mu\mu$ events. For 2012, the corrections were less than 0.1% [?].

Finally, the efficiency of the muon trigger is also estimated via the tag-and-probe method. In this analysis, the logical OR of two triggers is used to identify muons: a 24 GeV trigger with a loose track-based isolation requirement (the sum of the p_T of tracks within a cone of $\Delta R=0.2$ must be less than 12% the p_T of the muon) and a 36 GeV trigger without an isolation requirement. For $p_T < 100$ GeV, $Z \rightarrow \mu\mu$ events are used to estimate the trigger efficiency, while $W+jets$ is used for p_T above this threshold. The muon trigger efficiency in the barrel region is derived from $Z \rightarrow \mu\mu$ events is shown in Figure ??

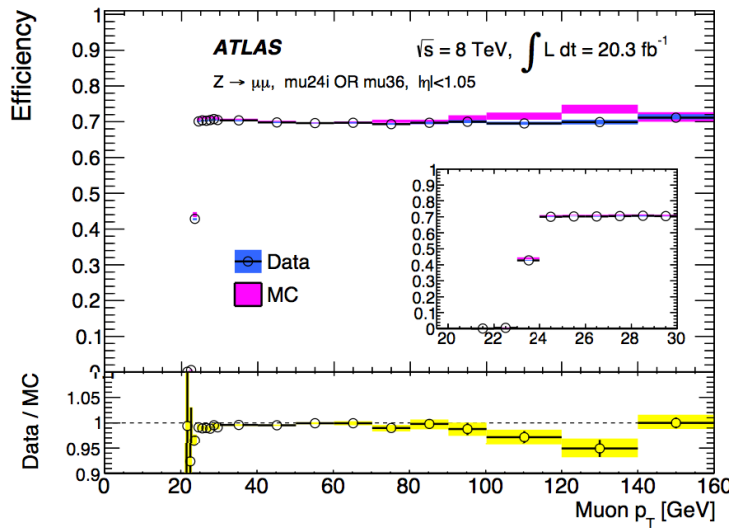


Figure 5.1: Reconstruction and identification efficiency [?].

5.2 Electrons

The reconstruction of electrons uses information from both the EM calorimeters and tracks in the ID. First, clusters of energy are found using the sliding-window algorithm described in Chapter 4.5.3. Then, tracks reconstructed in the ID are extended into the calorimeter. Tracks and clusters are considered a match if the center of the cluster and the track are within $\Delta\eta < 0.05$ and $\Delta\phi < 0.1$. Clusters that don't match to a single track are considered as candidate photons.

Quality requirements divide electron candidates into three categories: loose, medium and tight. In this analysis, electrons are required to match the tight requirements, such as ID hit requirements, shower shape, track quality and tighter criteria for matching tracks and clusters. The total reconstruction and identification efficiency for these tight electrons is shown in Figure 5.2. As with muon reconstruction, tag-and-probe methods determine the electron scale factors using $Z \rightarrow ee$.

The electron energy scale of the MC must be corrected to match data. First, the MC simulation of electron response is used as a initial calibration of the electron energy. Then,

the absolute energy scale and resolution are determined by comparing $Z \rightarrow ee$ events in data and MC. This calibration is then checked against $J/\Psi \rightarrow ee$ events.

In this analysis, the logical OR of two triggers is used to identify electrons: a 24 GeV trigger with a loose track-based isolation requirement and a 60 GeV trigger without an isolation requirement. The isolation requirement specifies that the sum of the p_T of tracks within a cone of $\Delta R=0.2$ must be less than 10% the p_T of the electron. The trigger efficiency is evaluated with a tag-and-probe of $Z \rightarrow ee$ events, using the tight electron matched to a trigger with a lower threshold as a tag and an electron with opposite charge as a probe. This efficiency is shown in Figure ??.

Their efficiency is measured using tag-and-probe in $Z \rightarrow ee$ events, where the tag is a tight electron matched to a trigger with a lower threshold and the probe is an oppositely charged electron such that the ee system has invariant mass within the Z mass window of 80-100 GeV. The measured efficiency is shown in Figure 5.3.

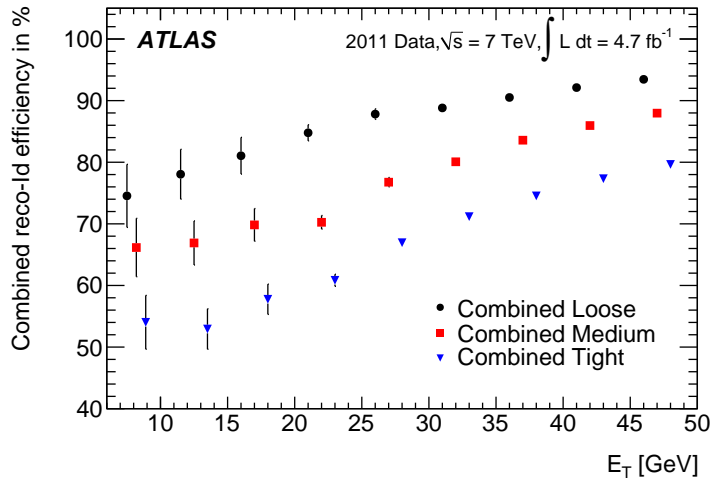


Figure 5.2: Reconstruction and identification efficiency [?].

5.3 Jets

Jet reconstruction begins with the formation of *topo-clusters* from energy deposits in the EM and hadronic calorimeter cells as described in Chapter 4.5.3. Once the clusters have been built, they are used as input to the the anti- k_t algorithm [?, ?, ?] with radius parameter $R = 0.4$. The final 4-momentum of the jet is defined as the sum of the 4-momenta of its constituent topo-clusters.

At this stage, the jet reconstruction efficiency and its uncertainty can be measured in data using the fraction track-jets matched to calorimeter jets. The efficiency can also be calculated using a tag-and-probe method in dijet events. The reconstruction efficiency is

found to be very small: about 0.0002% for jets with $p_T < 30$ GeV and negligible for jets with higher p_T .

The jets are then corrected for the effects of pileup using the jet area method. This method corrects the p_T of the jet by subtracting $\rho \times A$. The quantity ρ is defined as the energy density in the event calculated from all calibrated topo-clusters within $|\eta| \leq 2$, and the quantity A is defined as the catchment area of the jet. This correction depends both on the characteristics of the jet and the pileup in the event. Then a residual correction dependent on the instantaneous luminosity and number of reconstructed primary vertices in the event. This correction is primarily relevant in the forward region and is derived from simulation.

Finally, the jets are calibrated according to both their energy and η [?]. The jet direction is corrected so that the jet originates from the primary vertex. Then the energy scale of the jet (JES) correction is applied, which has both an MC-based and *in situ* component. The energy- and η -dependent MC-based JES scheme is derived from the ratio of the energy of a detector level jet to the matching truth level jet (jets formed using the same anti- k_t algorithm from simulated hadrons). The *in situ* correction uses data events where a jet recoils against a Z or a photon, which can be more precisely measured by the detector. However, this method can only be used for jets with $p_T < 800$ GeV. Jets with $p_T < 800$ GeV are calibrated with events where a high p_T jet recoils against a several lower p_T jets already calibrated by the Z or photon events. The final JES and uncertainty comes from a combination of such measurements. Figure 5.4 shows the JES uncertainty for jets in the central η region. The jet energy resolution (JER) is studied separately via a similar process with dijet events, and the resolution in data and simulation is found to be comparable.

5.4 b -tagged Jets

At the LHC, jets that contain b -quarks (called b -jets or b -tagged jets) can be distinguished from jets which only contain light quarks[?, ?]. The long lifetime of B -hadrons is exploited to make this distinction. Because a B -hadron will travel a relatively long path through the detector before decaying, a *secondary* vertex for this decay can be reconstructed and used to identify jets that contain a b -quark. The production of a top quark pair produces at least two b -jets (which are otherwise rare), so identifying b -jets leads to significant background reduction.

At the ATLAS detector, several algorithms are used in conjunction to identify b -jets:

IP3D is an impact parameter based algorithm that uses the tracks associated with the jet.

First, tracks must pass quality cuts on the number of hits in the ID. Then, tracks are required to have $|d_0| < 1$ mm and $z_0 < 1.5$ mm in order to reject tracks from the decays of long-lived mesons, such as kaons, and photon conversion. These tracks are then associated to the jet with a jet p_T dependent ΔR . Then, the algorithm uses the impact parameters' significance, $d_0/\sigma(d_0)$ and $z_0/\sigma(z_0)$, to produce the likelihood for tracks to originate from a b -jet. The likelihood distribution is produced from simulation.

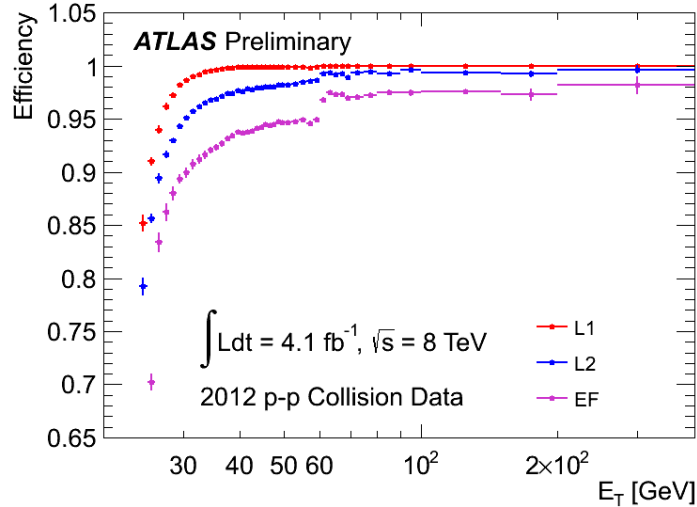


Figure 5.3: Combined efficiency of the 24 GeV and 60 GeV electron triggers. [?].

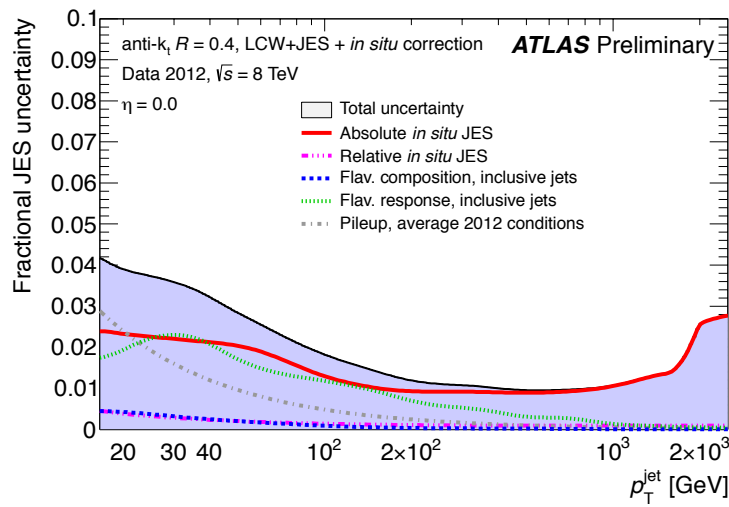


Figure 5.4: The relative Jet Energy Scale (JES) uncertainty for jets in the central region [?].

SV1 is an algorithm based on the secondary vertex. The tracks associated with the jet are required to pass quality cuts similar to IP3D. Next, all possible two-track vertices are considered. Vertices with masses compatible with long-lived particles like kaons or Λ have both tracks removed from the list of associated tracks. Then, all remaining two-track vertices are combined into a single vertex and the track with the worst fit is removed. This procedure is repeated until the overall χ^2 of the track errors to the vertex passes a quality threshold. Finally, a likelihood ratio technique is used to assign a b -tagging weight, using variables such as the secondary vertex mass, the number of two-track vertices, and the angle between the vertices and jet axis.

JetFitterCombNN uses the same tracks as IP3D. The algorithm attempts to find an axis and decay position of the B -hadron, including the possibility of an extra vertex due to a D -decay. A Kalman filter is used to start with the axis from the PV to the jet axis and update with addition of each track in the decay chain. The best combination of two vertices that fits the tracks is found. Then the decay length significance ($d_0/\sigma(d_0)$), the invariant mass of the tracks and the energy fraction of the tracks are combined into a neural network. The output of the neural network gives the likelihood that the jet is a light-, c -, or b -jet.

The results from three algorithms, IP3D, SV1 and JetFitterCombNN, are combined into a single discriminant using a neural network with the MV1 b -tagger. The efficiency of these algorithms in rejecting light-jets and c -jets is shown in Figure 5.5.

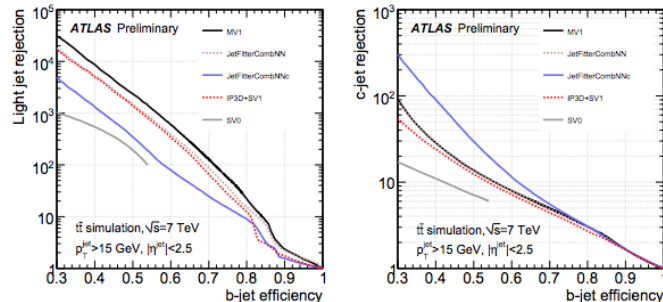


Figure 5.5: Light-jet rejection (left) and c -jet rejection (right) as a function of the b -tag efficiency for the b -tagging algorithms discussed based on simulated $t\bar{t}$ events. [?].

Chapter 6

Event selection

The following section describes the procedure used to select the events used for analysis. First, the data and simulation samples to be used are defined. Then, the fiducial definition of the physics objects used to select the events is given. Then, the criteria for selecting events is discussed. Finally, the event yields and reconstructed distributions are reviewed.

6.1 Data samples

Data and Monte Carlo samples are used in the common D3PD format (`NTUP_COMMON`), using the `p1562` processing tag. The D3PDs are processed using software based on AnalysisTop-1.8.0 [?].

6.1.1 Collision data

The analysis is performed on the complete 2012 $pp \sqrt{s} = 8$ TeV LHC collision dataset. Events are required to fulfill standard data quality requirements corresponding to the physics ‘All-Good’ good run list (GRL) [?], which ensures that all detector components are functioning. Events are required to pass a single electron or single muon trigger chain, with thresholds that are maximally efficient for leptons passing offline selections of $p_T > 25$ GeV. For electrons, the OR of the `EF_24vh_medium1` and `EF_e60_medium1` trigger chains is used. For muons, the OR of `EF_mu24i_tight` and `EF_mu36_tight` is used. In each case, the higher threshold trigger has no isolation requirement, and adds to the acceptance of the lower threshold trigger at higher lepton p_T .

Events are selected from both Egamma and Muons data streams. To avoid double counting of $e\mu$ events appearing in both streams, events passing electron triggers are only accepted from the Egamma stream, *i.e.* the Muons stream is only used for events selected only by muon triggers. Luminosity blocks where only one stream is seen in the final analysis are vetoed, to avoid biases from losing events from either stream in the upstream reconstruction

and data processing. After all these selections, the final analyzed data samples correspond to an integrated luminosity of 20.3 fb^{-1} with an uncertainty of 2.8%.

6.1.2 Simulated Samples

Simulated Monte Carlo event samples are used in this analysis to evaluate the efficiency and uncertainty of signal and background. Both uncorrected and corrected data distributions are also compared to simulated samples to distinguish between physics models. Standard ATLAS top group MC12 samples are used. [?] The corresponding dataset (DS) identification numbers are given in Tables 6.1, 6.2, and 6.3 and a complete list of dataset names is provided in Appendix ??.

Samples are processed either through the full ATLAS Geant4[?] based detector simulation or through the AtlFast2[?] fast simulation. All samples include additional overlaid minimum bias events generated with Pythia8 [?] to simulate pileup background. The simulated samples are reweighted to reproduce the same distributions of μ , the average number of interactions per bunch crossing, as the data. The samples are also reweighted with scale factors to reproduce the electron and muon reconstruction and trigger efficiencies, and the width of the primary vertex distribution in z , as measured in the data. Finally, scale factors are applied to account for b -tagging efficiencies. In all cases, the scale factors are those specified in AnalysisTop-1.8.0.

All Monte Carlo samples are normalized according to the best available theoretical cross-section and K -factor calculations, as tabulated in the TopDataPreparation package, tag 00-06-48.

6.1.2.1 $t\bar{t}$ samples

The baseline $t\bar{t}$ samples are produced using Powheg [?, ?, ?, ?] interfaced to Pythia6 [?] with the Perugia 2011C tune [?], CT10 parton density functions (PDFs) [?], the hdamp parameter set to ∞ and fast simulation (DS 117050). This same MC tune has been processed using full simulation and the results of the two samples have been compared. Powheg+Pythia6 is the baseline suggested by the TopReconstruction twiki page as the default $t\bar{t}$ simulation [?]. The atlfast2 sample with the hdamp parameter set to ∞ is chosen as the baseline because it has significantly higher statistics (~ 40 times data) than either the FS or $\text{hdamp}=m_t$ samples (~ 20 times data). Systematic uncertainties associated with the difference in the response matrices obtained from FS and atlfast are assessed in Section ??.

Alternative $t\bar{t}$ simulation samples are also studied. At next-to-leading-order, these include Powheg plus Pythia6 with the hdamp parameter set to m_t (DS 110404); Powheg plus Pythia8 with the hdamp parameter set to m_t and the A14 tune (DS117046) ; MC@NLO [?, ?] interfaced to Herwig [?, ?, ?] with Jimmy [?] for the underlying event modeling and with the ATLAS AUET2 [?] tune and CT10 PDFs (DS 105200); and Powheg plus Herwig (DS 105860). Alternate multi-leg leading order samples include MadGraph [?] interfaced to Pythia6 [?] with the Perugia 2011C tune [?], and CT10 parton density functions (PDFs) [?]

(DS 110872); Alpgen [?] interfaced to Herwig and Jimmy, with the CTEQ6L1 PDFs [?] (DS 105890–2, 117897–9, 116108 and 116109); and Alpgen interfaced to Pythia6 (DS 117113–8). To study the effects of initial and final state radiation (ISR/FSR), several samples with different radiation parameters were used.

The Powheg and MC@NLO samples include all $t\bar{t}$ final states except fully-hadronic, where both W bosons decay to $q\bar{q}$ giving a negligible probability to pass the event selection. The MadGraph sample only included dileptonic final states, where both W bosons decay to leptons. Most of these MC samples contain more than ten times the data statistics.

6.1.2.2 Single top samples

Only the Wt channel of single top production contributes significantly to $e\mu + 2$ b -jets events. Single top production is modeled using Powheg+Pythia with the CT10 PDFs and the Perugia P2011C tune, using the ‘diagram removal’ [?] generation scheme (DS 110140). Alternative physics models include the Powheg+Pythia sample with ‘diagram subtraction’ [?] (DS 110142) and MC@NLO+Herwig (DS 108346).

6.1.2.3 Background samples

Z +jets events with $Z \rightarrow \ell^-\ell^+$ and diboson production (WW , WZ and ZZ) where both bosons decay leptonically can contribute to background. Z +jets background is modeled using Alpgen [?] with CTEQ6L1 PDFs, interfaced to Pythia6 with the Perugia P2011C tune, including both samples with 0–5 additional light partons (DS 147105–10, 147113–8, 147121–6), $c\bar{c}$ plus an additional 0–3 partons (DS 200432–5, 200440–3, 200448–51), and $b\bar{b}$ plus 0–3 partons (DS 200332–5, 200340–3, 200348–51). The heavy flavor overlap procedure (HFOR) [?] is used to avoid double counting of configurations where the $c\bar{c}$ or $b\bar{b}$ pair could be produced from either the matrix element or parton shower. The simulated Z +jets events are scaled by the ratios of $Z \rightarrow ee+2$ b -jets or $Z \rightarrow \mu\mu+2$ b -jets measured in simulation and data, to account for the mismodeling of heavy-flavor jets produced with Z bosons. Ref. [?] computes this scale factor to be 1.13 ± 0.08 .

Diboson production is simulated using Alpgen+Herwig with up to three additional partons (DS 107100–11).

6.1.3 Pileup jet samples

Samples using pileup overlay simulation in $t\bar{t}$ events are used to study background to the extra jet distributions. The only sample with sufficient statistics (DS 117050) uses Powheg+Pythia with the baseline tune. The sample was processed using tag d708 which is affected by a simulation problem in the tile cell energy. An additional sample has been requested, but production is delayed by problems with ProdSys2.¹

¹JIRA entry ATLMCPROD-821

Generator	Dataset	Sim	FS	Tune	Comment
Powheg+Pythia hdamp= ∞	117050	fast	nFH	P2011C	baseline
Powheg+Pythia hdamp= m_t	110404	fast	nFH	P2011C	alt. physics
MC@NLO+Herwig	105200	fast	nFH	P2011C	alt. physics
Powheg+Herwig	105860	fast	nFH	AUET2	alt. shower
Powheg+Pythia8	117046	fast	nFH	A14	alt. physics
MadGraph+Pythia	110872	fast	$\ell\ell$	P2011C	alt. physics
Alpgen+Pythia	201020-4	fast	nFH	P2012	alt. physics
Alpgen+Herwig	164440-3,	full	nFH	P2012	alt. physics
Alpgen+Herwig	116108	full	nFH	P2012	alt. physics
Alpgen+Herwig	116109	full	nFH	P2012	alt. physics
AcerMC+Pythia	117209	fast	nFH	MPS AUET2	more radiation
AcerMC+Pythia	117210	fast	nFH	LPS AUET2	less radiation
Alpgen+Pythia	201030-4	fast	nFH	P2012	ktfac=0.5, more radiation tune
Alpgen+Pythia	201040-4	fast	nFH	P2012	ktfac=2, less radiation tune
MadGraph+Pythia	110878	fast	$\ell\ell$	P2011C	more radiation tune
MadGraph+Pythia	110875	fast	$\ell\ell$	P2011C	less radiation tune

Table 6.1: $t\bar{t}$ samples used in this analysis. The sample name, dataset ID, simulation type, final state simulated (non-fully hadronic, nFH, or dilepton, $\ell\ell$) and tune is given. The Alpgen samples consist of several samples with different parton multiplicities and sometimes dedicated heavy flavor samples.

Generator	Process	Sim	FS	Tune	Comment
Alpgen+Herwig	Diboson	full	$\ell\ell$	AUET2	
Alpgen+Pythia	Z+jets	full	$\ell\ell$	P2011C	On-the-fly

Table 6.2: Z+jets and diboson background samples used in this analysis. The sample name, process, simulation type, process simulated, final state simulated (non-fully hadronic, nFH, or dilepton, $\ell\ell$) and tune is given. The Alpgen samples consist of several samples with different parton multiplicities and sometimes dedicated heavy flavor samples. Dataset IDs are listed in Appendix ??.

Generator	Dataset	Sim	Tune	Comment
Powheg+Pythia	110140	fast	P2011C	baseline diagram removal
Powheg+Pythia	110142	full	P2011C	alt. diagram subtraction
MC@NLO+Herwig	108346	full	AUET2	alt. physics

Table 6.3: Single top Wt -channel samples used in this analysis. The sample name, dataset ID, simulation type, and tune is given. All samples are simulated with the inclusive final state in the Wt channel.

Because of limitations with the available overlay samples, a data driven estimate of the pileup is used for the baseline analysis. This estimate uses data from the `data12_8TeV.physics_ZeroBiasOverlay` which are events taken from data to estimate pileup. These data are available in `NTUP_COMMON` format. This sample is studied as an alternative to the standard minimum bias overlay in the other samples.

6.2 Object definitions

The object and event selection follows the generic ATLAS top working group recommendations for 2012 [?], with two exceptions. The first change is a loosening of the electron isolation criteria, which is possible due to the low background $e\mu$ final state. This loosened requirement is also used in Ref. [?]. The second change is to relax the η requirement on jets to $|\eta| < 4.5$.

6.2.1 Reconstructed objects

The analysis relies on the selection of electrons, muons and jets, and the tagging of jets as b -jets. With the exceptions specified above, these correspond to standard TopRootCore defaults.

Muons: Combined muons (reconstructed in both the muon spectrometer and inner detector) are selected with the MuID algorithm, and required to satisfy $p_T > 25 \text{ GeV}$ and $|\eta| < 2.5$. Following the 2012 recommendations from the MuonCP group, muons must have

- at least one pixel hit
- at least 5 SCT hits
- fewer than 3 holes in pixel and SCT layers combined
- In the region $0.1 < |\eta| < 1.9$: $n_{TRTHits} + n_{TRTOutliers} > 5$ and $\frac{n_{TRTHits}}{n_{TRTHits} + n_{TRTOutliers}} < 0.9$

The impact parameter in the longitudinal direction with respect to the primary vertex is required to satisfy $z_0 < 2 \text{ mm}$. To reduce the background from muons from heavy flavor decays inside jets, muons are required to be separated by $\Delta R > 0.4$ from the nearest jet. Muons are required to satisfy mini-isolation requirement $I_{\text{mini}}^\ell < 0.05$, where the mini-isolation variable is the ratio of the sum of p_T of tracks in a variable-sized cone of radius $\Delta R = 10 \text{ GeV}/p_T(\mu)$ to the p_T of the muon $p_T(\mu)$ [?].

Electrons: Electrons are selected using the offline `tight++` identification within the fiducial region $p_T > 25 \text{ GeV}$ and $|\eta| < 2.47$, excluding the calorimeter transition region $1.37 < |\eta| < 1.52$. The impact parameter in the longitudinal direction with respect to the primary vertex is required to satisfy $z_0 < 2 \text{ mm}$. In addition to the calorimeter isolation

requirements implicit in `tight++`, the calorimeter energy in a cone of radius $\Delta R < 0.2$ around the electron (excluding the deposit from the electron itself) is required to satisfy $\text{ETCone20} < 6 \text{ GeV}$, and the sum of p_T of tracks in a cone of radius $\Delta R < 0.3$ (excluding the electron track) is required to satisfy $\text{pTCone30} < 6 \text{ GeV}$. Using the EGamma group EisoTool2012 [?], further kinematic-dependent cuts are applied to these two isolation variables, corresponding to a 98 % efficiency on true prompt electrons. To prevent double-counting of electron energy deposits as jets, jets within $\Delta R < 0.2$ of a reconstructed electron are removed. If the nearest jet surviving the above cut is within $\Delta R < 0.4$ of the electron, the electron is discarded, to ensure it is cleanly separated from nearby jet activity. Electrons sharing a track with a muon are excluded by removing electrons with a muon within $\Delta\phi < 0.005$ and $\Delta\theta < 0.005$.

Jets: Jets are reconstructed using the anti- k_t algorithm [?] with radius parameter $R = 0.4$, starting from topological clusters. These are calibrated using the local cluster weighting (LCW) method, and corrected for the effects of pileup using the jet area method and a residual correction dependent on the instantaneous luminosity and number of reconstructed primary vertices in the event. Jets are calibrated using an energy- and η -dependent simulation-based calibration scheme, with in-situ corrections based on data [?]. Jets are accepted within the fiducial region $p_T > 25 \text{ GeV}$ and $|\eta| < 4.5$. To reduce the contribution from jets associated with pileup jets with $p_T < 50 \text{ GeV}$ are required to satisfy $|\text{JVF}| > 0.5$, where JVF is the ratio of the sum of the p_T of tracks associated to the jet which are also associated to the primary vertex, to the sum of p_T of all tracks associated to the jet. Jets with no associated tracks or with $|\eta| > 2.4$ at the edge of the tracker acceptance are assigned $\text{JVF} = -1$ by convention and thus always accepted. Reconstructed jets within $\Delta R < 0.2$ of a selected electron are removed.

b -tagging: Jets within the central region ($|\eta| < 2.5$) are b -tagged using the MV1 algorithm [?, ?], which combines the outputs of the IP3D, SV1 and JetFitterCombNN algorithms into a multivariate discriminant w with values between zero and one. Light-quark and gluon jets tend to have values close to zero, and b -flavored jets close to one, with charm jets somewhere in between. Jets are defined as being b -tagged if the MV1 weight w is larger than a cut value 0.7892, which corresponds to the b -tagging working point having approximately 70% b -tagging efficiency for b -jets in $t\bar{t}$ events, although the exact efficiency varies significantly with p_T . The b -tagging calibration used is the default in TopRootCore, which is based on the system8 muon and jet calibration method [?].

Events reconstructed with exactly one e and μ with opposite sign and at least 2- b jets as defined above pass the reconstruction-level fiducial selection. In the case of Monte Carlo, selected events are reweighted to reproduce the same distributions of μ , the average number of interactions per bunch crossing, as in the data. The samples are also reweighted with scale factors to reproduce the electron and muon reconstruction and trigger efficiencies, and the width of the primary vertex distribution in z , as measured in the data. Finally, scale factors are applied to account for b -tagging efficiencies.

6.2.2 Truth objects

Truth objects are processed using the software package TopFiducial-00-00-09 in AnalysisTop-1.8.0. Cuts applied to truth objects attempt to replicate the above fiducial selections for the reconstructed objects.

Leptons: Stable electrons and muons are required not to come from a hadron in the Monte Carlo truth particle record, either directly or through a tau decay. This ensures that the lepton is from an electroweak decay without requiring a direct W -boson match. The four momenta of the bare leptons are then ‘dressed’ by adding the four momenta of all stable photons within $\Delta R=0.1$ with status code 1 and not originating from Geant4. The dressed leptons are required to have $p_T > 25$ GeV and $|\eta| < 2.5$.

Jets: Truth jets are clustered using the anti- k_t algorithm [?] with radius parameter $R = 0.4$, starting from all stable particles, except for selected leptons (e, μ, ν) and the photons used to dress the leptons. Truth jets are required to have $p_T > 10$ GeV, $|\eta| < 4.5$. Though only jets with $p_T > 25$ GeV are considered in the final result, lowering the p_T requirement for truth jets allows matching across the fiducial boundary. This is discussed in more detail in Section ??.

b -tagging: B hadrons with $p_T > 5$ GeV are associated with jets through ghost matching [?]. Truth b -tagged jets have $p_T > 25$ GeV, $|\eta| < 2.5$ and at least one ghost associated B -hadron with $p_T^B > 5$ GeV.

Overlap removal: Truth objects are subject to the same overlap removal criteria as reconstructed objects, after dressing and jet reclustering. The closest jet within $\Delta R < 0.2$ of an electron is excluded from consideration. After such jets are removed, muons and electrons with $\Delta R < 0.4$ of a jet are excluded. Electrons overlapping with muons are removed if $\Delta\phi_{e\mu} < 0.005$ and $\Delta\theta_{e\mu} < 0.005$.

Events with exactly one e and μ with opposite sign and at least 2- b jets as defined above pass the fiducial truth selection.

6.2.3 Truth matching

Following TopFiducial standard criteria, a geometric ΔR algorithm matches reconstructed objects to truth objects satisfying the fiducial requirements above. These definitions are relevant for background unmatched extra jets, as well as various truth studies.

Leptons: Each truth e (μ) is matched to the closest reconstructed e (μ) within $\Delta R < 0.02$.

Jets: Truth jets are geometrically matched to the closest reconstructed jet within $\Delta R_{\text{recojet,truthjet}} < 0.4$. If a reconstructed jet is not matched to a truth jet, it is assumed to be either from pileup or matching inefficiency and is treated as background as discussed in Section 7.2.

In selecting $e\mu+2 b$ -jet events, b -jets are matched to truth jets before extra jets. Thus, if both an extra jet and a b -jet satisfy $\Delta R_{\text{recojet},\text{truthjet}} < 0.4$, the b -jet is matched to the truth jet and the extra jet is unmatched. If two b -jets or two extra jets are reconstructed within $\Delta R_{\text{recojet},\text{truthjet}} < 0.4$ of a single truth jet, the reconstructed jet with smaller $\Delta R_{\text{recojet},\text{truthjet}}$ is matched to the truth jet and the other reconstructed jet is unmatched.

Because of limited p_T resolution, the reconstructed p_T of a jet can vary significantly from its truth p_T . The p_T threshold for truth jets is lowered to 10 GeV, so that jets reconstructed with $p_T < 25$ GeV can match truth jets that fail the fiducial p_T cut.

Parton matching: For some studies, the truth jets from top are identified via a parton matching procedure. Each jet is matched to the highest energy parton² with $p_T > 5$ GeV within $\Delta R = 0.4$. If this parton is a decay product of the top, then the jet is considered a ‘top jet.’

6.3 Event selection

The process of selecting $e\mu + 2 b$ -jets events proceeds as follows. First, events are selected from simulation and data by vetoing a small number of events failing cleaning cuts. Then events are required to have exactly one electron and one muon with opposite charges. Finally, events with at least two b -tagged jets are selected. In events with more than two b -tagged jets, the two b -jets with the highest MV1 are considered the b -jets used to select the event and the remaining b -jet(s) are considered extra jets. The selection requirements are identical to those in the 2012 $t\bar{t}$ cross-section analysis [?], with the exception of requiring *at least* two b -tagged jets instead of *exactly* two.

6.3.1 Cleaning cuts

Events are required to have at least one reconstructed primary vertex with at least five associated tracks. Events containing any jets with $p_T > 20$ GeV and positive energy that fail the ‘Bad Loose Minus’ (also known as ‘Looser’) jet quality cuts [?] are removed (‘jet cleaning’). To remove events containing cosmic rays, events with two muons passing the muon selection requirements given above, each having an impact parameter with respect to the primary vertex $d_0 > 0.5$ mm and separated in azimuthal angle ϕ by $\Delta\phi > 3.1$ rad, are vetoed.

A muon undergoing catastrophic bremsstrahlung/energy loss in the calorimeter can leave a large energy deposit, causing it to be reconstructed as both an electron and a muon, and potentially giving rise to a fake $e\mu$ event. Such background is reduced by vetoing $e\mu$ events if the electron and muon are separated by $\Delta\phi < 0.005$ and $\Delta\theta < 0.005$, where ϕ and θ are the azimuthal and polar angles of the selected leptons (muon bremsstrahlung cut).

²Quarks (u,d,s,c,b), gluons, photons and pdgId = 0 particles.

6.3.2 Event yields

The numbers of events with exactly one e and one μ before and after the b -jet requirement are given in Table 6.4. The events are selected from the 2012 $\sqrt{s} = 8$ TeV data with 20.3 fb^{-1} . Simulation predictions are categorized into contributions from $t\bar{t}$, Wt single top, $Z+jets$ and dibosons.

After the selection of $e\mu$ opposite-sign pairs, the biggest contribution (60%) is from $t\bar{t}$ events with the second largest from $Z+jets$ (21.8%). The $e\mu$ event rates agree to better than 3% with those from other ongoing 2012 top analyses as documented in TopEventChallenge[?]. The events with at least 2 b -jets are heavily dominated by $t\bar{t}$ events, with a small $\sim 3\%$ contribution from single top. $Z+jets$ and dibosons make up less than 0.1% of events passing the final selection, and are thus neglected in this analysis.

The number of selected events in simulation and data agree to within better than 3%, demonstrating that the Monte Carlo reproduces the data quite well. Table 6.5 compares the number of selected events from the baseline $t\bar{t}$ simulation to those from other $t\bar{t}$ generators. The two PowHeg+Pythia simulations and MC@NLO+Herwig all agree with each other to within 2%. The MadGraph+Pythia simulation gives about 10% more events. The reason for this difference is not well understood. The last column in Table 6.5 gives the scale factor used to normalize each $t\bar{t}$ generator to the number of events in data (including the single top contribution).

6.3.3 Reconstructed distributions

In Figures 6.1 and 6.2, the properties of reconstructed lepton and b -jets in $e\mu+2 b$ -jet events are compared in simulation and data. The negligible contributions from $Z+jets$ and dibosons are not shown. Simulation is normalized to the number of events in data using the scale factors in Table 6.5 in order to study the shape differences and remove uncertainties from the $t\bar{t}$ cross section. In Figures 6.1 and 6.2, the statistical uncertainty on the data is shown as a gray band on the ratio plot and statistical uncertainties on the simulation are shown as error bars on the ratio. Systematic uncertainties are not shown.

Figure 6.1 shows the p_T and η distributions of the leptons. Figure 6.2 shows the p_T and η distributions of the 2 b -jets used to select the events.

Overall, the b -jets and the leptons are well modeled by simulation. PowHeg+Pythia $hdamp=\infty$ agrees well, motivating its suitability as a baseline simulation.³ These observations are consistent with those in Ref. [?].

³The baseline sample is primarily chosen for high statistics

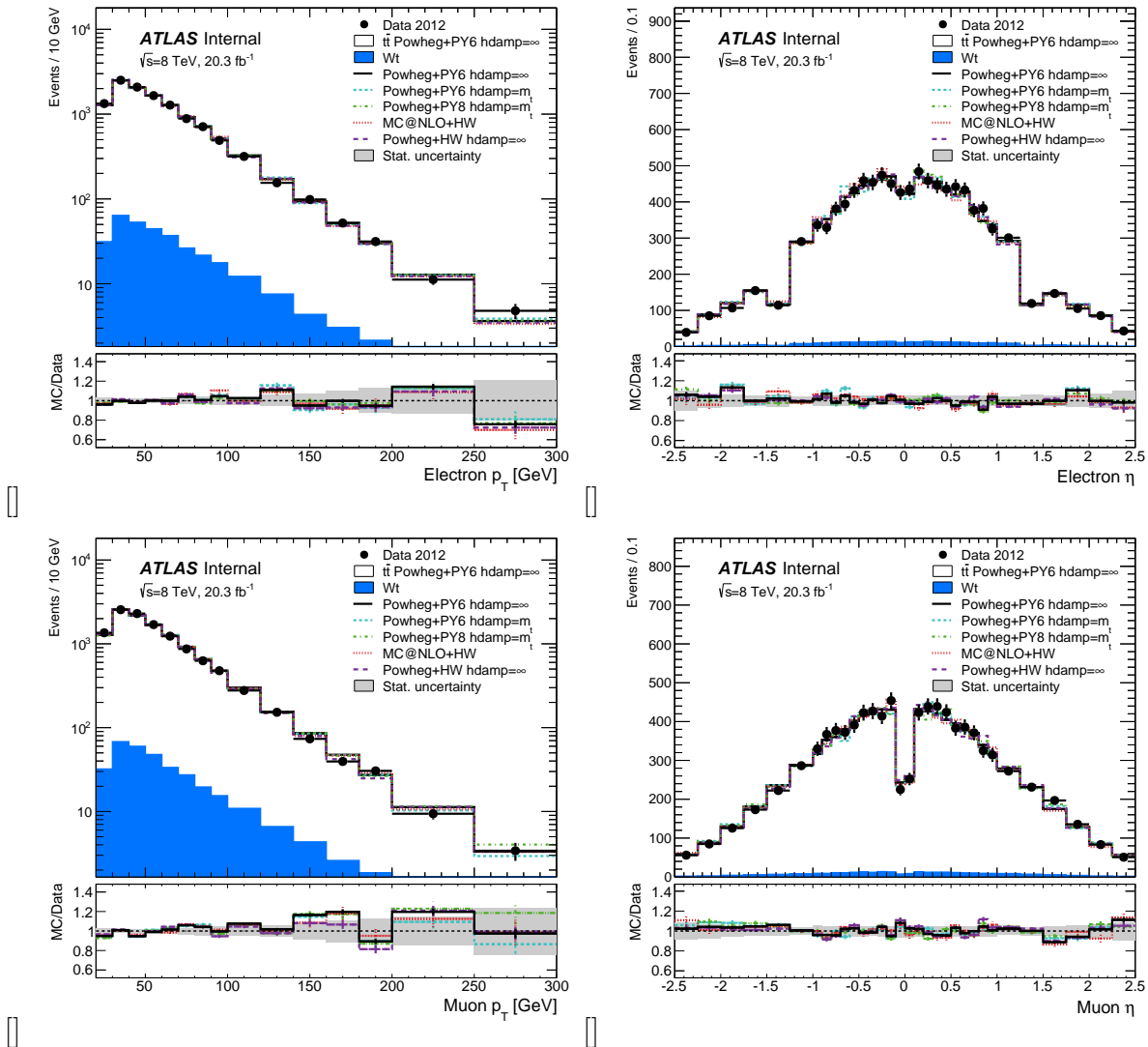


Figure 6.1: Distributions of the transverse momentum and η of the electron and muon in events with an opposite sign $e\mu$ pair and at least 2 b -jets in data and simulation. The distributions in data are compared to simulation normalized to data yields (see scale factors in Table 6.5). The ratio of different MC samples to data is shown with error bars corresponding to the MC statistical uncertainty and a shaded band corresponding to the data statistical uncertainty.

Component	$e\mu$	(%)	≥ 2 - b jets	(%)
$t\bar{t}$	40542.1	59.4	11946.5	97.1
Single top	3955.8	5.8	356.3	2.9
Z+jets	15117.4	22.1	4.5	0.0
Dibosons	8585.7	12.6	1.7	0.0
Total	68201.0	100.0	12309	100.0
Data	69575		12332	

Table 6.4: Number of events with opposite sign $e\mu$ and at least 2 b -jets in the data compared to that from Monte Carlo, broken down into contributions from $t\bar{t}$, Wt single top, Z+jets and dibosons. Only central values are shown here; systematic uncertainties are discussed in Section ??.

Generator	DS	$N_{t\bar{t}}$	$N_{\text{data}}/(N_{\text{single top}} + N_{t\bar{t}})$
PowHeg+Pythiah damp=∞ (base)	117050	11946.5	1.0024
PowHeg+PythiaP2011C hdamp= m_t	110404	12095.8	0.9904
MC@NLO+Herwig	105200	12208.3	0.9815
MadGraph+Pythia	110872	356.33	0.9194
PowHeg+Herwig	105860	11856.6	1.0097
PowHeg+Pythia8	117046	12115.6	0.9888

Table 6.5: Number of events with an opposite sign $e\mu$ and at least 2 b -jets for different $t\bar{t}$ generators. The last column gives scale factor to normalize the sum of the $t\bar{t}$ simulation and single top yields ($N_{\text{single top}} = 361.4$) to the data yield (12332).

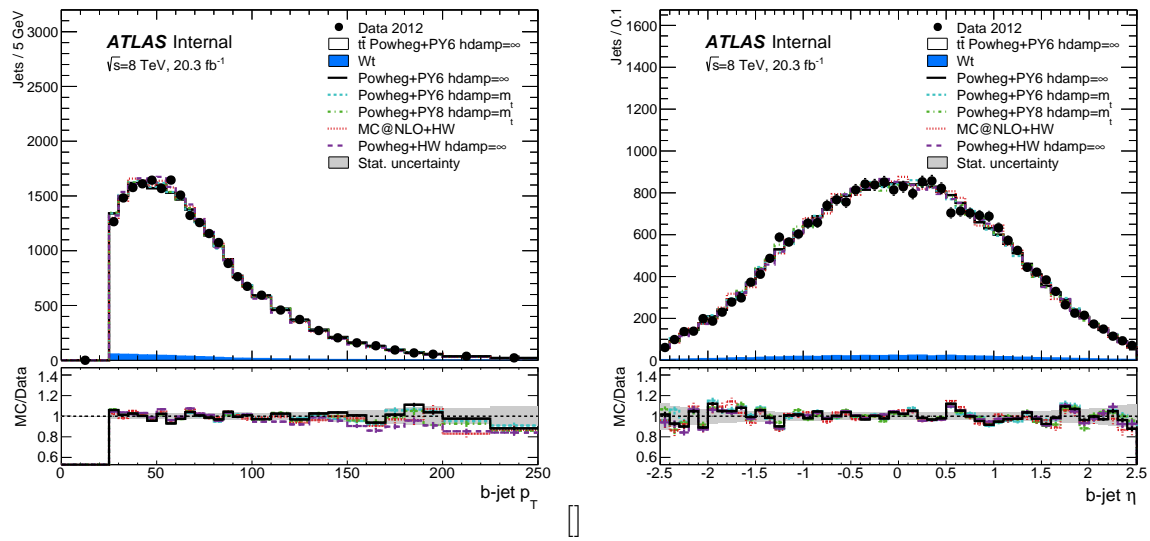


Figure 6.2: Distributions of the transverse momentum and η of the b -jets in events with an opposite sign $e\mu$ pair and at least 2 b -jets in the 2012 data. The distributions in data are compared to simulation, normalized to the same number of events as in the data (see scale factors in Table 6.5).. In events where more than two b -jets are reconstructed, the two highest p_T b -jets are selected and the remaining b -jet is classified as an extra jet (see Section ??). The ratio of different MC samples to data are shown with error bars corresponding to the MC statistical uncertainty and a shaded band corresponding to the data statistical uncertainty. Systematic uncertainties are not shown.

Chapter 7

Reconstruction of extra jets

The goal of this analysis is to study additional jets in events that pass the selection criteria described above. Jets in selected events are divided into two categories: the two b -jets used for event selection and any additional ‘extra’ jets. In simulated data, this categorization is done independently for truth jets and reconstructed jets. The b -jets are required to have $|\eta| \leq 2.5$. Extra jets are required to have $|\eta| \leq 4.5$. The final measurement of the extra jets will be corrected to the fiducial region $p_T^{jet} > 25$ GeV.

7.1 Matching criteria

As described in Section 6.2.3, a geometric algorithm matches reconstructed jets to truth jets. The b -jets are matched before the extra jets and no two reconstructed jets are allowed to match to the same truth jet. Though required to have reconstructed $p_T \geq 25$ GeV, reconstructed jets are matched to truth jets with $p_T \geq 10$ GeV. This procedure allows the unfolding to account for migration over the selection boundary.

In the $\sim 2\%$ of events with more than two reconstructed b -jets, the two jets with the highest MV1 weight are classified as the selected b -jets and the remaining jets are treated as extra jets. In the events that contain more than two reconstructed b -jets, this prescription selects b -jets that are matched to the top decay products with 74% accuracy. In contrast, choosing the two highest p_T b -jets in these same events selects b -jets from the top decay 68% of the time. In simulated events with exactly 2 reconstructed b -jets, 96% of selected b -jets descend from the top quark; the remainder are consistent with mistagged [?] non b -jets.

7.2 Background contributions to extra jets

In the baseline MC sample, approximately 4% of the events contain an *unmatched* jet (see Section 6.2.3). The RooUnfold package used to unfold the data does not properly handle p_T -dependent background subtraction. Therefore, the unfolding response matrix is constructed

using only matched jets. Unmatched jets are defined to be background and are subtracted from the data before unfolding. Unmatched jets can result from two sources:

Pileup : Jets coming from additional proton-proton collisions within the same bunch crossing.

False : Jets observed in the reconstruction that arise from detector effects or jets resulting from reconstruction pathologies such as when a single truth jet is split into two reconstructed jets or when the $\eta - \phi$ positions of the truth and reconstructed jets differ by more than the matching distance of 0.4.

The procedures used to estimate the rate of these two types of backgrounds are outlined below.

7.2.1 Pileup jets

The ATLAS simulation describes the effect of pileup on hard-scatter jets well. [?] The multiplicity of pileup jets has not been as fully validated, especially in the region $2.4 < |\eta| < 4.5$. Ideally, the pileup rate could be estimated using the ATLAS pileup overlay simulation framework. In this framework, zero bias events from data are combined with simulated hits for the hard scattering event and the digitization and reconstruction are performed on the combined sample. At present, only two $t\bar{t}$ pileup overlay samples exist. One, using MC@NLO for the hard scattering, contains only 400,000 no-all-hadronic events and is too small to use for systematic studies. The other uses the baseline Powheg+Pythia $hdamp=\infty$ configuration, but uses tag d780 which is affected by simulation problems with the tile cell energy that can affect the JES for hard scatter jets. In addition, this sample has limited statistics. Despite these problems, the pileup overlay sample provide a reasonable description of pileup jets, as documented in Appendix ??.

A higher statistics alternative to the overlay sample can be constructed using a hybrid technique. This hybrid technique takes as its input files in NTUP_COMMON format from the baseline simulation and from the ZeroBiasOverlay data stream (the same stream that is used as input to the standard overlay simulation). Unmatched jets are removed from the baseline simulation and the matched jets are combined with reconstructed jets from the zero bias data.

To properly estimate the pileup rate, the input ZeroBiasOverlay data must be luminosity-weighted to match the data. This weighting is done as follows. First, the run number and luminosity block number for all events passing the $e\mu + 2 b$ -jets data event selection is tabulated. Second, data from the ZeroBiasOverlay stream is skimmed to keep only those run and luminosity block pairs present in the selected data. Third, $t\bar{t}$ MC events are analysed. The e, μ, b -jets, and truth-matched additional jets are kept and the unmatched additional jets are deleted. For each MC event, a ZeroBiasOverlay data event is randomly selected from the skimmed data. The distribution of these ZeroBias events is forced to sample the list of run and luminosity block numbers to match the distribution for the $e\mu + 2 b$ -jets data. The

reconstructed jets in the selected ZeroBiasOverlay event are added to the $t\bar{t}$ MC event record. An overlap removal procedure removes zero bias jets that overlap hard scatter jets. If a zero bias jet overlaps a lepton, then the event is removed from the sample. This hybrid sample provides the baseline estimate of the pileup contribution to the extra jet distributions.

The dependence of the extra jet rate on the average number of interactions per bunch crossing (μ) in the signal sample is used to validate this estimate. Details of this validation are provided in Appendix ???. Figure 7.2 shows an example of this procedure for (a) central and (b) forward jets for the lowest jet p_T bin used in this analysis. The figure shows the mean number of jets in events passing the baseline selection as a function of μ and the pileup contribution estimated from the ZeroBiasOverlay stream. Before pileup subtraction, the number of jets depends on μ , with a larger dependence observed in the forward η region where the JVF cut can not be used. After subtraction of the pileup using the estimate from the ZeroBiasOverlay stream, this μ dependence is eliminated. For this p_T bin, the estimated number of pileup extra jets per event is 0.005 (0.016) in the central(forward) region. The pileup rate decreases with jet p_T and is estimated to be below 0.002 for jets with $p_T > 50$ GeV. Systematic uncertainties on this pileup estimate are discussed in Section 9.4.

7.2.2 False jets

Reconstruction pathologies are studied using simulated data. Because the simulation event record does not contain truth information for pileup, it is not straightforward to determine what fraction of the unmatched jets derive from pileup and what fraction are the result of other detector effects. The most straightforward way to study the rate of false jets would be to study them in a sample simulated without pileup, but no such $t\bar{t}$ sample exists.

The rate of false jets is estimated by studying the ΔR between extra jets. While the $\eta - \phi$ position of pileup jets is uncorrelated with the position of truth jets, false jets from reconstruction pathologies should be preferentially close to truth jets (since they are derived from particles in these truth jets). Figure 7.3 shows the distance between each reconstructed jet and the nearest additional reconstructed jet in the event ($\Delta R_{\text{reco jet}, \text{reco jet}}$) in simulation and in data for jets of rank=1-4. The data is in good agreement with the simulation. The contribution of unmatched jets at low $\Delta R_{\text{reco jet}, \text{reco jet}}$ is evident in the figure; this false jet component is needed in order to reproduce the shape observed in the data.

Figure 7.4 shows the distance between each reconstructed jet and the nearest truth jet ($\Delta R_{\text{reco jet}, \text{truth jet}}$) for jets of rank=1-4. The presence of unmatched jets with $\Delta R_{\text{reco jet}, \text{truth jet}} < 0.4$ results from the requirement that each truth jet can only be matched to a single reconstructed jet, as described in Section 6.2.3. Because the matching requires $\Delta R_{\text{reco jet}, \text{truth jet}} < 0.4$, all jets above this threshold are unmatched. The probability that a second (and hence, unmatched) jet is reconstructed with $\Delta R_{\text{reco jet}, \text{truth jet}} < 0.4$ is ~ 0.0068 . This number represents a lower bound on the false jet rate.

The false jet rate can be estimated in another way. Figure 7.5 shows the number of unmatched jets per event in the baseline simulation as a function of μ . These unmatched jets include both the pileup and false jet contributions, with pileup dominating at high μ

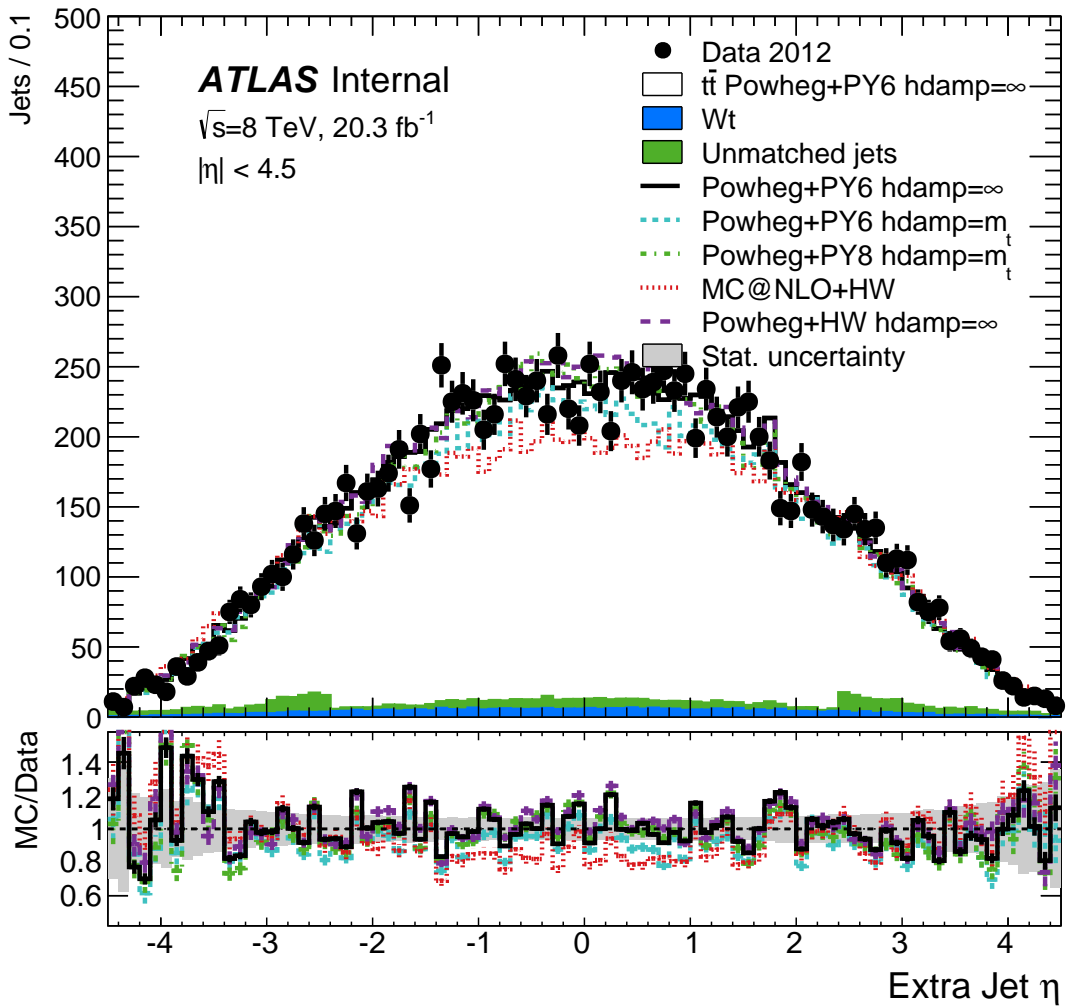


Figure 7.1: The η distribution of extra jets in simulation and data.

and false jets at low μ . The rate of false jets can be determined by fitting this distribution to a first order polynomial. The intercept of this fit predicts the false jet rate, while the slope provides the pileup rate in the simulation. The fitted intercept is 0.0075 ± 0.0014 , which is slightly higher than the estimate obtained from $\Delta R_{\text{reco jet}, \text{truth jet}}$ above, but is consistent within the statistical uncertainty on the fit. This second technique is used to obtain the baseline false jet estimate and its uncertainty.

The false jets comprise $\sim 20\%$ of the total unmatched jets and have a p_T and rank dependence similar to pileup jets. These two contributions are treated as a single background in the subtraction procedure.

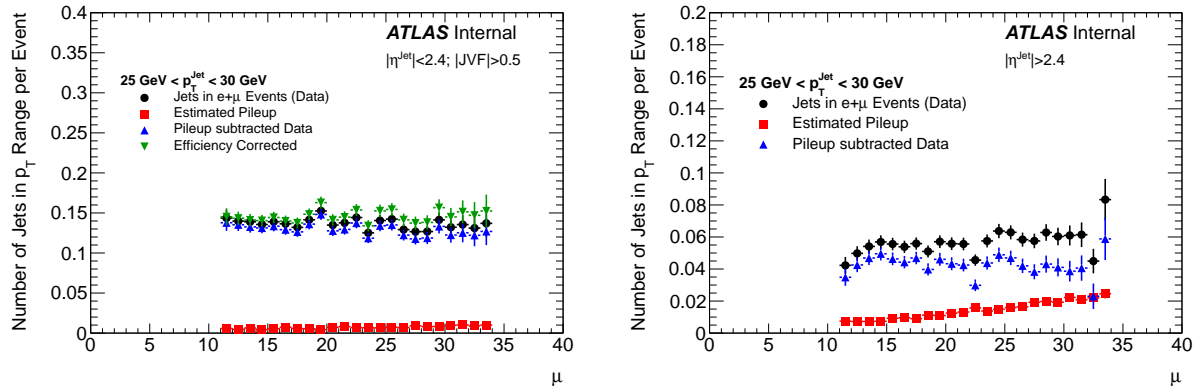


Figure 7.2: Mean number of reconstructed jets as a function of $\langle \mu \rangle$ for jets in the p_T range $25 < p_T^{\text{jet}} < 30 \text{ GeV}$ for (a) central and (b) forward jets in data events passing the $e+\mu$ selection before and after correction for pileup. Jets passing the 70% MV1 b-tagging selection are removed. The pileup rate is estimated using the ZeroBiasOverlay data stream. The blue markers show the pileup subtracted rate before correcting for the $\langle \mu \rangle$ -dependent efficiency of the JVF cut. The green points show the results after correction.

7.3 Reconstruction level distributions

Figures 7.6 and 7.7 compare the multiplicity and p_T of reconstructed extra jets in data and $t\bar{t}$ simulation, where the simulation has been normalized to the number of events in data. Statistical uncertainty on the data is shown as a gray band on the ratio plot and statistical uncertainty on the simulation is shown as error bars on the ratio. Systematic uncertainties are not shown. In data, background from pileup jets is subtracted, while in simulation, reconstructed jets are required to have a truth match. The multiplicity in the MC samples agree with that of the data, except for MC@NLO+Herwig, which consistently underestimates the number of events with 3 or more extra jets. Figure 7.7 shows the p_T distributions of each extra jet, including contributions from single top events and unmatched jets. The fact that MC@NLO+Herwig underestimates the jet multiplicity can be seen in these distributions. The jets in PowHeg+Pythia8 appear to exhibit a slightly harder spectrum than the data. All other generators agree reasonably well with the data.

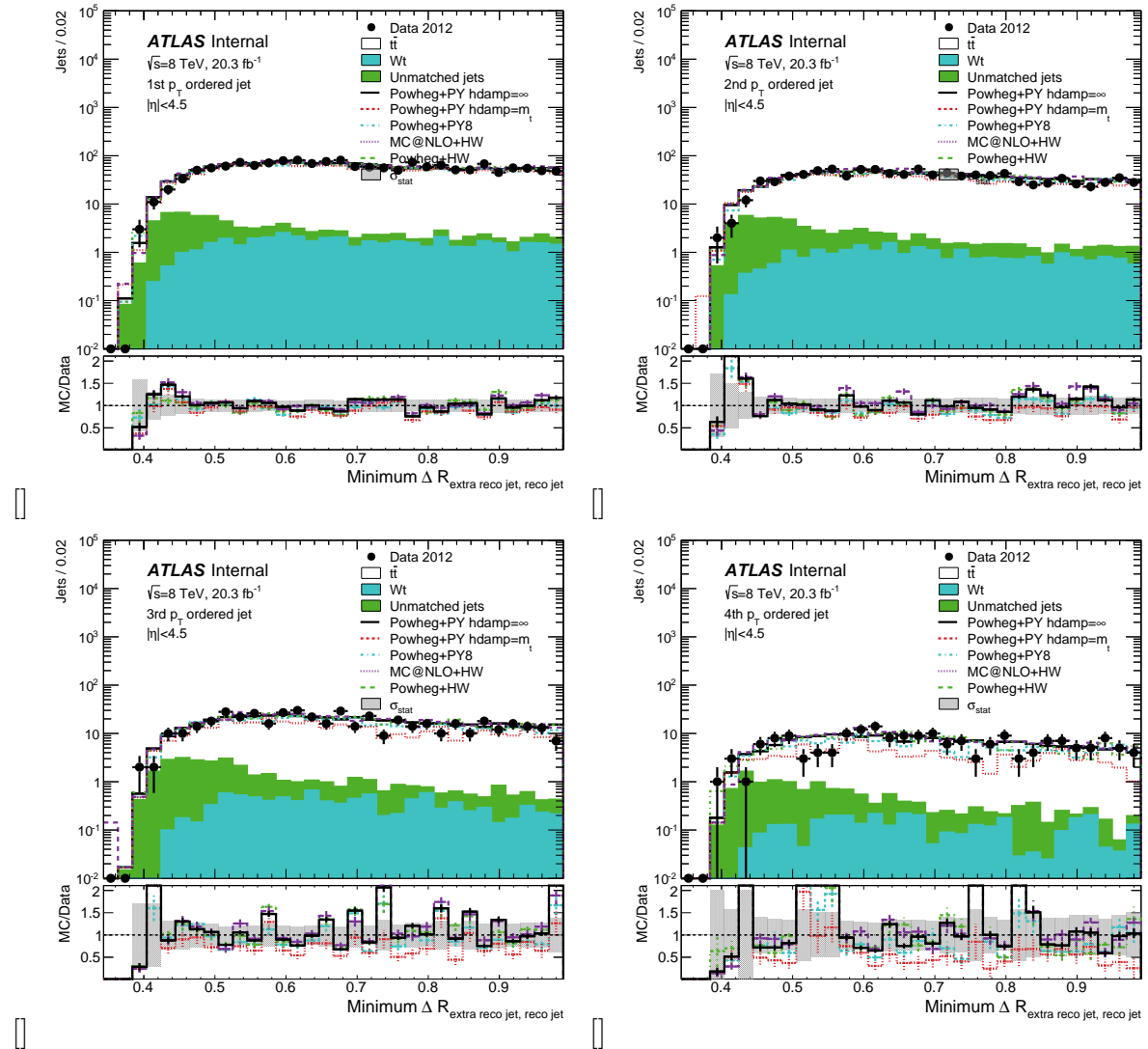


Figure 7.3: Distributions of minimum reconstructed ΔR between extra jets in simulation and data for (a) the first, (b) second, (c) third and (d) fourth extra jet.

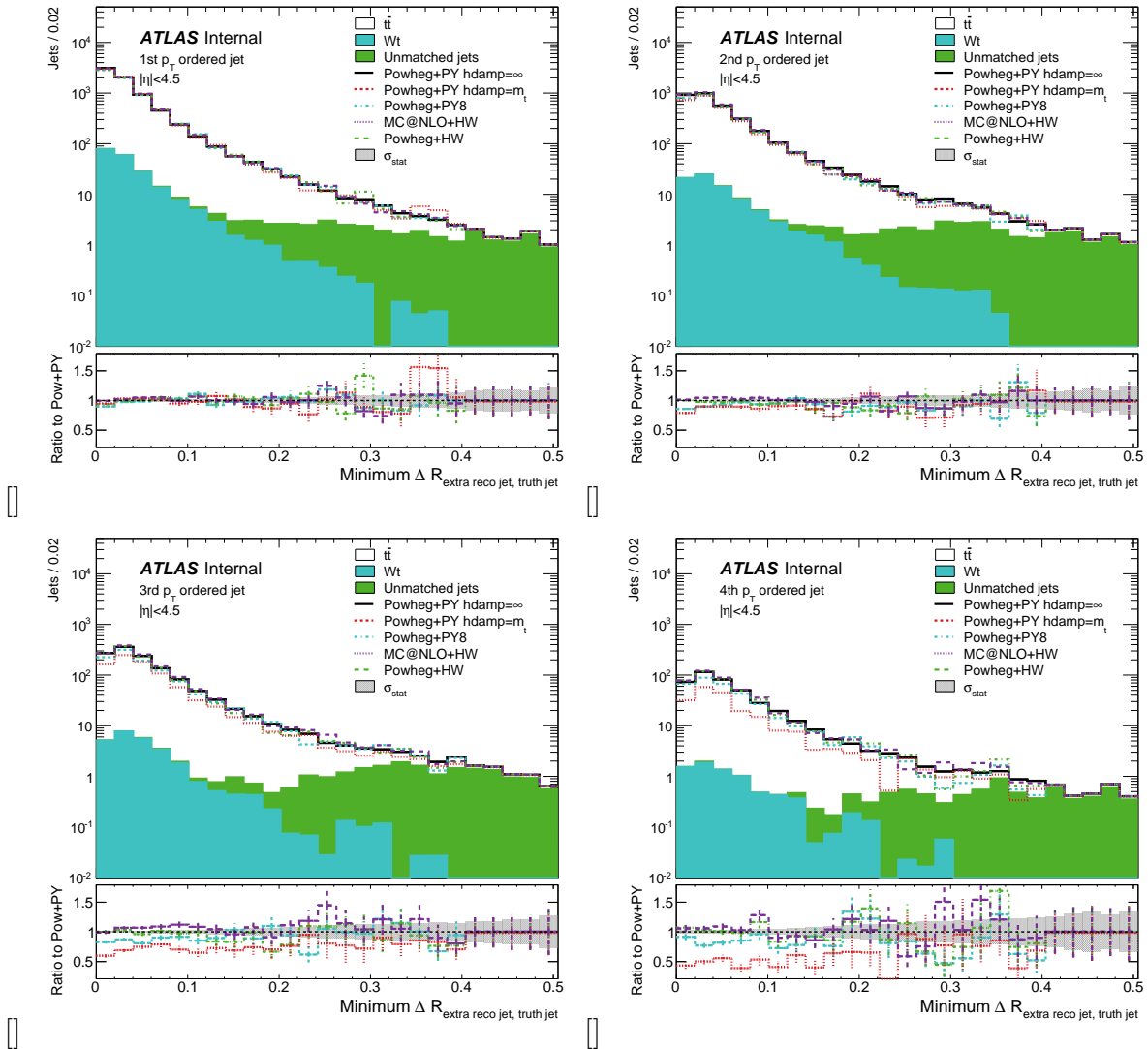


Figure 7.4: Distributions of ΔR between reconstructed extra jets and the nearest truth jet for (a) the first, (b) second, (c) third and (d) fourth extra jet.

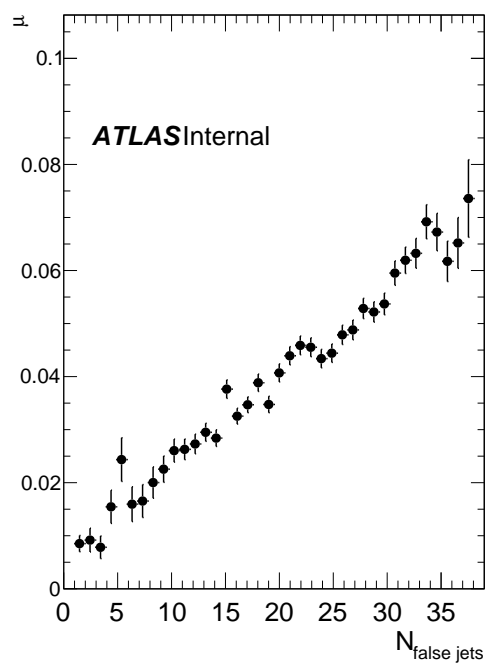


Figure 7.5: Dependence of the unmatched extra jet rate on μ for the baseline simulation.

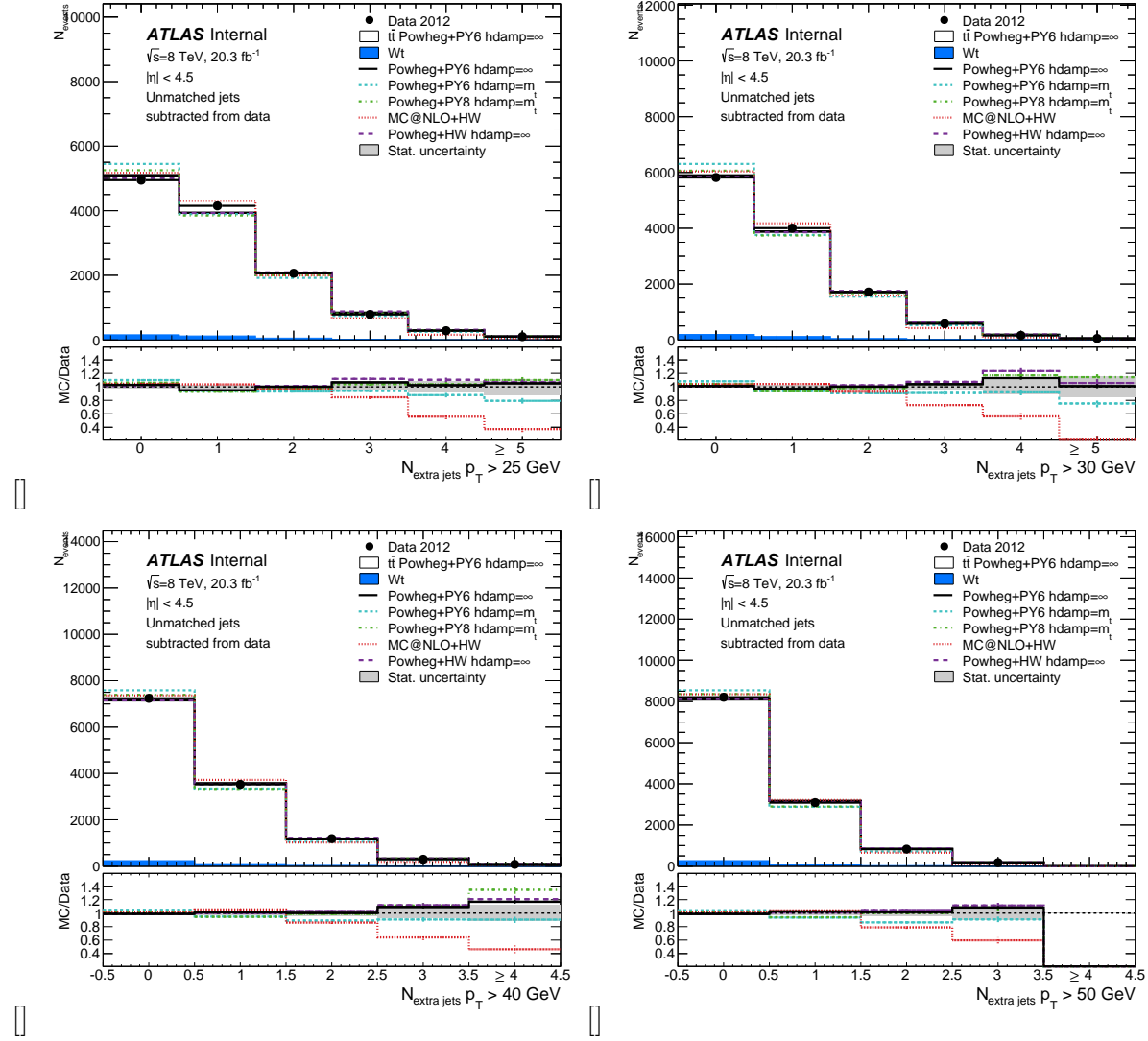


Figure 7.6: Distributions of the reconstructed extra jet multiplicity as a function of p_T threshold in simulation and data. The distributions in data are compared to $t\bar{t}$ simulation normalized to the same number of events as in the data. Extra jets from pileup are excluded in simulation by requiring a match to truth. Extra pileup jets are subtracted from the data. The ratio of different MC samples to data is shown with error bars corresponding to the MC statistical uncertainty and a shaded band corresponding to the data statistical uncertainty. Systematic uncertainties are not shown.

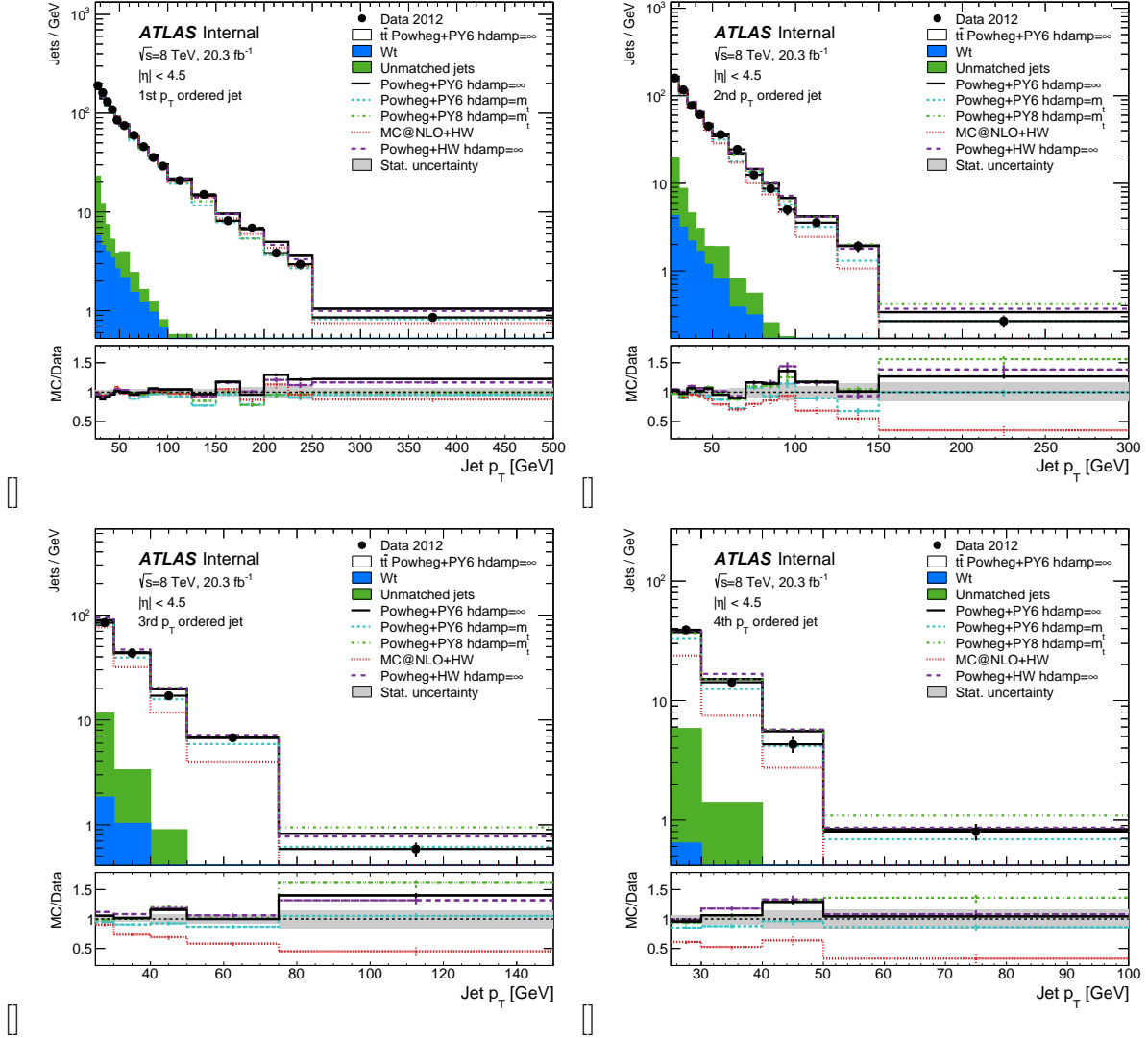


Figure 7.7: Distributions of reconstructed extra jet p_T in simulation and data. The distributions in data are compared to $t\bar{t}$ simulation normalized to the same number of events as in the data. Backgrounds from single top and extra pileup jets are included as background to $t\bar{t}$. The ratio of different MC samples to data is shown with error bars corresponding to the MC statistical uncertainty and a shaded band corresponding to the data statistical uncertainty. Systematic uncertainties are not shown.

Chapter 8

Correction to particle-level

8.1 Introduction to unfolding

8.2 Procedure

This section outlines the procedure used to unfold the reconstructed p_T and multiplicity of the extra jets using RooUnfold [?].¹ This procedure corrects the background-subtracted measured spectrum to the true spectrum for events that pass the fiducial requirements at both the truth and the reconstruction level. Detector effects can distort the true extra jet spectrum in several ways. Hard scattering jets can be lost due to inefficiencies in the reconstruction, resolution smearing will affect the jet p_T , and the rank of two reconstructed jets can be swapped relative to the truth jets (e.g. leading truth jet reconstructed as subleading jet or vice versa). In addition, jets can migrate into and out of the fiducial region. The unfolding procedure corrects for all these effects.

The unfolding is performed on a distribution where the integral of the input distribution is the number of measured jets in the sample and the integral of the output distribution is the number of true jets passing the fiducial requirements.

The full correction procedure is given by the equation:

$$\frac{1}{\sigma_{e\mu+2 \text{ } b\text{-jets}}} \frac{d\sigma_{\text{jet},i}}{dp_T} = \frac{1}{N_{\text{events}}} \sum_j f^i \left(\mathbf{M}^{-1} \right)_{\text{reco},j}^{\text{true}, i} g^j (\mathcal{N}_{\text{reco}}^j - \mathcal{N}_{\text{bkgnd}}^j) . \quad (8.1)$$

$\mathcal{N}_{\text{reco}}^j$ gives the raw distribution measured from data. The estimated extra jet background, $\mathcal{N}_{\text{bkgnd}}^j$ is subtracted from this raw distribution. A ‘feed-in’ factor g^j corrects for migration across the fiducial boundary (cases where the reconstructed jet has $p_T > 25$ GeV but the truth jet has $p_T > 25$ GeV). The migration matrix $\mathbf{M}_{\text{reco},j}^{\text{true}, i}$ relates the number of jets in truth bin i to the number in reconstructed bin j . The correction factor f^i removes the bias

¹Due to important bug fixes necessary for error propagation in this analysis, the development version of RooUnfold is used.

in the extra jet spectrum introduced by the event selection. Finally, the number of jets is normalized to the number of $e\mu + 2 b$ -jets events passing the fiducial requirements (N_{events}) to obtain the final distribution.

This section is organized as follows. First, the scheme for binning jets in both p_{T} and rank is discussed. Second, the method for the unfolding is outlined. Third, the correction factor for event selection is discussed.

8.2.1 Binning

In order to account for the migration effects described above in a single procedure, jets are binned according to both their p_{T} value and rank. For each jet rank, variable sized p_{T} bins are chosen to satisfy two criteria. First, each bin must have at least 10 entries for the data. Second, each bin should show bias of less than 10% of the statistical uncertainty in the closure test discussed in Section 8.4.1. In cases where the second criterion fails, neighboring bins are combined until the closure test passes this criterion. Further studies showing the purity, stability, and p_{T} resolution for the binning can be found in Appendix ??.

The rank (R) and p_{T} of each jet in an event can be mapped to a single integer bin number $\mathcal{N}(p_{\text{T}}, R)$. The bin boundaries are given in Table 8.1. The last p_{T} bin for each rank is treated as an overflow bin.

Both the p_{T} distribution and multiplicity of the extra jets can be recovered from the distribution $\mathcal{N}(p_{\text{T}}, R)$. The p_{T} distribution of the R^{th} jet is obtained directly from $\mathcal{N}(p_{\text{T}}, R = k)$. The jet multiplicity can be obtained by integrating over p_{T} : the number of events with at least j jets with $p_{\text{T}} \geq p$ is given by:

$$N(\geq j) = \begin{cases} N_{\text{total}} & : j = 0 \\ \int_p^{\infty} \mathcal{N}(p_{\text{T}}, R = j) dp_{\text{T}} & : j > 0 \end{cases} \quad (8.2)$$

Then the number of events with exactly j jets is given by:

$$N(j) = N(\geq j) - N(\geq j + 1) \quad (8.3)$$

and the total number of jets with exactly 0 jets is $N(0) = N_{\text{total}} - N(\geq 1)$, where N_{total} is the total number of events.

Table 8.1: Binning for unfolding of extra jets. Jets are binned simultaneously in both rank (p_{T} order) and p_{T} . For each jet rank, variable sized p_{T} bins are chosen so that at least 10 data events fall in each bin. The first bin in p_{T} for each rank is treated as underflow bins. These bins are not reported as part of the measurement.

Bin number	Jet rank	Jet p_{T} (GeV)
1	1	25 – 30
1	2	30 – 35

Continued on next page

Table 8.1 –Continued from previous page

Jet rank	Bin number	Jet p_T (GeV)
1	3	35 – 40
	4	40 – 45
	5	45 – 50
	6	50 – 60
	7	60 – 70
	8	70 – 80
	9	80 – 90
	10	90 – 100
	11	100 – 125
	12	125 – 150
	13	150 – 175
	14	175 – 200
	15	200 – 225
	16	225 – 250
	17	> 250
	18	25 – 30
2	19	30 – 35
	20	35 – 40
	21	40 – 45
	22	45 – 50
	23	50 – 60
	24	60 – 70
	25	70 – 80
	26	80 – 90
	27	90 – 100
	28	100 – 125
	29	125 – 150
	30	> 150
3	31	25 – 30
	32	30 – 40
	33	40 – 50
	34	50 – 75
	35	> 75
4	36	25 – 30
	37	30 – 40
	38	40 – 50
	39	> 50
5	40	25 – 30
	41	> 30

8.2.2 Unfolding procedure

The raw measured spectrum of extra jets is distorted by detector effects such as limited acceptance and efficiency and mismeasurement of jet p_T . In order to compare the data to theoretical predictions, the data must be ‘unfolded’ to obtain the true, underlying physical extra jets. This unfolding algorithm corrects the number of jets reconstructed in each bin $\mathcal{N}_{\text{reco}}^i(p_T, R)$ for detector effects to obtain the unfolded $\mathcal{N}_{\text{unf}}^i(p_T, R)$ according to:

$$\mathcal{N}_{\text{unf}}^i = \sum_j (\mathbf{M}^{-1})_{\text{reco},j}^{\text{true},i} g^j (\mathcal{N}_{\text{reco}}^j - \mathcal{N}_{\text{bkgd}}^j) \quad (8.4)$$

The procedure begins with the raw $\mathcal{N}_{\text{reco}}^j$ distribution measured from data.

First, the estimated extra jet background, $\mathcal{N}_{\text{bkgd}}^j$ is subtracted. This background is estimated from data and further discussed in Section 7.2. Sources of background include jets from pileup and cases where detector effects result in a single truth jet being split into two jets in the reconstruction. In simulation, background removal is done by requiring a match to a truth jet.

Next, a factor g corrects for migration across the fiducial boundary in reconstruction. For each bin j , g^j gives the fraction of reconstructed jets matched to truth jets inside the fiducial boundary (> 25 GeV):

$$g^j \equiv \frac{\mathcal{N}_{\text{reco match } < 25 \text{ GeV}}^j}{\mathcal{N}_{\text{all reco}}^j}$$

Figure 8.1 shows this factor estimated for several NLO $t\bar{t}$ generators. The baseline PowHeg+Pythia hdamp= is used to correct the data.

The response matrix $\mathbf{M}_{\text{reco},j}^{\text{true},i}$ gives the number of jets reconstructed with bin number j ; bin number i is obtained from true p_T and rank. The matrix is filled from simulated events that pass both reconstructed and truth selection requirements. Figure 8.2 provides a graphical representation of $\mathbf{M}_{\text{reco},j}^{\text{true},i}$. The matrix is largely diagonal, showing that jets are most likely to be constructed with the correct p_T and rank. However, there are significant numbers of truth subleading jets reconstructed as leading jets (for example $\mathbf{M}[1, 18; 19, 32]$), and truth leading jets reconstructed as subleading jets (for example $\mathbf{M}[19, 32; 1, 18]$). This type of migration motivates the simultaneous binning via both rank and p_T .

In RooUnfold, detector inefficiencies (cases where a true object is not reconstructed) are entered into the response matrix. These “misses” are shown in Figure 8.2(b) and are accounted for in the unfolding.

The response matrix is inverted using iterative Bayesian unfolding [?], which reduces fluctuations from instabilities in the inversion process. The number of iterations has been set to 2. Details on the procedure used to determine the optimal number of iterations are described in Appendix ???. Singular value decomposition unfolding cannot be used since the input spectrum is not smooth [?].

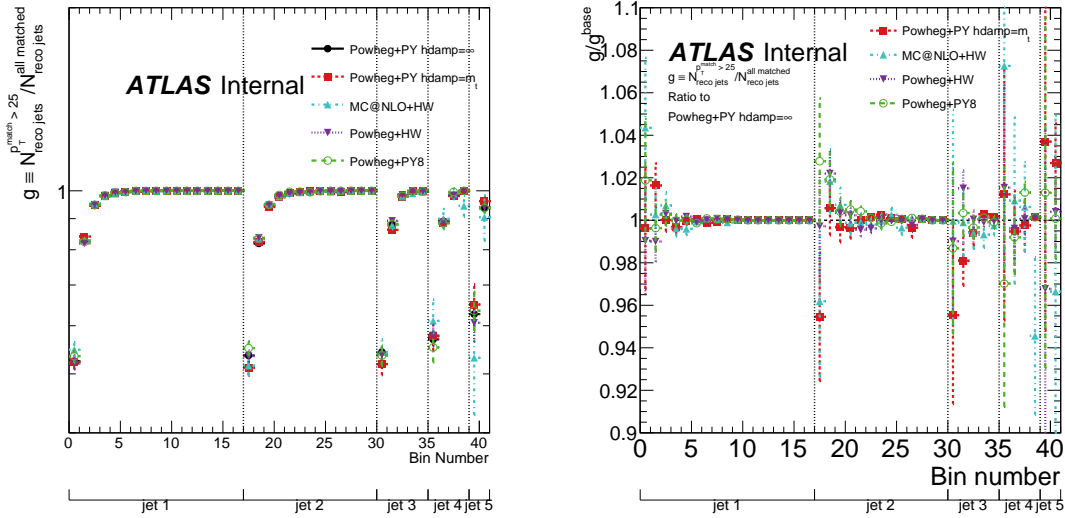


Figure 8.1: Fraction of reconstructed extra jets with truth matches inside the fiducial region (a) and ratio of alternate generators to the baseline (b). This factor is used to correct the data for p_T smearing across the fiducial boundary.

8.2.3 Bias in extra jet distributions due to event selection requirements

8.3 Misidentified events

The unfolding procedure described above returns unbiased extra jet distributions for events passing *both* the truth and reconstruction selection. This subsample of events has different kinematics from events passing the truth only selection. Therefore, the extra jet distributions obtained from the unfolding are biased with respect to the truth selection. In addition, a secondary contribution to the bias results from events where one of the two reconstructed b -jets is in fact a mistag. These biases are corrected using a bin-by-bin correction factor that is applied after the unfolding.

To understand the contributions to this correction, events that fall outside the combined truth and reconstructed fiducial region are classified and their kinematic distributions are studied. These studies use the PowHeg+Pythia $\text{hdamp}=\infty$ $t\bar{t}$ baseline simulation. Table 8.2 gives the number of events passing the fiducial selection for different combinations of reconstruction and truth selection. Events passing both reconstructed and truth selection are properly handled by the unfolding and used to fill the migration matrix, but events that pass one set of selection criteria and not the other require additional corrections. The subsections below provide additional information on each failure category.

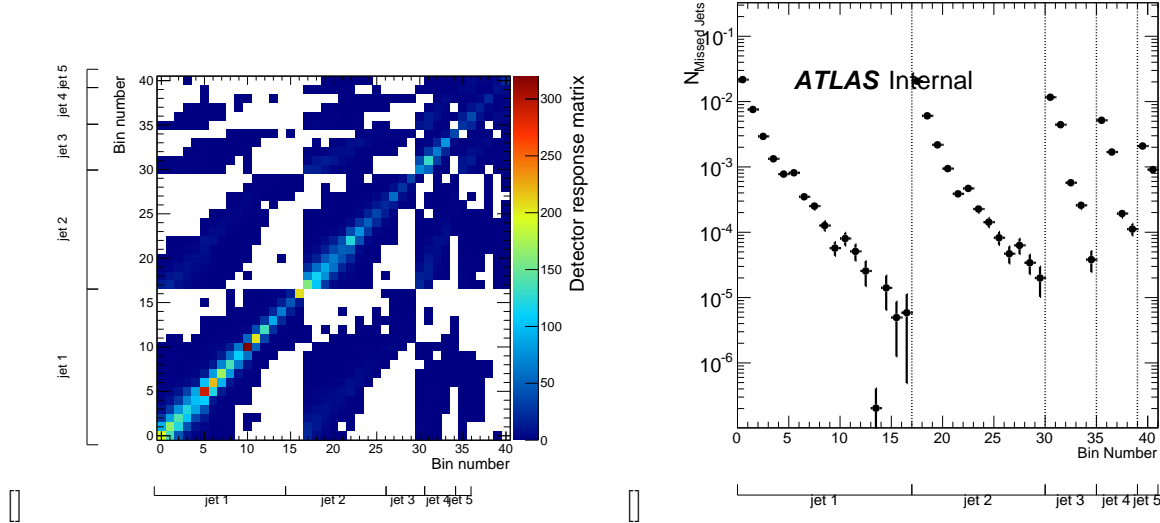


Figure 8.2: Migration matrix between the truth and reconstructed number of extra jets in each bin (a) and distribution of ‘missed’ truth jets not matched to reco jets (b). Jets are binned according to both p_T value and rank. The matrix is filled from events passing both reconstructed and truth $e\mu+2-b$ jet events in the baseline $t\bar{t}$ simulation. ‘Missed’ jets are handled by the RooUnfold framework.

8.3.0.1 Reconstructed events that fail truth event selection

Table 8.3 shows that 95.85% of reconstructed $e\mu+2$ b -jet $t\bar{t}$ events also pass the truth selection and 4.15% of these are *misclassified* events that fail. This table breaks these events into 5 categories:

1. Lepton fiducial: dressed truth e or μ fails the fiducial p_T or η cuts, while reconstructed e or μ passes.
2. Lepton jet overlap:dressed truth e or μ overlaps with a truth jet, while reconstructed e or μ does not overlap with a reconstructed jet.
3. Lepton non-prompt: truth e or μ leptons result from the decay of a hadron or are other background (such as conversions).
4. b -jet fiducial: truth b -jet fails the fiducial p_T or η cuts.
5. b -jet other: truth jet not matched to B hadron, meaning that the reconstructed b -jet was mistagged. This category also includes a small number of cases where the two reconstructed b -jets are matched to a single truth jet or one of the two reconstructed b -jets does match any truth jet.

Figure 8.3 shows the electron p_T , b -jet p_T , b -jet MV1 weight, and extra jet multiplicity for events in the above categories. Additional plots of the kinematics and extra jets for these

Category	N_{events}
Reco	11997.1
Truth	43496.9
Reco AND truth	11499.0
Reco AND NOT truth	498.2
NOT Reco AND truth	31877.7

Table 8.2: Number of events passing different combinations of truth and reconstructed selection requirements.

events can be found in Appendix ???. Events failing the truth lepton or b -jet fiducial cuts arise mainly from resolution smearing of the p_T . These produce a softer spectrum for the reconstructed lepton p_T in Figure 8.3(a) and reconstructed b -jet p_T in Figure 8.3(b). Misclassified events with overlap between a lepton and a jet show a harder reconstructed lepton p_T spectrum and higher extra jet multiplicity, suggesting that a jet has been reconstructed from a lepton. Events with non-prompt leptons show similar properties. Finally, in the ‘ b -jet other’ category, the MV1 of the reconstructed b -jet is much lower than other types of events, suggesting that a light jet has been mistagged as a b -jet. The $\sim 1\%$ rate in this category is consistent with the mistag estimate for b -jets given in Ref. [?].

8.3.0.2 Truth events that fail reconstructed event selection

Due to detector inefficiencies, the majority of events passing the truth selection fail the reconstruction selection (*missed events*). Table 8.4 shows the events that pass truth selection broken into categories based on which objects were correctly reconstructed. The largest contributions come from failure to reconstruct the electron or the second b -jet in the event. A large fraction of these come from migrations across the fiducial boundary due to p_T smearing.

Figure 8.4 shows the truth b -jet p_T , extra jet multiplicity, leading extra jet p_T and sub-leading extra jet p_T by category. Additional distributions can be found in Appendix ???. The b -jet p_T is much softer for events that are not reconstructed. The extra jets in these events are softer as well.

The differences in the extra jet distributions for these events can be explained by studying the relationship between the b -jet p_T and the number and kinematics of the extra jets. Figure 8.5 shows the extra jet multiplicity and p_T in truth events in bins of b -jet p_T . Softer b -jets correspond to events with softer and fewer extra jets. This effect is likely the result of the dependence of the b -jet p_T on p_T^{top} .

In summary, events that fail the reconstruction requirements on the b -jets have a lower extra jet multiplicity and softer jets than those that fall in other categories.

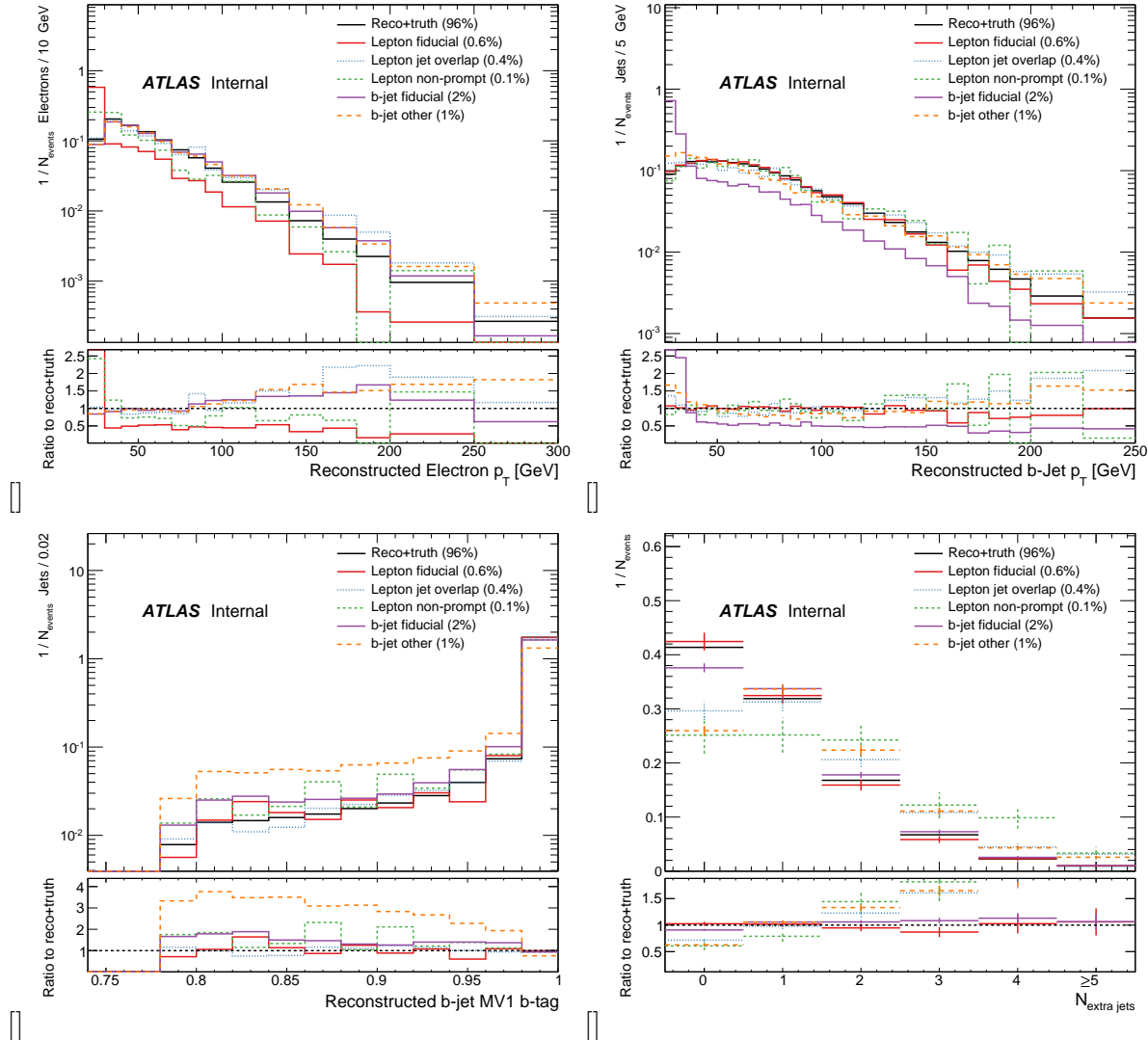


Figure 8.3: Distributions of the (a) $e p_T$, (b) b -jet p_T , (c) b -jet MV1 weight and (d) extra jet multiplicity. Each distribution is normalized by the number of events falling in that category. Events were simulated with PowHeg+Pythia hdamp= ∞ $t\bar{t}$.

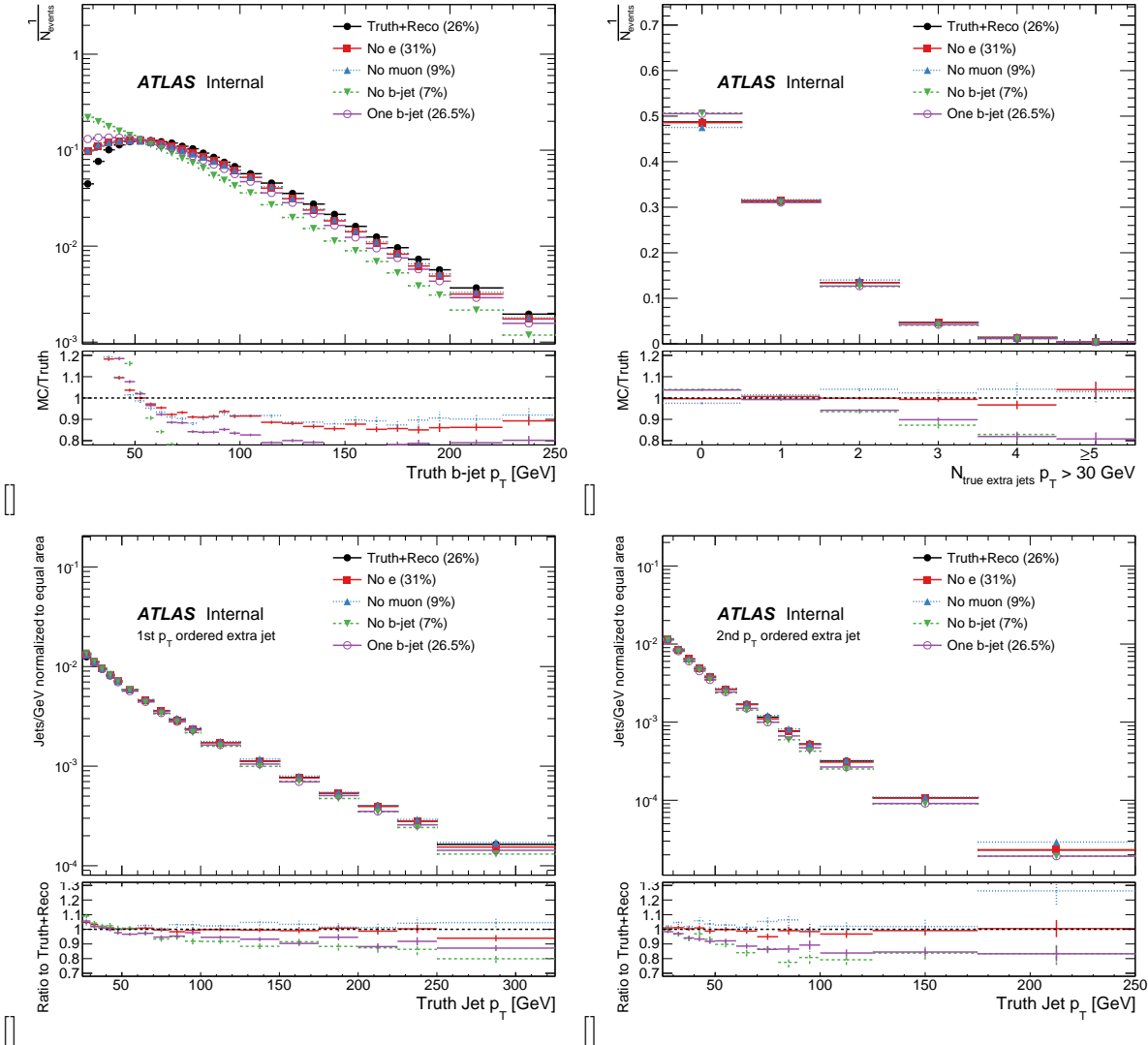


Figure 8.4: Distributions of the truth (a) b -jet p_T , (b) extra jet multiplicity, (c) leading extra jet p_T and (d) subleading extra jet p_T . Each distribution is normalized by the number of events falling in that category. Events were simulated with PowHeg+Pythia hdamp= ∞ $t\bar{t}$ and required to pass the fiducial truth $e\mu+2$ b -jet selection.

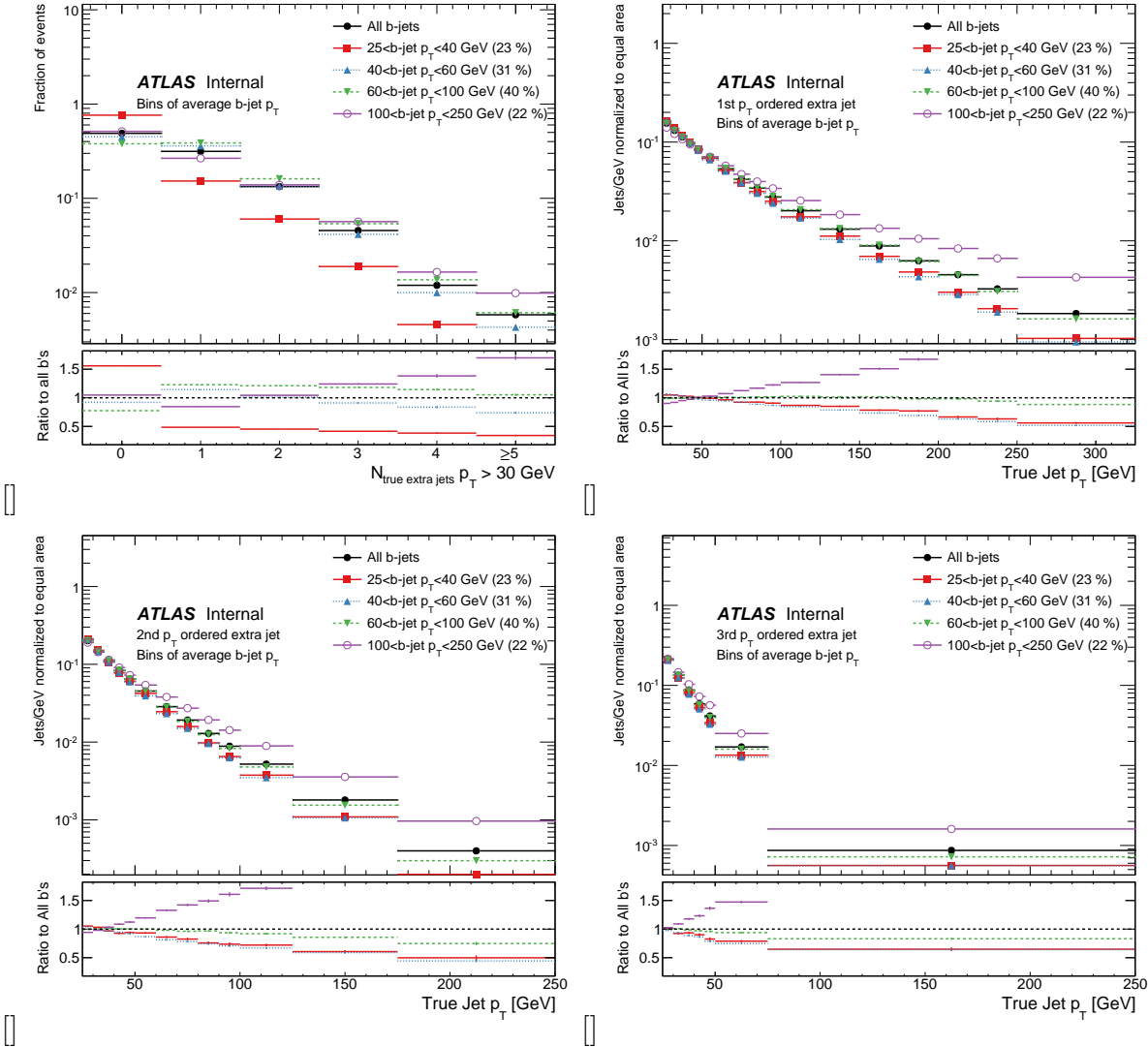


Figure 8.5: Distributions of the truth (a) extra jet multiplicity, (b) leading extra jet p_T , (c) subleading extra jet p_T and (d) subsubleading extra jet p_T in bins of the average of the p_T of the two truth b -jets used to select the event. Each distribution is normalized by the number of events falling in that bin. Events were simulated with PowHeg+Pythia $\text{hdamp}=\infty$ $t\bar{t}$ and required to pass the fiducial truth $e\mu+2$ b -jet selection.

Category	N_{events}	(%)
Lepton fiducial	67.5	0.56
Lepton jet overlap	50.6	0.42
Lepton non-prompt	10.9	0.09
b -jet fiducial	245.8	2.05
b -jet other	123.4	1.03
Total misclassified	498.2	4.15
Passes reco and truth selection	11499.0	95.85
Total reco events	11997.1	100.00

Table 8.3: Number of selected reconstructed events that fail truth selection categorized by reason they have failed. The selections are applied sequentially in the order listed in the table.

Category	N_{events}	(%)
No e	13472.3	31.06
No μ	3743.0	8.63
same-sign $e\mu$	161.1	0.37
0 b -jets	2986.0	6.88
1 b -jet	11515.3	26.55
Missed total	31877.7	73.49
Passes reco and truth selection	11499.0	26.51
Total truth events	43376.7	100.00

Table 8.4: Number of truth events that fail reconstruction selection categorized by reason they have failed. The selections are applied sequentially in the order listed in the table.

8.3.0.3 Event selection correction factors

To correct for the effects discussed above, bin-by-bin correction factors f^i are applied to the unfolded distribution as shown in Equation 8.1. These factors are derived by comparing unfolded simulated events that pass the reconstruction selection (with no particle level event selection) to particle level truth distributions where no reconstruction requirements are applied. Each bin's correction factor is given by:

$$f^i \equiv \frac{\mathcal{N}_{\text{true}}^i}{\mathcal{N}_{\text{unf}}^i} \quad (8.5)$$

The simulated data used for this study includes $t\bar{t}$ and single top events with their relative contributions determined from their NLO cross sections. $\mathcal{N}_{\text{true}}^i$ and $\mathcal{N}_{\text{unf}}^i$ are normalized by number of events passing $e\mu + 2 b$ -jets selection at the reconstructed and particle level,

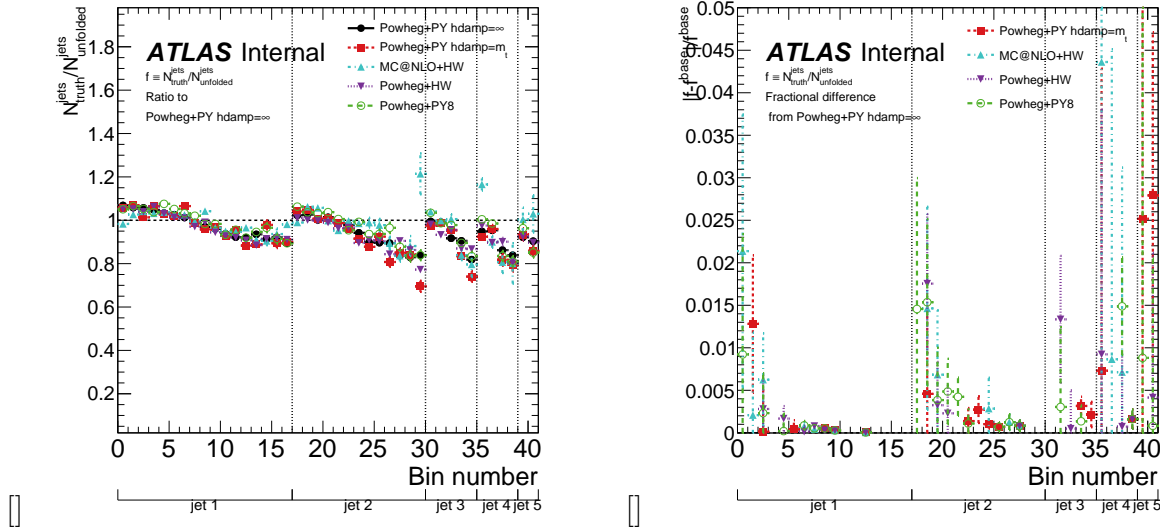


Figure 8.6: (a) Ratio of unfolded extra jets to truth extra jets different $t\bar{t}$ generators (including a 2.9% contribution from single top). (b) Fractional difference of the correction factor from baseline for different generators. Extra jets in events passing reconstructed and truth selection for each generator are added to single top and used to fill a response matrix. Then each generator is unfolded against itself, using all selected reconstructed events. Extra jet truth distributions are made without any reconstruction requirements. Finally, the unfolded distribution is divided by the truth distribution to obtain a correction factor for each bin.

respectively. Since the final measurement given by Equation 8.1 is normalized by the number of events in data, the correction factor f^i corrects only for the bias in the extra jet spectrum, not the efficiency in number of events. Figure 8.6 shows the correction factors obtained using different choices of generator for the $t\bar{t}$ component. The final correction factors used for data are taken from the baseline PowHeg+Pythia $\text{hdamp}=\infty$ sample. Systematic uncertainties associated with generator dependence of this factor are discussed in Section 9.5.

8.4 Validation

RooUnfold allows propagation of the full covariance matrix of the measured distribution through the unfolding. The package returns a covariance matrix, which is used to determine the uncertainties on the unfolded spectrum. The covariance matrix X on the unfolded distribution is calculated via pseudoexperiments. The diagonal elements of this covariance matrix give the uncertainties on the bins of p_T and rank.

The agreement between an unfolded spectrum and truth distribution can be estimated using a χ^2 test (including correlations among bins):

$$\chi^2 = (\mathcal{N}_{\text{unf}} - \mathcal{N}_{\text{true}})^T X^{-1} (\mathcal{N}_{\text{unf}} - \mathcal{N}_{\text{true}}) \quad (8.6)$$

The inverse covariance matrix, X^{-1} , is determined using SVD with SciPy [?].

This χ^2 is used validate the unfolding procedure with different MC generators in Sections 8.4.1-8.4.2, as well as to assess the agreement of generators with the fully corrected data in Section ??.

8.4.1 Closure test

The closure test validates the unfolding procedure using simulation. The stability of unfolding can depend on the statistical power of the input data. To ensure that the the closure test appropriately accounts for this effect, the test is performed using pseudoexperiments with the same statistical power as the data.

In the closure test, the baseline $t\bar{t} + 3\% Wt$ simulation is used to fill the migration matrix and one thousand pseudoexperiments are performed using randomly chosen subsamples of events. Each pseudoexperiment is chosen so the number of events is equal to that of data. The extra jet distribution from each pseudoexperiment is then unfolded. Each unfolded distribution is compared to the truth distribution obtained from the full sample of events used to train the migration matrix.

The bias $B^i = \mathcal{N}_{\text{truth}}^i - \mathcal{N}_{\text{unfold}}^i$ and pull $P^i = (\mathcal{N}_{\text{truth}}^i - \mathcal{N}_{\text{unfold}}^i)/\sigma_{\text{unfold}}$ distributions are measured for each bin i . Figure 8.7 shows the mean pull and its uncertainty in bins of p_T for jets of rank 1 through 5. The shaded bands indicate the width of the pull distribution, obtained from a Gaussian fit. The pull distributions for each bin are shown in Appendix ???. The mean pull is close to zero and has a width close to unity. This demonstrates that the unfolding procedure has no significant bias and that the statistical uncertainties on the unfolded distribution are properly estimated. Additional test of the unfolding are provided in Appendix ??.

In addition to the pull and bias, the average χ^2 between the unfolded pseudoexperiments and the true distribution is computed using Equation 8.6. The χ^2 obtained in the closure test is 42 for 41 degrees, indicating that the inverse covariance matrix returned from RooUnfold appropriately estimates the correlated uncertainties.

8.4.2 Stress test

‘Stress’ tests assess the effect of the input p_T spectrum on the unfolding algorithm by unfolding pseudoexperiments produced from alternate $t\bar{t}$ MC generators (described in Section ??) using the response matrix and correction factors obtained from the baseline.

To study the stability of the unfolding with respect to changes in the input jet p_T and multiplicity spectra, pseudoexperiments are constructed by reweighting the truth jet spectrum

in the baseline MC sample. The weight for each bin is given by the ratio of the alternative generator to the baseline². This procedure isolates the uncertainty associated with the choice of spectrum from other sources of instability (e.g. JES), which are accounted for separately.

Stress tests have been performed using the following samples: PowHeg+Pythia, PowHeg+Herwig, MadGraph+Pythia, MC@NLO+Herwig, PowHeg+Pythia8, PowHeg+Pythia $\text{hdamp} = m_t$, RadHi MadGraph+Pythia and RadLo MadGraph+Pythia. Each of the alternate $t\bar{t}$ samples are unfolded with 1000 pseudoexperiments against a migration matrix filled from the baseline $t\bar{t}$ simulation. In both the migration matrix and the samples, a 3% contribution from single top is included. Correction factors (f and g in Equation 8.1) are also taken from the baseline.

The pull distributions for the alternate generators unfolded against the baseline are provided in Appendix ??, including studies of number of iterations.

Figure 8.8 shows the fractional bias obtained for the stress test for four representative alternative generators. Though bin-to-bin fluctuations around zero are visible, these fluctuations fall largely within the one sigma error contour. For MC@NLO+Herwig, the disagreements become large for jets of rank 3 and higher. The jet multiplicity in MC@NLO+Herwig at reconstruction level is significantly lower than the data. For MadGraph+Pythia deviations above the one sigma level are observed for low jet p_T . The MadGraph+Pythia is significantly steeper than that of PowHeg+Pythia $\text{hdamp} = \infty$. This will affect the size of the feed-in correction g_i . The differences with respect to MadGraph+Pythia are included in the systematic uncertainties described in Section 9.5.

²An alternative reweighting procedure where the ratios were fit to a smooth function was also studied. Changes with respect to the procedure described here were small

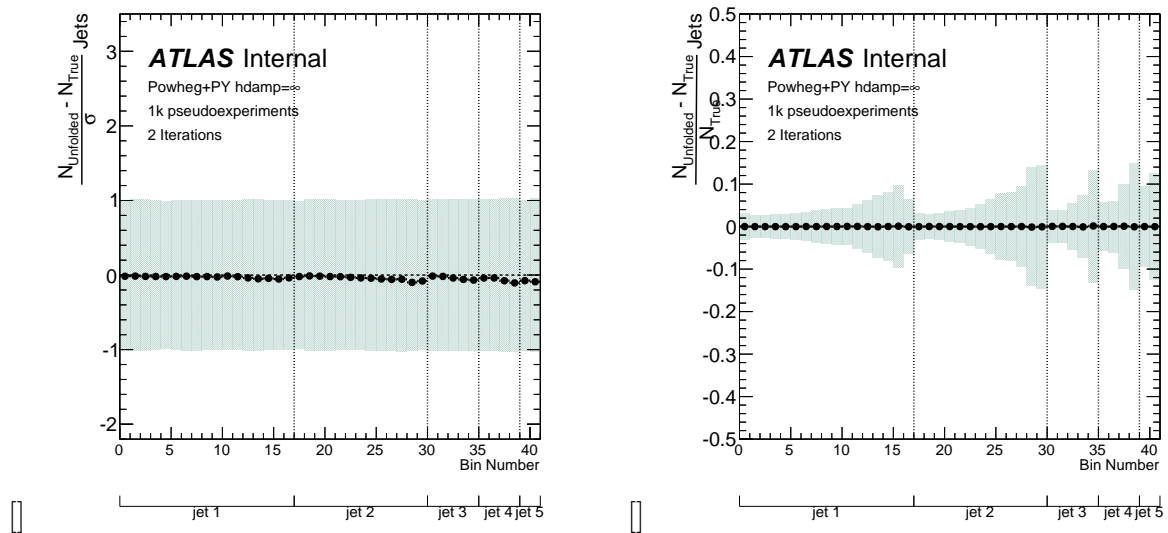


Figure 8.7: (a) Pull distribution and (b) fractional bias for the extra jets from the baseline $t\bar{t}$ simulation unfolded against a matrix filled with the baseline $t\bar{t}$ simulation with all correction factors. The Bayesian unfolding method with 2 iterations is used. One thousand pseudoexperiments, each the size of the events in data, are randomly selected from the sample and unfolded. Each bin of the pull distribution over the pseudoexperiments is fit with a gaussian. The black points show the fitted mean of each bin. A fitted mean of zero shows the unfolding is not significantly biased. The blue band shows the fitted σ of each bin. A fitted σ of one shows the unfolding correctly estimates the errors.

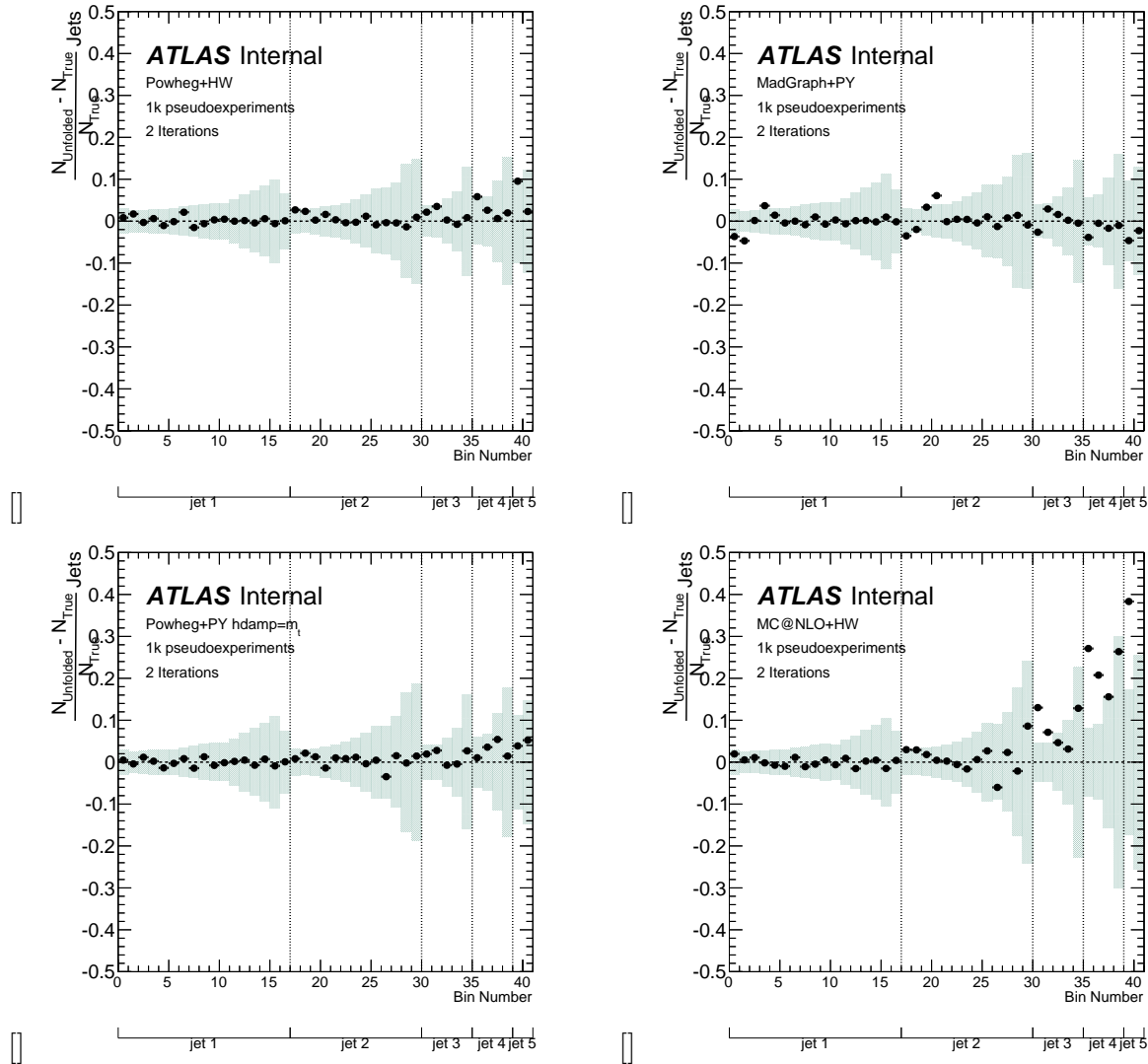


Figure 8.8: Fractional bias distributions for pseudoexperiments from alternative generators unfolded against a matrix filled with the baseline simulation. The truth spectrum of the baseline sample is reweighted to match jet p_T and multiplicity spectra of (a) PowHeg+Herwig (b) MadGraph+Pythia, (c) PowHeg+Pythia $hdamp=m_t$, and (d) MC@NLO+Herwig simulation. One thousand pseudoexperiments, each the size of the events in data, are constructed for each generator and unfolded. The Bayesian unfolding method with 2 iterations is used. Each bin of the distribution over the pseudoexperiments is fit with a gaussian. The black points show the fitted mean of each bin and the blue band shows the fitted sigma.

Chapter 9

Sources of uncertainty

9.1 Types of uncertainty

Bias versus spread

9.2 Detector modeling

Detector modeling uncertainties are evaluated using the baseline $t\bar{t}$ simulation by varying the default scale factors within their systematic uncertainties using the TopRootCore framework. Jet-related uncertainties, primarily the jet energy scale, are the biggest source of detector modeling uncertainty. Uncertainties due to lepton isolation, reconstruction, identification and trigger efficiencies have been evaluated, but found to be negligible.

9.2.1 Nuisance parameters

Jet energy scale uncertainties are evaluated using the JetUncertainties-00-08-25 package and the InsituJES2012_23NP_ByCategory.config configuration. Each of the 23 nuisance parameters is independently varied. The jet energy resolution (JER) uncertainty is derived from measurements of the jet response in data and found to agree well with simulation. The uncertainty is evaluated using the ApplyJetResolutionSmearing-00-01-04 package. Jet energy is smeared using a function that depends on p_T and η . Because this procedure only allows for an increase in resolution, the resulting uncertainty is symmetrized. The uncertainty on the jet finding efficiency is parametrized in the JetEffiProvider-00-00-05 tool. This uncertainty is propagated to the extra jet distribution by randomly dropping jets in the nominal simulation and reanalyzing the resulting data. The resulting difference is then symmetrized.

The b -tagging scale factor and uncertainty for b -tagging efficiency and mistag is evaluated using the BTaggingCalibrationDataInterface. To avoid using efficiencies and mistag rates measured from the same events as this analysis, the System 8 calibrations are used.

9.2.2 Computation of uncertainty

The impact of these systematic uncertainties on reconstructed extra jets is evaluated by varying each individual scale factor and reanalyzing the simulated data using the same prescription as for the nominal. The standard ATLAS procedure for evaluating detector systematic uncertainties is to vary each nuisance parameter individually by $\pm 1\sigma$. However, this method does not allow the construction of a full covariance matrix. The procedure used here is similar to that used in Ref. [?]. A set of 1000 modified samples is constructed from the full statistics of the PowHeg+Pythia hdamp= ∞ simulation. For each sample, each nuisance parameter i is varied by $\lambda_i = \text{Gauss}(0, \sigma_i)$, where σ_i is the nuisance parameter uncertainty. The systematic covariance matrix from these samples is then computed:

$$C_{ij} = \frac{1}{1000} \sum_{x=0}^{1000} (\mathcal{N}_x^i - \langle \mathcal{N}^i \rangle) (\mathcal{N}_x^j - \langle \mathcal{N}^j \rangle) \quad (9.1)$$

where $\langle \mathcal{N}^j \rangle$ is the average jets in bin j over all samples and \mathcal{N}_x^j is the number of jets in bin j in a single sample x .

As a cross-check, the uncertainties obtained using this procedure are compared to those obtained using the standard method for the most significant subset of nuisance parameters. Figure 9.1 shows the uncertainties from the 15 JES eigenstates on the p_T for jets of rank=1-4. The band shows the uncertainty obtained from the samples with gaussian variation of all nuisance parameters. The upper and lower lines shows uncertainty from the quadratic sum of the independent variations of each nuisance parameter by $\pm 1\sigma$. The distribution of samples values has fitted $\mu = 1$ and σ consistent with the $\pm 1\sigma$ method.

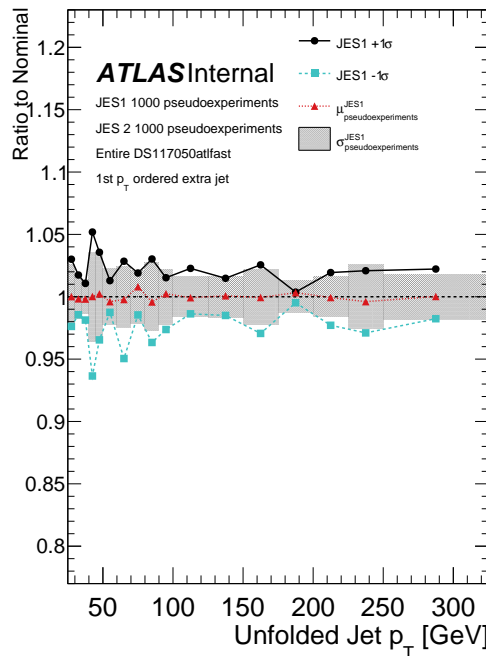
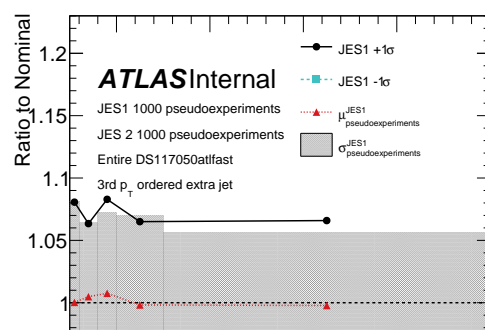
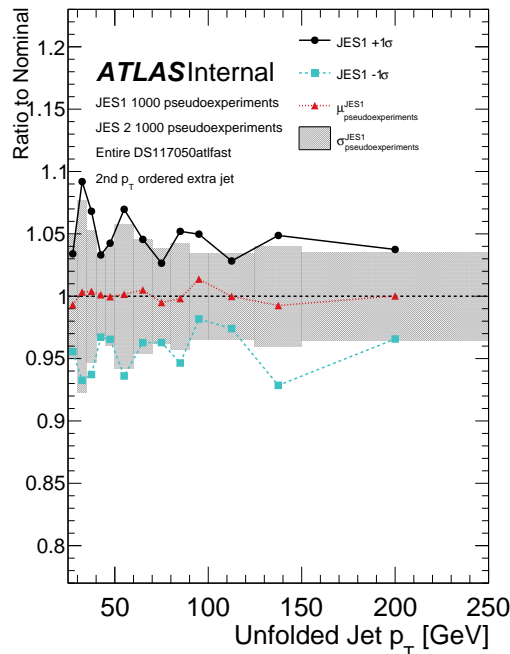
9.3 Single top rate

Since the single top contribution is treated as signal, a systematic uncertainty must be placed on the rate of selected single top events relative to $t\bar{t}$. To assess the uncertainty on the extra jets, the single top rate is varied relative to the baseline 2.9% computed in Table 6.4. The uncertainty for each bin due to the single top is given by the maximum difference between the baseline 2.9% single top and 0% or 5.8% single top. The results of this study can be found in Appendix ??.

$$\sigma_{ij} \equiv \langle \max |\mathcal{N}_{5.8\%}^i - \mathcal{N}_{2.9\%}^i|, \mathcal{N}_{0\%}^i - \mathcal{N}_{2.9\%}^i | \rangle \langle \max |\mathcal{N}_{5.8\%}^j - \mathcal{N}_{2.9\%}^j|, \mathcal{N}_{0\%}^j - \mathcal{N}_{2.9\%}^j | \rangle$$

9.4 Pileup and false jet background

Before unfolding, unmatched jets are subtracted from the measured data distribution. The uncertainty on the modeling of these jets is estimated by taking the difference between the pileup and false jets rates obtained in Section 7.2 with the rate obtained from the baseline PowHeg+Pythia hdamp= ∞ simulation. The unmatched extra jets obtained using these two

[Highest p_T extra jet][2nd highest p_T extra jet]

methods are shown in Figure 9.4. The two distributions agree well at low p_T but differ slightly at higher p_T . This systematic uncertainty is small compared to the statistical uncertainty of the samples.

$$\sigma_{ij} \equiv \langle \mathcal{N}_{\text{false PowHeg+PYTHIA}}^i - \mathcal{N}_{\text{ZeroBias false}}^i \rangle \langle \mathcal{N}_{\text{false PowHeg+PYTHIA}}^j - \mathcal{N}_{\text{ZeroBias false}}^j \rangle$$

9.5 Input extra jet spectrum

Uncertainty due to the modeling of the input $t\bar{t}$ spectrum for the unfolding is taken from stress tests constructed using the method described in Section ??.

Following the prescription outlined by the Top group (see twiki Ref. [?]), the following input generator samples and unfolding procedures are used to evaluate different components of modeling uncertainty:

NLO generator: MadGraph+Pythia are unfolded using a response matrix and correction factors obtained from PowHeg+Pythia $\text{hdamp}=\infty$. MadGraph+Pythia is used rather than MC@NLO+Herwig because MC@NLO+Herwig is inconsistent with the reconstructed distributions.

Shower: PowHeg+Herwig are unfolded using a response matrix and correction factors obtained from PowHeg+Pythia $\text{hdamp}=\infty$.

Radiation: MadGraph+Pythia q^2 up and down are unfolded using a response matrix and correction factors obtained from nominal radiation MadGraph+Pythia.

In all cases, the unfolded result is compared to the truth for the input generator. For each component, the uncertainty is expressed as a covariance matrix obtained from the outer product of the biases:

$$\sigma_{ij} \equiv \langle \mathcal{N}_{\text{unf}}^i - \mathcal{N}_{\text{truth}}^i \rangle \langle \mathcal{N}_{\text{unf}}^j - \mathcal{N}_{\text{truth}}^j \rangle \quad (9.2)$$

The radiation uncertainty is taken from the average bias for MadGraph+Pythia q^2 up and down.

9.6 Statistical uncertainty on migration matrix

As shown in the Figure 8.2(a), the migration matrix has some elements far from the diagonal with very few entries. To account for the uncertainty introduced by the migration matrix statistics, pseudoexperiments are unfolded varying the response matrix while keeping the input spectrum constant. The migration matrix, input spectrum and correction factors are all taken from the baseline PowHeg+Pythia $\text{hdamp}=\infty$ sample. The contribution to the covariance matrix from this component is evaluated according to Equation 9.1.

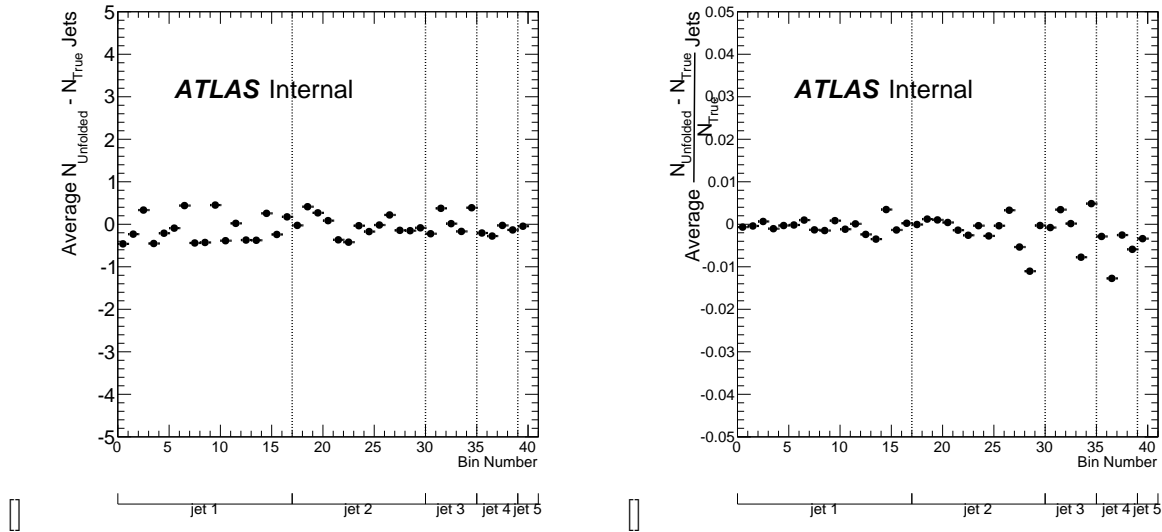


Figure 9.2: (a) bias and (b) fractional bias distributions PDF variations of MC@NLO+Herwigunfolded with the nominal MC@NLO+Herwigmigration matrix. Each bin of the distribution over the pseudoexperiments is fit with a gaussian. The outer product of the bias is used to compute the uncertainty due to the PDF.

9.7 PDF modeling uncertainty

Uncertainty in the modeling of the parton distribution function (PDF) can affect modeling of the extra jets. Following the prescription given in Ref. [?], events are reweighted according to the x and Q^2 of the corresponding PDF variation. PDF variations are taken from the MC@NLO+Herwig sample is used with 52 variations for the CT10 PDF, 40 variations for the MSTW PDF, and 100 variations for the NNPDF¹.

Each variation is unfolded with the nominal MC@NLO+Herwig migration matrix. For each bin, the average bias of the variations with respect to the input spectrum is computed. The outer product of these biases is used to compute the covariance for the PDF uncertainty:

$$\sigma_{ij} \equiv \langle \mathcal{N}_{\text{unf}}^i - \mathcal{N}_{\text{truth}}^i \rangle \langle \mathcal{N}_{\text{unf}}^j - \mathcal{N}_{\text{truth}}^j \rangle$$

9.8 Combined uncertainty

A covariance matrix associated with the statistical uncertainty of the input data spectrum returned from RooUnfold. The covariance due to all sources of uncertainty described above is then added to obtain the final uncertainty on the corrected data. Figure 9.6 shows (a)

¹Though MC@NLO+Herwig shows poor agreement with data, it is the only sample for which x and Q are properly recorded in ATLAS simulation

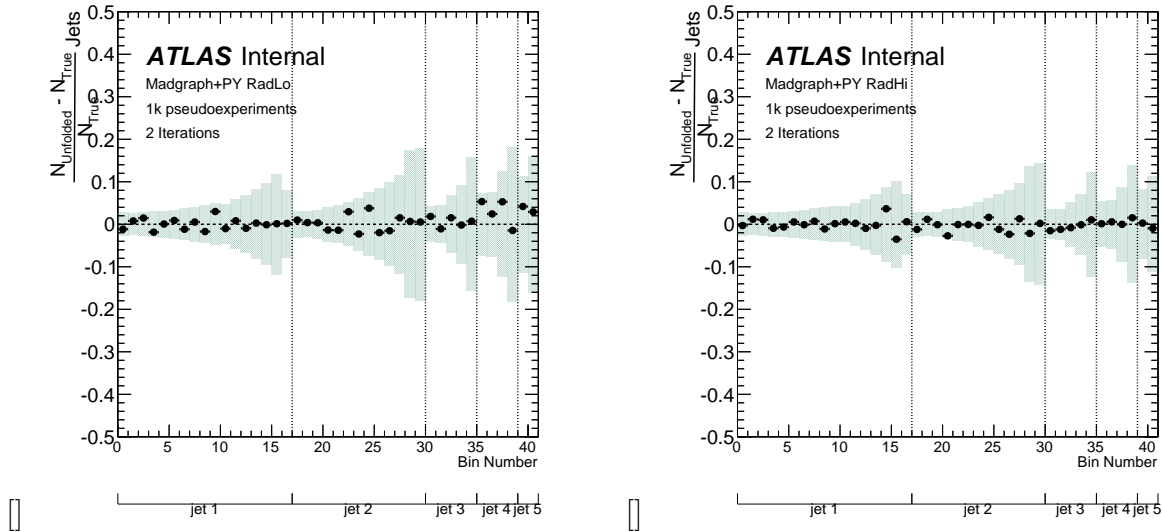


Figure 9.3: Fractional bias distributions for pseudoexperiments from MadGraph+Pythia radiation samples unfolded against a matrix filled with nominal MadGraph+Pythia. The truth spectrum of the baseline sample is reweighted to match jet p_T and multiplicity spectra of (a) MadGraph+Pythia RadLo (b) MadGraph+Pythia RadHi simulation. One thousand pseudoexperiments, each the size of the events in data, are constructed for each generator and unfolded. The Bayesian unfolding method with 2 iterations is used. Each bin of the distribution over the pseudoexperiments is fit with a gaussian. The black points show the fitted mean of each bin and the blue band shows the fitted sigma.

the statistical covariance matrix and (b) total covariance matrix for the unfolded data. The diagonal elements of total matrix are used to obtain uncertainties on the bins of p_T and rank. The entire matrix is used to assess the χ^2 agreement between data and generators.

Figure 9.5 shows the sum of uncertainties from all sources, broken into categories as follows.

Statistics: Statistical uncertainty on the data is returned from RooUnfold

Modeling: NLO generator, radiation, shower and migration matrix statistics uncertainties (Section 9.5-9.6)

PDF: PDF variations, determined from MC@NLO+Herwig(Section 9.7)

Pileup: Uncertainties from JVF nuisance parameters (Section 9.2.1) and false jet modelling (Section 9.4)

JES: Jet energy scale nuisance parameters (Section 9.2.1)

JER/JEFF: Jet energy resolution and jet finding efficiency nuisance parameters (Section 9.2.1)

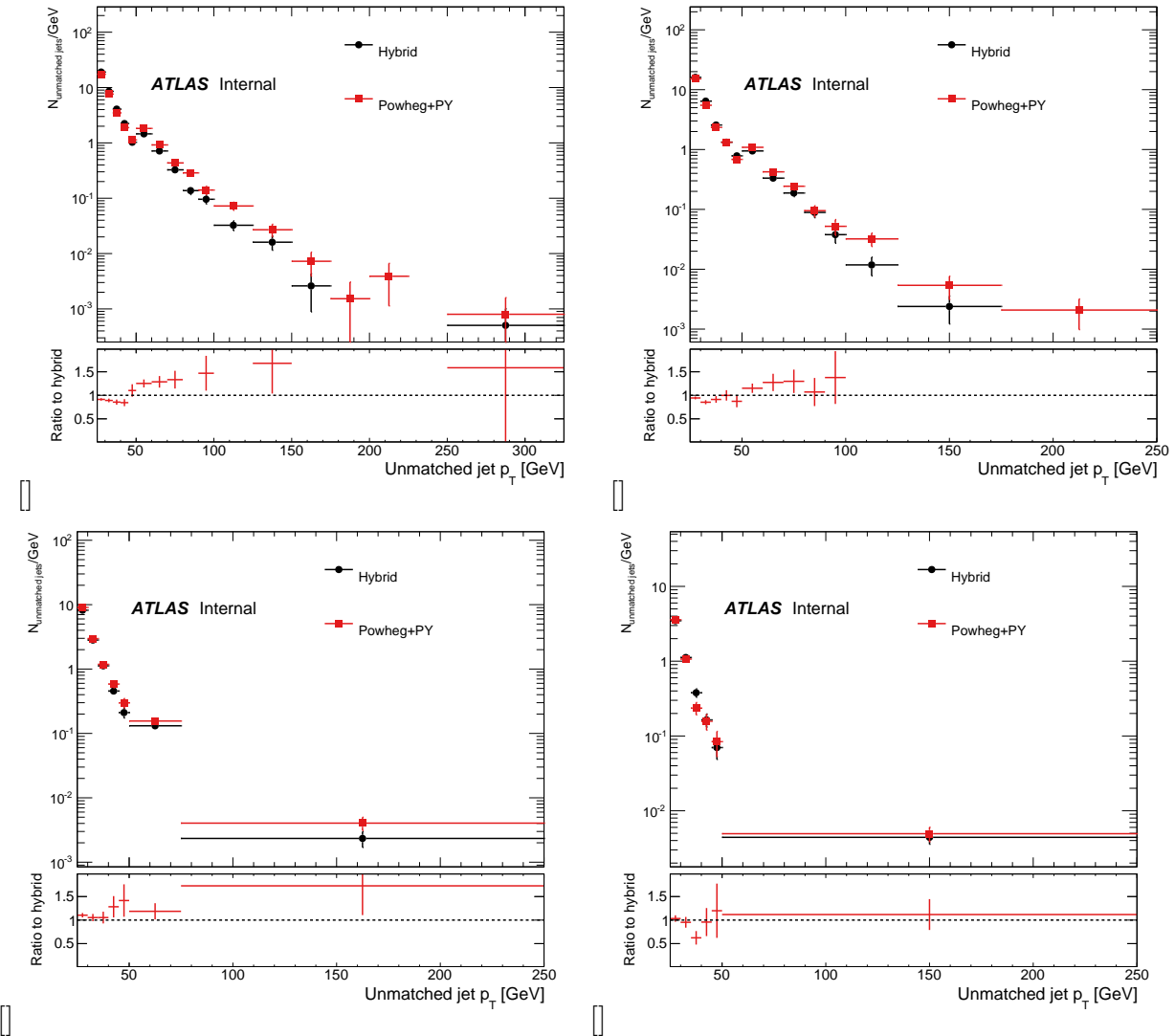
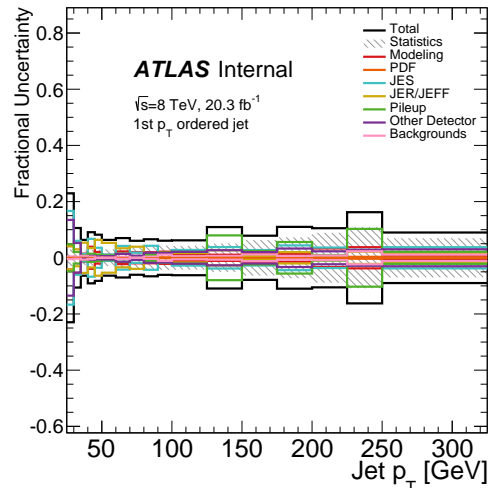
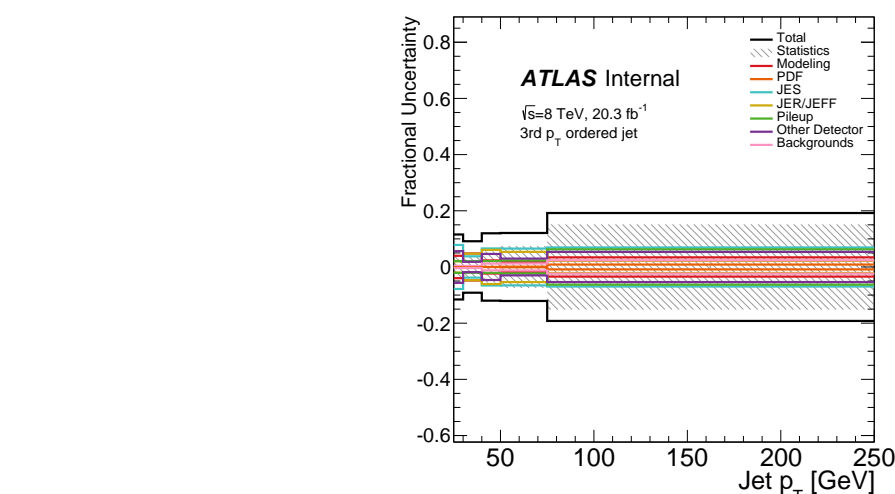
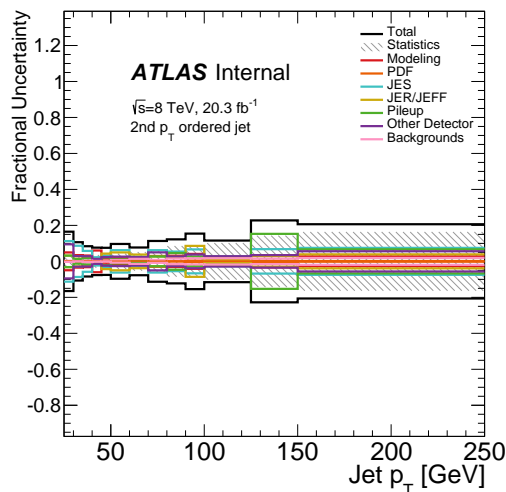
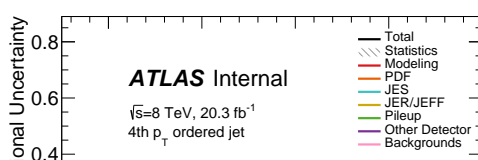


Figure 9.4: Unmatched jets in the baseline $t\bar{t}$ simulation and the hybrid sample. The difference between the two is used to estimate the uncertainty.

Other detector: Lepton and b -tag nuisance parameters not in the JES, JER/JEFF or pileup category.

Backgrounds: Single top rate uncertainty Wt (Section 9.3)

In most bins, statistical uncertainty dominates. At low jet p_T , JES is the largest source of uncertainty. Modeling is the largest source of uncertainty at high jet p_T .

[Highest p_T extra jet][2nd highest p_T extra jet][3rd highest p_T extra jet][4th highest p_T extra

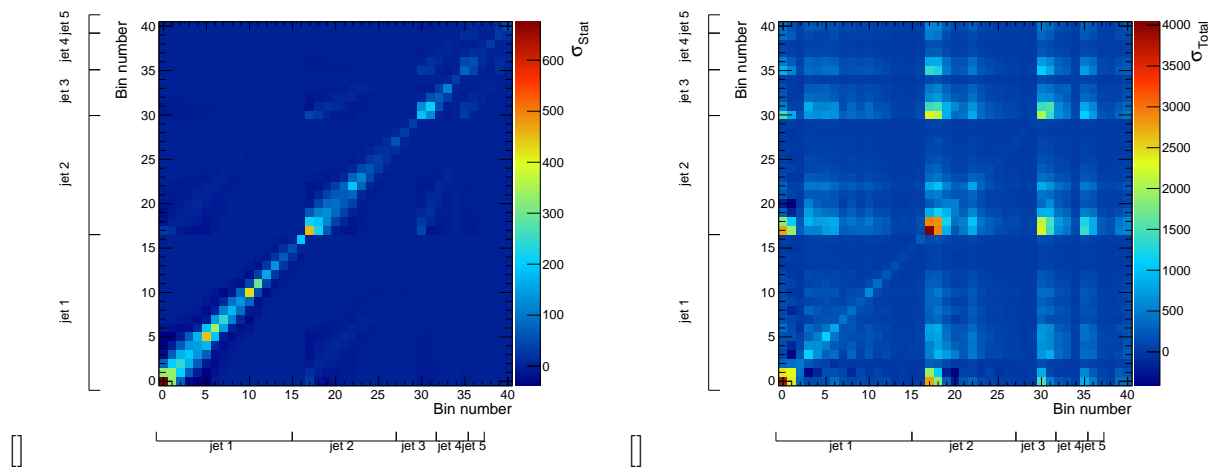


Figure 9.6: (a) The covariance matrix associated with the statistical uncertainty of the input spectrum returned from RooUnfold. (b) The covariance matrix from all sources of uncertainty, obtained by adding the covariance matrices from all sources of systematic uncertainty to (a). This matrix is used to determine the χ^2 agreement between generators and the fully corrected data.

Chapter 10

Results

This chapter presents the final, fully corrected results of the analysis described in the previous chapters. Fully corrected distributions are present, then the corrected data is compared to different MC generators using a χ^2 test. Finally, the results of this χ^2 test are discussed.

10.1 Fully corrected distributions

Figure 10.1 shows the normalized differential cross-section $\frac{1}{\sigma_{e\mu+2 \text{ b-jets}}} \frac{d\sigma_{\text{jet},i}}{dp_T}$ for jets of rank 1-4 and compares the data to four next-to-leading order generators. Figure 10.2 provide the multiplicity of extra jets measured. All of the generators provide a reasonable description of the leading jet. Correct modeling of the leading jet is perhaps unsurprising since NLO calculations can include one additional jet in the hard scattering calculation. Differences among the generators become larger with increasing jet rank since the generators predict significantly different rates of additional jet production. The generators also predict some differences in the shapes of the jet p_T spectra. The MC@NLO+Herwig generator predicts the lowest rate of additional jet production and underestimates the number of events with at least 4 jets by 40%. The level of agreement between the remaining generators and the data can only be assessed using a more rigorous statistical test and is discussed below.

The same fully corrected data are compared to multi-leg leading order generators in Figure 10.3. In all cases, the renormalization and factorization scales are set to the defaults provided by the code authors. Alpgen used with Pythia or Herwig does a reasonable job of reproducing the data, while MadGraph+Pythia provides a less accurate description.

For lowest order generators, the predicted cross section can depend strongly on the choice of scale. Figure 10.4 shows the effects of such scale variation for the generators under consideration. In all cases the solid (dashed) line shows the predicted rate with the scale is halved (doubled). The measurement provides a smaller uncertainty on the cross section than the scale variations in the lowest order calculation would allow.

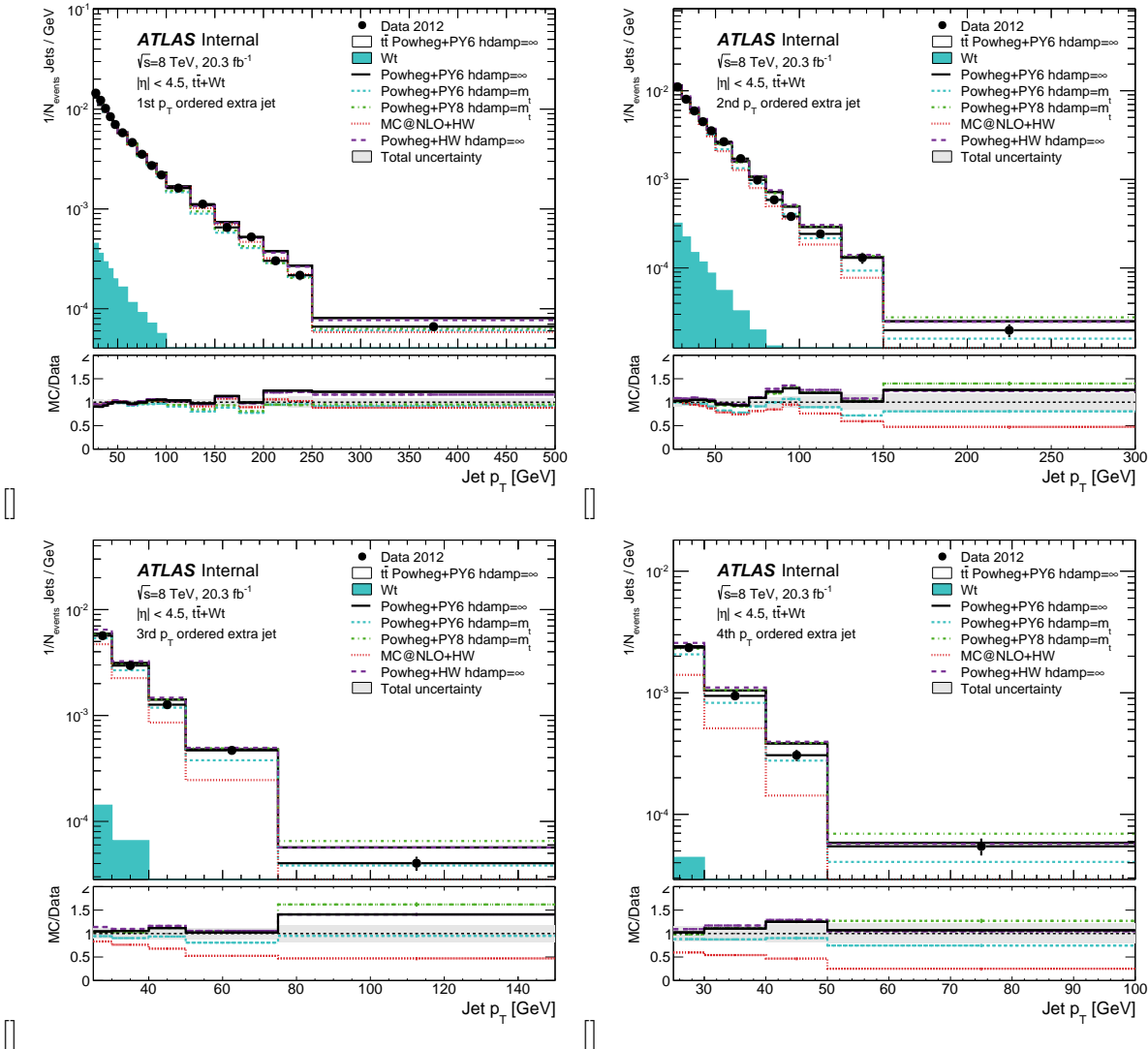


Figure 10.1: Distributions of the unfolded p_T of extra jets in data and simulation. Each sample is unfolded against a response matrix filled with baseline $t\bar{t}$ + single top simulation. The gray band on the ratio shows the sum of statistical and systematic uncertainties.

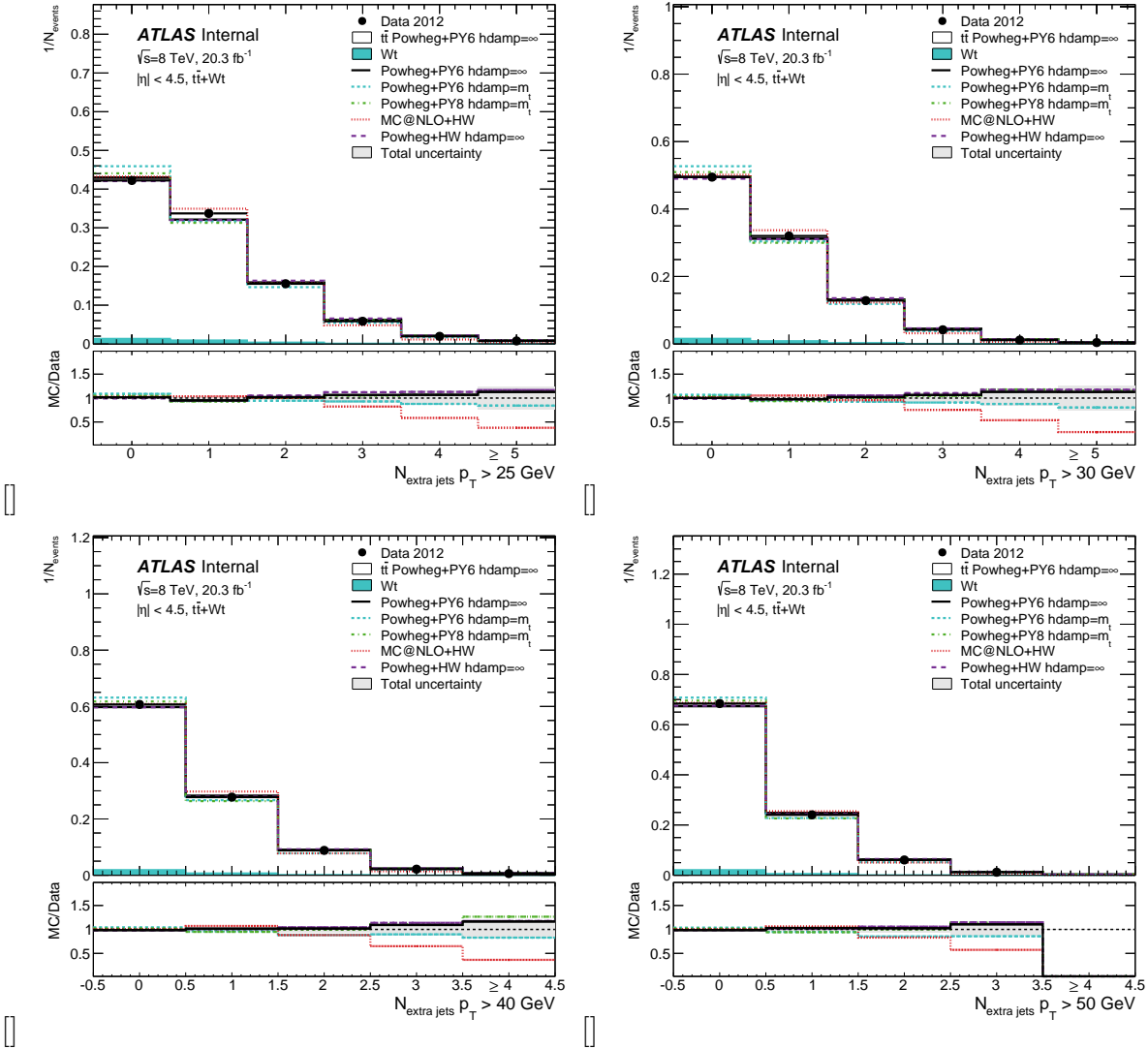


Figure 10.2: Distributions of the number of unfolded extra jets with $p_T >$ (a) 25, (b) 30, (c) 40 and (d) 50 GeV in data and simulation. Each sample is unfolded against a response matrix filled with baseline $t\bar{t}$ +single top simulation. The gray band on the ratio shows the sum of statistical and systematic uncertainties.

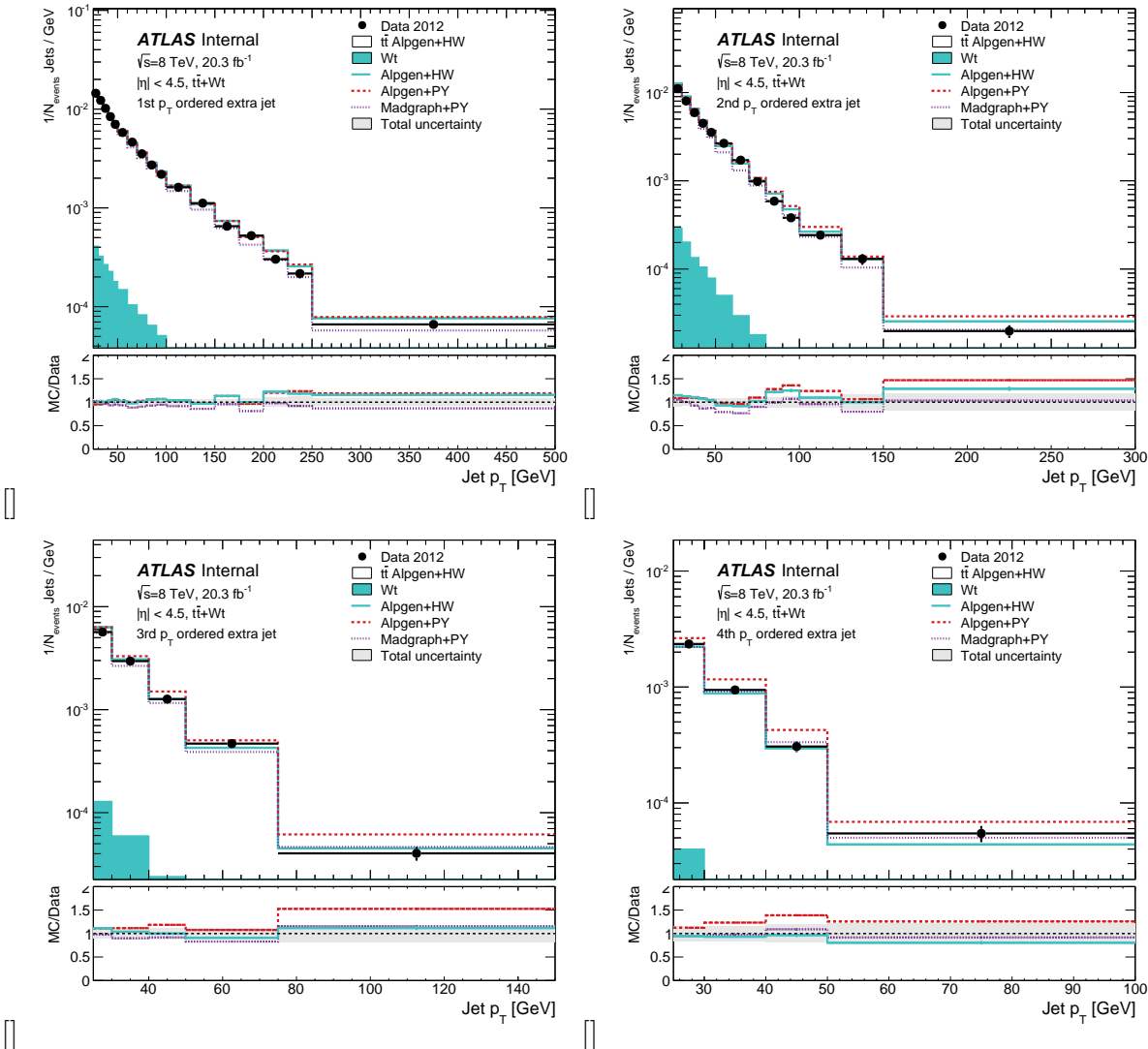


Figure 10.3: Distributions of the unfolded p_T of extra jets in data and simulation. Each sample is unfolded against a response matrix filled with baseline $t\bar{t} + \text{single top}$ simulation. The gray band on the ratio shows the sum of statistical and systematic uncertainties.

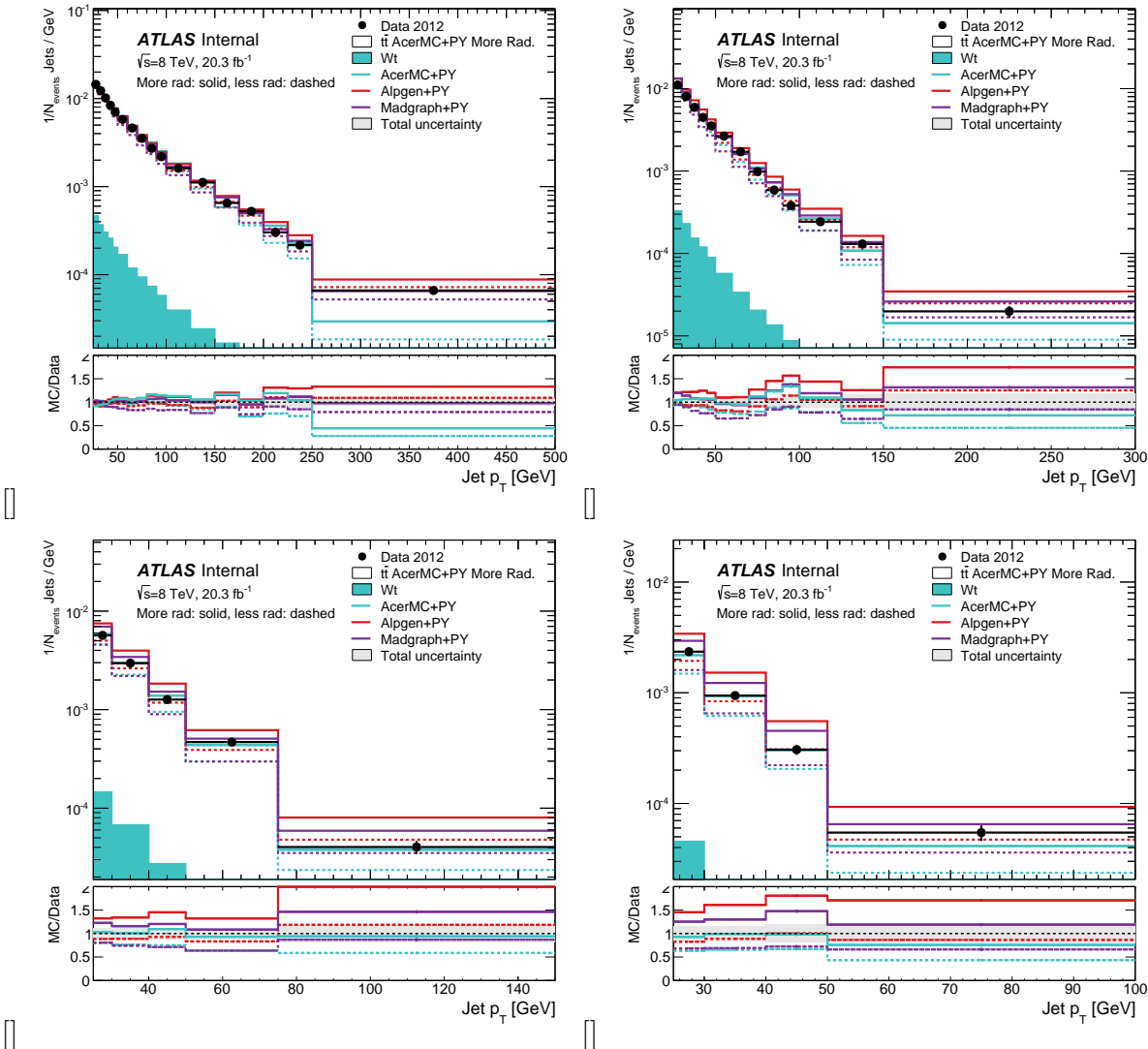


Figure 10.4: Distributions of the unfolded p_T of extra jets in data and simulation. Each sample is unfolded against a response matrix filled with baseline $t\bar{t}$ +single top simulation. The gray band on the ratio shows the sum of statistical and systematic uncertainties.

Generator	χ^2_{stat}	p -value	$\chi^2_{stat+sys}$	p -value
PowHeg+Pythia hdamp= ∞	103.06	2.9628×10^{-7}	53.59	8.9931×10^{-2}
PowHeg+Pythia hdamp= m_t	129.84	3.6708×10^{-11}	43.77	3.5480×10^{-1}
PowHeg+Pythia8	162.67	2.0444×10^{-16}	61.72	1.9762×10^{-2}
MC@NLO+Herwig	301.51	2.1411×10^{-41}	103.58	2.5140×10^{-7}
PowHeg+Herwig	246.22	4.3310×10^{-31}	55.95	5.9838×10^{-2}
Alpgen+Herwig	162.34	2.3213×10^{-16}	74.80	9.8529×10^{-4}
Alpgen+Pythia	147.24	6.7828×10^{-14}	50.71	1.4222×10^{-1}
MadGraph+Pythia	167.50	3.2078×10^{-17}	53.01	9.9021×10^{-2}
ACERMC+PythiaRadHi	185.62	2.6851×10^{-20}	116.39	3.8078×10^{-9}
ACERMC+PythiaRadLo	401.24	1.2019×10^{-60}	95.75	2.8533×10^{-6}
Alpgen+PythiaRadHi	709.83	7.6068×10^{-123}	104.70	1.7642×10^{-7}
Alpgen+PythiaRadLo	124.23	2.6195×10^{-10}	45.51	2.8983×10^{-1}
MadGraph+Pythia q^2 down	187.13	1.4771×10^{-20}	55.47	6.5133×10^{-2}
MadGraph+Pythia q^2 up	506.35	1.6412×10^{-81}	95.84	2.7788×10^{-6}

Table 10.1: χ^2 between extra jet p_T spectra in fully corrected data and different generators. The first column represents the agreement including only (diagonal) statistical uncertainties. The second column also includes the covariance due to systematic uncertainties (primarily JES).

10.2 χ^2 comparisons and discussion

Because the systematic and unfolding uncertainties have large correlations between bins, calculating the χ^2 from the full covariance matrix is necessary to assess the agreement between the data and generators. Table 10.1 presents the χ^2 obtained by comparing the extra jet p_T and rank distributions in the data and each generator. The χ^2 is calculated using only the statistical uncertainty, as well as the sum of systematic and statistical uncertainties. The structure of χ^2 can be visualized as a matrix of its addends $(N_{mc}^i - N_{data}^i)\sigma_{ij}^{-1}(N_{mc}^j - N_{data}^j)$. This matrix is shown for PowHeg+Pythia hdamp= ∞ , PowHeg+Pythia hdamp= m_t , MadGraph+Pythia, and PowHeg+Pythia8 in Figure 10.5.

Among NLO generators, PowHeg+Pythia hdamp= m_t and PowHeg+Pythia hdamp= ∞ agree the best with the data. PowHeg+Herwig and PowHeg+Pythia8 are slightly disfavored, and MC@NLO+Herwig is excluded. For multi-leg LO generators, Alpgen+Pythia agrees well with data, while MadGraph+Pythia and Alpgen+Herwig are slightly disfavored. The less radiation systematic variation of MadGraph+Pythia agree best with data, suggesting that the scale used in baseline ATLAS tunes may predict too much radiation in this analysis' fiducial region. ACERMC+Pythia does not reproduce the data well, regardless of scale.

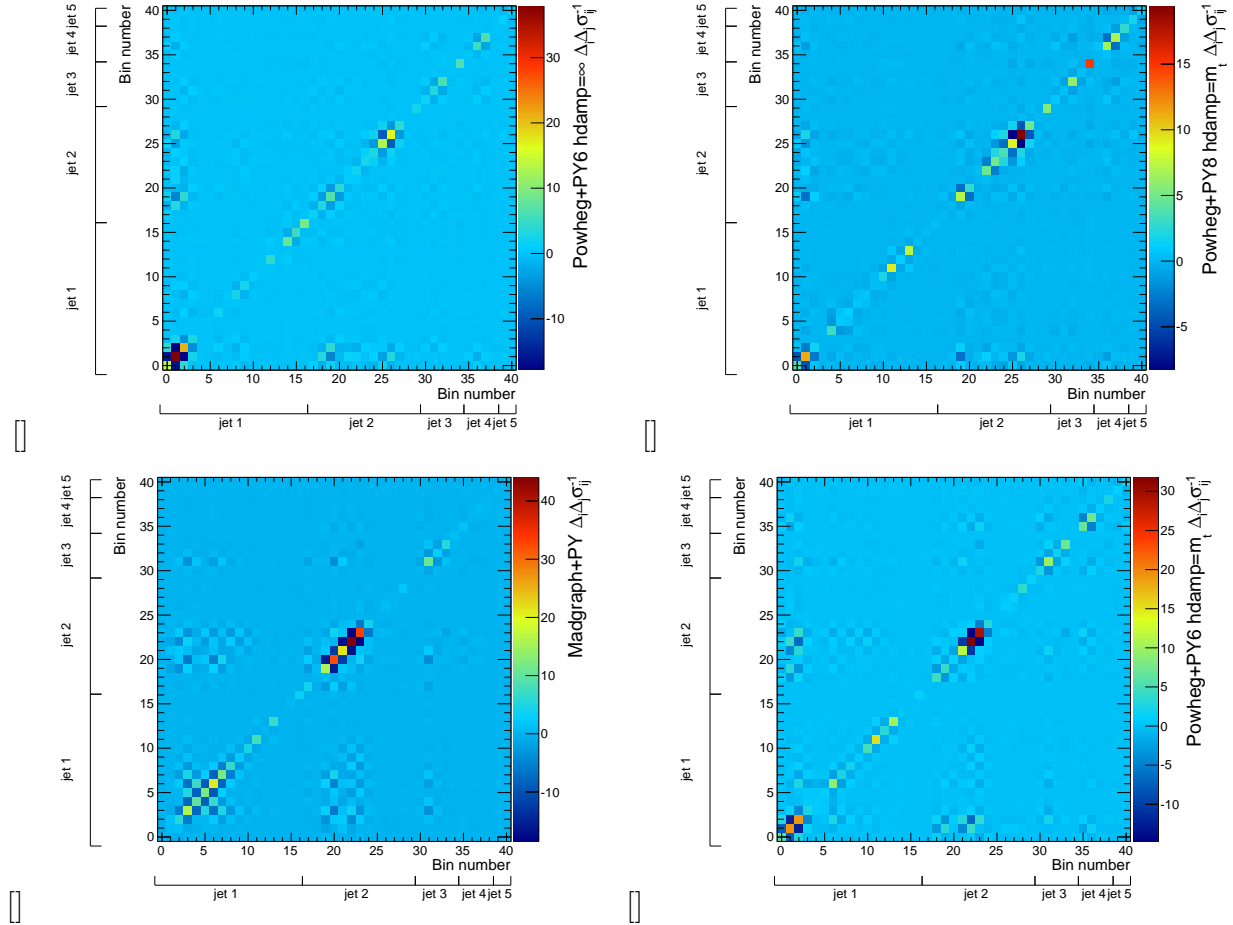


Figure 10.5: Visual representation of the χ^2 distributions for (a) PowHeg+Pythia $hdamp=\infty$ (b) PowHeg+Pythia8 (c) MadGraph+Pythia and (d) PowHeg+Pythia $hdamp=m_t$. Each element ij of the matrix is given by $M_{ij} = (N_{mc}^i - N_{data}^i)\sigma_{ij}^{-1}(N_{mc}^j - N_{data}^j)^j$ where N_{mc}^i is the number of jets predicted in bin i , N_{data}^i is the number of jets in bin i in data, and σ^{-1} is the inverse of the covariance matrix.

Chapter 11

Conclusions

Appendix A

Extra jets

stuff

Appendix B

Tracking studies

Appendix C

Modeling hadron decays